

# High-Resolution Spectroscopy of the Yellow Hypergiant $\rho$ Cassiopeiae from 1993 Through the Outburst of 2000-2001

A. Lobel<sup>1</sup>, A. K. Dupree, R. P. Stefanik, G. Torres,

*Harvard-Smithsonian Center for Astrophysics, 60 Garden Street, Cambridge MA 02138*

G. Israelian,

*Instituto de Astrofísica de Canarias, E-38200 La Laguna, Tenerife, Spain*

N. Morrison,

*Ritter Astrophysical Research Center, University of Toledo, Toledo, OH 43606*

C. de Jager, H. Nieuwenhuijzen,

*SRON Laboratory for Space Research, Sorbonnelaan 2, 3584 CA Utrecht, the Netherlands*

I. Ilyin,

*Astronomy Division, PO Box 3000, 90014 University of Oulu, Finland*

and F. Musaev

*Special Astrophysical Observatory, Nizhnij Arkhyz 369167, Russia*

## ABSTRACT

We present an overview of the spectral variability of the peculiar F-type hypergiant  $\rho$  Cas, obtained from our long-term monitoring campaigns over the past 8.5 years with four spectrographs in the northern hemisphere. Between 2000 June and September an exceptional variability phase occurred when the  $V$ -brightness dimmed by about a full magnitude. The star recovered from this deep minimum by 2001 April. It is the third outburst of  $\rho$  Cas on record in the last century. We observe TiO absorption bands in high-resolution near-IR spectra obtained with the Utrecht Echelle Spectrograph during the summer of 2000. TiO formation in the outer atmosphere occurred before the deep brightness minimum. Atmospheric models reveal that the effective temperature decreases by at least 3000 K, and the TiO shell is driven supersonically with  $\dot{M} \simeq 5.4 \times 10^{-2} M_{\odot} \text{ yr}^{-1}$ . Strong episodic mass loss and TiO have also been observed during the outbursts of 1945-47 and 1985-86.

A detailed analysis of the exceptional outburst spectra is provided, by comparing with high-resolution optical spectra of the early M-type supergiants  $\mu$  Cep (Ia) and Betelgeuse (Iab). During the outburst, central emission appears above

the local continuum level in the split Na  $D$  lines. A prominent optical emission line spectrum appears in variability phases of fast wind expansion. The radial velocity curves of H $\alpha$ , and of photospheric metal absorption lines signal a very extended, and velocity stratified dynamic atmosphere. The outburst spectra indicate the formation of a low-temperature, optically thick circumstellar gas shell of  $3 \times 10^{-2} M_{\odot}$  during 200 d, caused by dynamic instability of the upper atmosphere of this pulsating massive supergiant near the Eddington luminosity limit. We observe that the mass-loss rate during the outburst is of the same order of magnitude as has been proposed for the outbursts of  $\eta$  Carinae. We present calculations that correctly predict the outburst time-scale, whereby the shell ejection is driven by the release of hydrogen ionization-recombination energy.

*Subject headings:* instabilities — stars: atmospheres — stellar dynamics — pulsations — supergiants — stars: variables: hypergiants

## 1. Introduction

The recurrent eruptions of  $\rho$  Cas (HD 224014) recorded over the past century are the hallmark of the exceptional atmospheric physics manifested by the yellow hypergiants. These cool luminous stars are thought to be post-red supergiants, rapidly evolving toward the blue supergiant phase (de Jager 1998). They are rare enigmatic objects, and continuous high-resolution spectroscopic investigations are limited to a small sample of bright stars, often showing dissimilar spectra, but with very peculiar spectral properties. Yellow hypergiants are the candidates ‘par excellence’ among the cool luminous stars to investigate the physical causes for the luminosity limit of evolved stars (i.e. de Jager et al. 2001; Lobel 2001a; Stothers & Chin 2001). The post-red supergiant phase assumed for  $\rho$  Cas mainly relies, among other cool hypergiants such as HR 8752 and IRC+10420, on a substantial atmospheric overabundance observed in N and Na (Takeda & Takeda-Hidai 1994; El Eid & Champagne 1995). There is evidence that  $\rho$  Cas is surrounded by a tenuous circumstellar gas shell with the observation of forbidden [Ca II] optical emission lines (Lobel 1997)<sup>2</sup>. Recent high-resolution near-IR imaging with HST-WFPC2 does not show evidence of distant shells or a reflection nebula in  $\rho$  Cas (Schuster & Humphreys 2001), although complex circumstellar environments have been imaged in the cool hypergiants IRC+10420 and VY CMa

---

<sup>1</sup>Guest investigator of the UK Astronomy Data Centre.

<sup>2</sup>Partly available at <http://www.shaker.nl/Boekencatalogus.asp>.

(Humphreys et al. 1997; Smith et al. 2001). The distance to  $\rho$  Cas is large ( $d=3.1\pm 0.5$  kpc), and presently based on interstellar absorption and absolute visual magnitude estimates (e.g. Zsoldos & Percy 1991). Since the distance to IRC+10420 is estimated  $\sim 5$  kpc, the lack of detection in  $\rho$  Cas may result from the imaging technique. Its brightness causes bleeding near the star, although a range of integration times was used. The images do not show any extended structure within  $0.1''$  of the star, and down to the WFPC2's read noise  $2''$  away.

A spectroscopic study during 1993-95 showed that  $\rho$  Cas is a slowly pulsating supergiant with changes in the optical spectrum corresponding to variations of  $T_{\text{eff}}$  less than 750 K ( $T_{\text{eff}}=7250\text{K} - 6500$  K; Lobel et al. 1998). Its optical spectrum is peculiar because prominent permitted emission lines from neutral atoms sometimes appear, which are rarely seen in stellar spectra (e.g. in 1993 December; Lobel 1997). An important aspect of hypergiant spectra is the unusual large broadening observed in photospheric absorption lines. This broadening is currently attributed to large-scale atmospheric movements which assume highly supersonic velocities, while the stellar rotational broadening is small. Another remarkable aspect of  $\rho$  Cas' spectrum is the permanent, and cyclic, core doubling in low-energy resonance and subordinate photospheric absorption lines, such as Fe I, Fe II, and Ba II. The phenomenon is presently thought to result from a static central emission reversal which is optically thick with an excitation temperature of 3050 K, formed at a large distance from the photosphere (Lobel 1997). The intensity of both adjacent absorption components periodically alters with the Doppler shifts of the pulsating photosphere. High-resolution spectroscopic studies of stellar atmospheric dynamics based on split absorption lines are important because they are also observed in RR Lyrae variables, Cepheids, and FU Ori objects (Lobel 2001b). The line doubling appears to be physically linked with the changing spectral type of the hypergiant, because it was also observed in HR 8752 in 1960-70, when this binary star had a smaller  $T_{\text{eff}}$ , and appeared to be a spectroscopic twin of  $\rho$  Cas (Israelian, Lobel, & Schmidt 1999). There are presently no indications for a companion star in  $\rho$  Cas which, in addition to its visual brightness, makes it an important target for long-term spectroscopic monitoring to investigate the exceptional stellar atmospheric dynamics.

Of the bright cool hypergiants we investigated spectroscopically over the past decade, the spectrum of  $\rho$  Cas appears similar to RW Cep in late 1998, displaying comparable spectral properties mentioned above. A number of fainter yellow Ia-supergiants as HD 12399 and HD 179821, are spectroscopically even more compatible. RW Cep is classified as a semi-regular SRd variable, although the SRd class covers a variety of variable star types (Percy & Kolin 2000).  $\rho$  Cas is too luminous to be related to the majority of low-mass Asymptotic Giant Branch stars in this class, although its quiescent small light amplitudes and spectral properties suggest kinship, which could result from its advanced evolutionary stage.

Surprisingly, the spectrum of  $\rho$  Cas lacks core emission in the broad near-UV Mg II and Ca II resonance absorption lines (§ 7.3), although it is so prominently observed in the less luminous F- and G-type (Ib) supergiants (i.e. Lobel & Dupree 2000a). Variable and temporal emission line wings observed in H $\alpha$  may signal weak quasi-chromospheric activity (de Jager, Lobel, & Israelian 1997) during phases of enhanced mass-loss with  $\dot{M} \geq 10^{-5} M_{\odot} \text{yr}^{-1}$ . Observational evidence for a permanent kinetic temperature minimum in its extended outer atmosphere ( $\sim 10\%$  of  $R_{*}=400\pm 100 R_{\odot}$ ) is, however, presently not available.

Jura & Kleinmann (1990) presented a model for the weak silicate emission feature observed at  $9.7 \mu\text{m}$  with *IRAS* in 1983. They argued that dust formed at large distance from the star between 1973 and 1983, which could be the consequence of an outburst event observed in 1945-47. During the event many zero-volt excitation energy lines appeared, not previously observed in the absorption spectrum. These atomic lines, in fact normally observed in M-type supergiants, were strongly blue-shifted, signaling the ejection of a cool circumstellar gas shell (Beardsley 1961). In the following two decades after this event, a number of noteworthy papers were published in the astrophysical literature, discussing  $\rho$  Cas' peculiar spectroscopic changes in the years during and after the outburst (Popper 1947; Gaposchkin-Payne, Gaposchkin, & Mayall 1947; Keenan 1947; Thackeray 1948; Tai & Thackeray 1948; Beardsley 1953; Bidelmann & McKellar 1957). Between 1945 and 1946 the star rapidly dimmed and developed optical and near-IR TiO bands. Within a couple of years, the hypergiant brightened up by nearly a full magnitude, and a mid G-type spectrum was recovered around 1950. Beardsley (1961) discusses a possible brightness minimum during 1893, which could be the first reported outburst of  $\rho$  Cas. More recently, Boyarchuk, Boyarchuk, & Petrov (1988) also reported the detection of TiO bands in the optical spectrum during the moderate outburst of 1985-87 (§ 10).

This paper presents a detailed spectroscopic study of the recent outburst in  $\rho$  Cas in 2000-01. Our observations presently cover over 8.5 years, beginning in 1993, of continuous monitoring with high spectral resolution, including the recent outburst event. Throughout the paper we adopt the term ‘outburst’ or ‘eruption’ to indicate the variability phases of mid 2000 when newly formed TiO bands are observed in the spectrum. The terminology of ‘shell or mass ejections’, which has been used in the literature for these dramatic spectral changes is not adopted here, because we presently also report high-resolution observations of migrating discrete absorption features in the far violet extended wings of atomic lines during other variability phases. Section 2 discusses the spectroscopic observations and data reduction procedures. Section 3 compares, for the first time, long-term radial velocity observations with photometric monitoring, and we can therefore assign the peculiar spectral evolutions to different variability phases (§ 4 & 5). We observe, for example, that a prominent emission line spectrum develops during phases of fast expansion of the photosphere.

A discussion of the spectral changes during the 2000-01 outburst is provided in § 7. We analyze prominent TiO bands newly detected in the spectra, before and during the outburst minimum. From these measurements we compute in § 8 the gas mass-loss rate during the eruption, for a semi-empirical model of the supersonic expanding photosphere. Based on these observations we propose in § 11 a thermal mechanism that drives the eruptions of  $\rho$  Cas. New equations are presented that correctly predict the time-scale for the outbursts. We further demonstrate numerically that these atmospheric explosions are driven by the release of ionization-recombination energy of hydrogen during the expansion, which causes  $T_{\text{eff}}$  to decrease from  $\sim 7250$  K to below 4000 K (§ 6). A discussion of stellar outburst physics is provided in § 12. The conclusions of this investigation are summarized in § 13.

## 2. Observations and Data Reductions

### 2.1. Optical Line Profile Monitoring

Table 1 lists our high-resolution spectroscopic observations of  $\rho$  Cas between 1993 January 29 and 2002 July 7. A total of 78 spectra were observed on different nights with the Utrecht Echelle Spectrograph (UES) at the Nasmyth focus of the 4.2 m William Herschel Telescope at the Observatorio del Roque de los Muchachos (ING-WHT, Canary Islands), the Sofin spectrograph at the Cassegrain focus of the 2.6 m Nordic Optical Telescope (NOT, Canary Islands), the echelle spectrographs of the 1 m Zeiss-1000 telescope of the Special Astrophysical Observatory of the Russian Academy of Science (SAO/AN, Russia), and the fiberfed echelle spectrograph of the 1 m Ritter Observatory telescope (Toledo, OH). One echelle spectrum was recently obtained with the MuSiCoS echelle spectrograph of the 2 m Bernard Lyot Telescope at Pic du Midi Observatory (PMO, France) (S. Bagnulo 2002, priv. comm.), and an additional two coudé spectra were observed with the 2.6 m Shajn telescope of the Crimean Astrophysical Observatory (CrAO, Ukraine) (A. Rosenbush 2002, priv. comm.). The absorption line monitoring program includes  $H\alpha$ , Na  $D$ , the single and unblended Fe I lines around  $5570 \text{ \AA}$  of the Revised Multiplet Table (Moore 1945) (RMT) 686, the split Fe I lines around  $5500 \text{ \AA}$  (RMT 15), and the Ba II lines at  $\lambda 5853$  and  $\lambda 6141$  (RMT 2).

The wavelength coverage and nominal wavelength dispersions of the spectra are listed in columns [7] and [9] of Table 1, respectively. The majority of these echelle spectra are co-added from separate exposures during the same night, with exposure times provided in column [10]. The typical continuum signal-to-noise ratios (S/N) therefore exceed 100 with WHT-UES (mostly obtained from the service time programs in good weather conditions), while some of our dedicated observation runs with NOT-Sofin yielded exceptional spectra with  $S/N > 300$ , dependent on the quality of the seeing conditions. Two very high-resolution

( $R=170,000$ , but lower S/N) spectra were observed at SAO/AN in 1997 February and March, while three similar spectra were obtained in 1998 October and November with NOT-Sofin. These spectra cover only very limited wavelength portions, with broad echelle gaps, because they focus on the detailed profiles of the selected absorption lines. Five of the WHT-UES spectra do not include  $H\alpha$  because the data were obtained with the 18-order echelle E79 grating to improve the background measurements, or with a shorter central wavelength setting to investigate the near-UV spectrum (Israelian et al. 1999) or the Ca II resonance lines. In 1998 October a number of NOT-Sofin spectra were observed with different spectral resolutions on consecutive nights, to investigate the influence of the wavelength dispersion on the detailed line shapes, and to also extend the free wavelength range to beyond  $1 \mu\text{m}$ . Unlike HR 8752, we do not detect He I  $\lambda 10830$  in  $\rho$  Cas. The line is also absent in the near-IR spectra of 1999, and in the most recent observations of 2002 February.

The WHT-UES spectra were reduced with the standard IRAF<sup>3</sup> procedures. These include the average bias subtractions, order definition based on flat fields, removal of cosmic ray hits, and average flat division. A polynomial fit to the inter-orders is used to remove the background. The wavelength calibration is performed with a Th-Ar hollow-cathode lamp spectrum, and the pixel-to-wavelength mapping is iterated by increasing the number of calibration emission lines in the echelle order solutions to accuracies typically better than  $0.02 \text{ \AA}$ .

The NOT-Sofin spectra were also calibrated with a Th-Ar source (or lamp) spectrum obtained after each stellar exposure, to eliminate any temporal changes in the spectrograph in a combined wavelength solution with the use of the 4A software package (Ilyin 2000)<sup>4</sup>. It also includes a 2D-spline fit to remove scattered light, and weighted spectral order extraction which excludes the cosmic spikes from the fit. The sum of numerous master flat fields with overlapping orders is used to correct the pixel-to-pixel noise for the high S/N echelle images. The exposure times for the high-resolution observations ( $R \geq 80,000$ ) have been increased to exceed 100, while values above 50 are obtained for the lower resolution observations. The SAO/AN spectra were reduced with the DECH code (Galazutdinov 1992), which performs the standard echelle reduction steps. Most of these spectra have a  $S/N \geq 100$  per resolution element. Comparison Th-Ar exposures are obtained for the wavelength calibrations, although some of the dispersion solutions were also based on sharp telluric lines. The S/N of the Ritter spectra is between 100 and 200. Further details about the Ritter observations and

---

<sup>3</sup>IRAF is distributed by the National Optical Astronomy Observatories, which is operated by the Association of Universities for Research in Astronomy, Inc., under contract with the National Science Foundation.

<sup>4</sup>I. Ilyin's *Acquisition, Archiving, and Analysis Software Package User's Manual* is available at <http://www.not.iac.es/newwww/html/sofin.html>.

data reduction procedures are given in Morrison et al. (1997).

The mean accuracy of our wavelength calibrations for the spectra of Table 1 is better than  $\pm 1 \text{ km s}^{-1}$ . Note that these echelle spectra are not calibrated in the absolute flux scale, and that the placement of local continuum levels is either visually estimated, or results from a detailed spectral synthesis (§ 7).

## 2.2. Radial Velocity Monitoring

Separate from the line profile monitoring, 88 radial velocity observations were obtained between 1990 July 10 and 2002 February 7 at the Oak Ridge Observatory (ORO of the Smithsonian Astrophysical Observatory) with the 1.5-m Wyeth reflector and an echelle spectrograph. A single echelle order was recorded using a photon-counting intensified Reticon detector at a central wavelength of  $5187 \text{ \AA}$ , with a spectral coverage of  $45 \text{ \AA}$ . The strongest features present in this window are the lines of the Mg I b triplet. The resolving power is  $R \approx 35,000$ , and the nominal S/N ranges from about 25 to 100 per resolution element of  $8.5 \text{ km s}^{-1}$ . Wavelength calibration was performed in the standard way with Th-Ar lamp exposures taken before and after each stellar exposure. The rms residual, from the 30–35 calibration lines used in the dispersion solution, was typically around  $0.01 \text{ \AA}$ . The stability of the zero-point of our velocity system was monitored by means of exposures of the dusk and dawn sky, and small systematic run-to-run corrections were applied with the methods described by Latham (1992). Internal errors for each of our velocities were computed using the IRAF task XCSAO (Kurtz & Mink 1998), and range mostly from  $1.5 \text{ km s}^{-1}$  to  $2.0 \text{ km s}^{-1}$ .

In the next two sections we investigate the radial velocity changes obtained from individual line profiles in the high-resolution spectra. A comparison with the radial velocity monitoring at ORO is provided in § 5.

## 3. Light Curve vs. Radial Velocity Curve

In Figure 1 we compare the radial velocity curve with the  $V$ -brightness curve observed over the last 8.5 years. The solid dots are photo-electric measurements offered in Percy, Kolin, & Henry (2000). Their high-precision  $V$ ,  $R$ , and  $I$  observations are complemented with visual brightness estimates from the AAVSO (*solid boxes*). Visual brightness estimates during the outburst between JD 2451100 and JD 2452400 are offered by the AFOEV (French

Association of Variable Star Observers)<sup>5</sup>. The light curve shows how the star dims by  $1^{\text{m}}.2 - 1^{\text{m}}.4$ , from an unusual high brightness maximum of  $V \sim 4^{\text{m}}.0$ , to a deep minimum between 2000 September and December. In the half year after the deep minimum the star rapidly brightened up to average  $V$ -magnitude values observed before the outburst, however recently assuming another very bright visual maximum in late December 2001. The lower panel of Figure 1 shows the radial velocity curve ( $V_{\text{rad}}$ ) of the photosphere that we measure from the bisector at half intensity minimum of the unblended Fe I  $\lambda 5572$  absorption line (*solid dots*). These values have been added after JD 2450100 (1995 December) to the radial velocity curve in Figure 8 of Lobel et al. (1998). The dotted line is computed from a linear interpolation of the Fe I line *profiles* between consecutive observations, marked by the vertical lines. Note that the detailed changes of the line shape also contain information about the intensity changes between the observations, but which would not be represented with a simple spline fit to the radial velocity data. Although usually small, the difference is appreciable during phases when the line rapidly becomes much deeper and more asymmetric, while shifting blueward, as we observe during the outburst. The numbers correspond to the spectrum numbers of Table 1. The monitoring suggests that during the quiescent variability phases before JD 2451000 the radial velocity variations with a (rapid) decrease of absolute velocity are followed by a velocity increase that lasts considerably longer. After this time the unusually large velocity variations observed during the pre-outburst and the outburst cycle become rather symmetric.

For comparison the  $V_{\text{rad}}$ -curve is overplotted with the light curve (*dotted line in upper panel of Fig. 1*). The star becomes brightest for phases soon after the photosphere begins to expand. The stellar center-of-mass velocity of  $-47 \text{ km s}^{-1}$  was determined from the line bisector at half maximum of the forbidden [Ca II]  $\lambda 7323$  emission line, which was prominent in 1993 December (Lobel 1997, p. 53). We observe four phases between JD 2449300 and JD 2451000 with rapid brightness decreases that lag the fast (absolute) radial velocity decrements by  $\sim 3.5$  months. The radial velocity minima, marking maximum photospheric expansion, do not coincide with the  $V$ -brightness minima. The phase lag is clearly observed during the pre-outburst variability cycle of JD 2451000–2451500, and during the actual outburst. During the outburst, the  $V_{\text{rad}}$ -values decrease from  $\sim -30 \text{ km s}^{-1}$  to  $-65 \text{ km s}^{-1}$  in  $\sim 200$  d, which is followed  $\sim 100$  d later by a steep decline of the  $V$ -magnitude over the same period of time. We observe a strong correlation between the velocity and brightness amplitudes during the past 8.5 years. These observations show that the flow dynamics of the photospheric layers where the Fe I  $\lambda 5572$  line forms are strongly related to the overall thermal conditions of the atmosphere ( $T_{\text{eff}}$  and  $\log g$ ) in which the stellar  $V$ -band continuum is produced, near the maximum of the spectral energy distribution of this cool star. It signals

---

<sup>5</sup><http://cdsweb.u-strasbg.fr/afoev/>.



that the global photospheric dynamics due to pulsation causes the thermal conditions of the atmosphere to vary with time.

#### 4. Line Profile Evolution

Figure 2 shows the detailed line profile changes of  $H\alpha$ , Fe I  $\lambda 5572$ , and Fe I  $\lambda 5506$  (*panels left to right*). The line profiles are plotted in heliocentric velocity scale and have been normalized to the local continuum level, indicated by the right-hand horizontal line for each observation night. The stellar continuum level is estimated with a polynomial fit through wavelength regions of maximum intensity in the vicinity of the line, which remain sufficiently ‘flat’ with the spectral changes, and indicate the absence of weak absorption features. The Fe I  $\lambda 5572$  line has been continuum normalized through the flat intensity maxima beyond the line wings, while  $H\alpha$  requires a local continuum region around  $-320 \text{ km s}^{-1}$  because its violet wing sometimes blends with Ti II  $\lambda 6559$ . The split Fe I  $\lambda 5506$  line requires even farther continuum definition points because the violet line wing is more extended, while the red line wing is weakly blended. The same continuum fitting points have systematically been applied for a consistent measurement of equivalent width changes in  $H\alpha$  and Fe I  $\lambda 5572$  (§ 6), and for the radial velocity measurements from the line bisectors. The vertical dotted line is drawn at the stellar rest velocity of  $-47 \pm 2 \text{ km s}^{-1}$ .

For an improved visualization of the detailed line profile evolutions we plot dynamic line spectra in Figure 3. The observed line profiles are linearly interpolated between consecutive observation nights (*left-hand tickmarks*). While the velocity amplitudes and overall line profile evolutions in Fe I  $\lambda 5572$  and Fe I  $\lambda 5506$  are similar, the  $H\alpha$  line shape and velocity changes are notably different. The difference signals different regions for the mean formation of  $H\alpha$  and the Fe I lines. The absorption portions of the Fe I lines are formed around photospheric levels of  $-2 \leq \log \tau_{\text{Ross}} \leq 0$ , and these low-excitation energy lines can develop extended violet wings, produced in a cool optically thick expanding stellar wind at smaller optical depths. The body of the Fe I lines therefore tracks the photospheric movements over time, while  $H\alpha$  forms higher, over a much more extended region of the upper atmosphere. The extended  $H\alpha$  envelope of the hypergiant produces broad emission line wings at either or both sides of the central absorption core due to photon scattering in our line of sight. On the other hand, the dynamic  $H\alpha$  spectrum also reveals large Doppler shifts between 1993 and 1997. This strongly suggests that the  $H\alpha$  absorption core is rather optically thick, and results from radiation transfer through a moving line formation region, in front of the stellar disk, where photons are removed from or scattered out of our line of sight.

The outburst of 2000-01 is characterized by the strong blue-shifts of the Fe I lines in

the upper portions of Figs. 2 & 3. These neutral lines become much deeper and broader than usual in the spectra of summer 2000. Note that the split Fe I  $\lambda$ 5506 line has a central emission reversal which remains around the stellar rest velocity, while a far extended violet wing unfolds during the outburst. Our monitoring also reveals that many of the split lines in the optical spectrum of  $\rho$  Cas develop discrete and weak absorption features at high velocity in the violet line wing. These features migrate toward the central emission core over a long period of time (several years). It indicates the regular formation in the supersonic stellar wind of circumstellar gas ‘shells’ that gradually decelerate and dissolve. A more detailed discussion of the split line features will be given elsewhere. A very remarkable aspect of the dynamic spectra is that the H $\alpha$  core does not display the strong blue-shifts observed in the photospheric lines during the outburst. Instead, the H $\alpha$  absorption core becomes very weak during the deep brightness minimum. A comparison of the shape changes with H $\alpha$  in Betelgeuse and  $\mu$  Cep is discussed in § 7.2.

For an improved comparison of the detailed evolutions of the three line profiles with the stellar brightness changes, we convert the dynamic spectra into a movie sequence<sup>6</sup>. The day-to-day changes of the line shapes are shown together with the  $V$ -magnitude curve (*lower panel*). The movie reveals how the H $\alpha$  absorption core strongly red-shifts between 1995 and early 1999 (around JD 2451200), following the trend of the Fe I lines. After this time, the star rapidly brightens up to the very bright maximum of JD 2451600 (early 2000), leading up to the outburst event. During this pre-outburst phase unusual strong emission develops in the blue wing of H $\alpha$  (the white emission ‘spot’ in Figure 3 is at maximum normalized intensity of 25% above the continuum level), while the red-shifted absorption core becomes very broad and extended, indicating the collapse of the H $\alpha$ -envelope in our line of sight. However, during this pre-outburst cycle the Fe I lines also strongly red-shift, indicating a similar collapse or compression of the deeper photosphere. The combined spectral and photometric monitoring indicates that the outbursts of the hypergiant are preceded by phases of unusual fast contraction of the upper and lower atmosphere, during which the star quickly brightens up and strongly increases its  $T_{\text{eff}}$  (§ 6).

We note that a comparable strong emission increase of the blue H $\alpha$  wing has more recently been observed during a new very bright maximum around JD 2452270 (2001 December). The very extended red absorption core of H $\alpha$  observed during this period, followed by fast blueshifts of Fe I in early 2002, could suggest that a new outburst of  $\rho$  Cas is imminent. This appears supported by the fact that in 2002 July 07 an unusual H $\alpha$  profile was observed with a very extended red absorption wing. The profile is shown in the left-hand

---

<sup>6</sup><http://cfa-www.harvard.edu/~alobel>.

panel of Figure 2 (*top*). Most remarkably, the core of the line is split, and its large broadening has not been observed before. The recent evolution of the Fe I  $\lambda 5572$  is also strikingly similar to the changes observed before the 2000-01 outburst. If the star brightens up to a new very large brightness maximum over the next half year a new, and possibly more dramatic, outburst event could be expected.

## 5. Comparison of Radial Velocity Curves

The radial velocity curves of Fe I  $\lambda 5572$  (*filled circles*) and H $\alpha$  (*triangles*) are compared in Figure 4. These velocity values are measured from the absorption line bisectors, and listed in Table 2. The box symbols show the ORO radial velocity values, also listed in Table 3. These velocities are obtained from a cross-correlation technique applied to ORO spectra observed in the 5166 Å– 5211 Å wavelength range. The template for  $\rho$  Cas is selected from a library of pre-computed synthetic spectra based on the latest model atmospheres by R. Kurucz <sup>7</sup> (Nordström et al. 1994), covering a large range of stellar parameters and calculated for the precise wavelength window and resolution of the spectra. As described in more detail below, the effective temperature of  $\rho$  Cas varies considerably over the pulsation cycles. For the purpose of deriving radial velocities from these spectra, however, we adopt a fixed temperature of 6250 K for our template. Limited changes around this value have only a small effect on the results. Similarly, to match the line broadening of  $\rho$  Cas we adopt a  $v \sin i$ -value of 40 km s<sup>-1</sup>, as well as a surface gravity of  $\log g = 2.5$  (the nearest value in our template library) and  $[m/H] = 0.0$ . The effect of the gravity and metallicity parameters on the radial velocities is negligible. The one  $\sigma$ -error computed from the cross-correlation method is also shown in Figure 4, and listed in column [5] of Table 3.

There is good correspondence between the radial velocity values obtained from the bisector of the Fe I  $\lambda 5572$  line in the high-resolution spectra, and from cross-correlating the ORO spectra. Both methods independently yield the large Doppler shifts observed during the pre-outburst cycle and the outburst. The velocity curves agree to within 5 km s<sup>-1</sup>. Only for the observations around JD 2449600 does the cross-correlation yield  $V_{\text{rad}}$ -values of 9–10 km s<sup>-1</sup> smaller than obtained from the Fe I line bisector measurements. A detailed comparison of the ORO spectra of this epoch, with the high-resolution spectra in the same wavelength range, shows that the difference results from the many deep and broad absorption lines in this part of the spectrum. During this epoch, the deep lines develop enhanced absorption line wings, indicating a variability phase with stronger wind expansion. The

---

<sup>7</sup>Available at: <http://cfaku5.harvard.edu>.

deep lines are more asymmetric toward shorter wavelengths than the weaker Fe I  $\lambda 5572$  line. Consequently, the cross-correlation method samples more of the outflow by the larger wind opacity in the strong and broad lines. We therefore think that the Fe I radial velocity curve is more sensitive to the oscillations of the deeper photosphere, because absorption contributions from extra opacity in the variable wind are less for this weaker line. This is further supported by the behavior of the Fe I radial velocity curve which closely matches the  $V$ -brightness changes (Fig. 1), although the line was monitored by three different spectrographs during this epoch. Stronger blue-shifts for the deep absorption lines were for example measured from the bisector of the Y II  $\lambda 4900$  line during this epoch (Fig. 8 of Lobel et al. 1998). Note further that during the pre-outburst and outburst cycles the entire Fe I line profile, and the absorption line spectrum, strongly Doppler shift (Fig. 2), which explains why the measurements from both methods agree within a few  $\text{km s}^{-1}$  during these events.

We also computed the radial velocity changes based on the method of line moments. The moments of a line are defined by  $M_i = \int_{\text{line}} (v - v_0)^i (1 - F(v)) dv$ , with  $v_0$  the stellar rest velocity, and  $F(v)$  the normalized line flux in the velocity scale. The center of gravity velocity of the Fe I  $\lambda 5572$  line is computed from the first moment  $M_1$  with  $v_1 = M_1/M_0 + v_0$ , where the zeroth moment  $M_0$  is the equivalent width of the line. The radial velocity values determined from the line half width at half intensity minimum in Figure 4 are almost identical to the  $v_1$ -values. The open circles plot the velocity variations of the line determined from the second moment  $M_2$  with  $v_2 = -\sqrt{M_2/M_0} + v_0$ . The periodicity and phase of the  $v_2$ -curve are very similar to the radial velocity curve (*solid dots*), which indicates that the higher moments of the Fe I line do not reveal photospheric oscillation modes of a higher frequency. The velocities determined from the higher line moments do not show correlations with the  $V$ -brightness curve, which is unlike the strong correlation observed with the zeroth (§ 6) and the first moment. We think that the method cannot detect possible higher oscillation frequencies, based on detailed profile changes from the higher line moments, because the photospheric lines of the hypergiant are broadened by supersonic macrobroadening velocities (of  $\sim 21 \text{ km s}^{-1}$ ), which strongly increases the line breadth. Small changes of the line shape, caused by intrinsic variability, when integrating over the stellar disk (e.g. due to possible non-radial atmospheric movements), therefore become smoothed out by the overall large line broadening. It is however also possible that the moment method cannot detect higher oscillation frequencies because the time resolution of our dataset appears too coarse for shorter time intervals. The application of the line moment method is further complicated by the fact that our dataset is not fully homogeneous (four spectrographs were used) in both S/N and spectral resolving power, which influences the velocity curves obtained from the higher moments.

A remarkable aspect of the radial velocity curve is that the photosphere reveals an av-

erage variability period of  $\sim 300$  d between consecutive velocity maxima from JD 2449200 to JD 2450450, while the  $H\alpha$  absorption core only strongly red-shifts during this period of time. It signals a strongly velocity stratified dynamic atmosphere in which the deeper photospheric layers oscillate at a higher frequency, indicating smaller mean radius displacements than the upper  $H\alpha$ -atmosphere. After this period, both atmospheric regions strongly red-shift, indicating a global collapse (by  $\sim 13$   $\text{km s}^{-1}$  from the stellar rest velocity) during less than 200 d. This phase is followed by a blue-shift of the photosphere during which the moderate brightness maximum of JD 2450750 occurs. However,  $H\alpha$  remains strongly redshifted, indicating a continuous collapse of the upper atmosphere. Over the next variability phase the photosphere strongly blue-shifts during the pre-outburst cycle. This phase is followed by the development of a very extended red line wing in the absorption core of  $H\alpha$ , together with an unusual strong redshift of the photosphere (by  $\sim 18$   $\text{km s}^{-1}$  from the stellar rest velocity), which precedes the very large brightness maximum of JD 2451600, and the subsequent outburst minimum. These observations indicate substantial changes in the thermal conditions of the stellar ( $V$ ) continuum formation region with the growing pulsation amplitudes. The amplified photospheric oscillations lead up to the outburst event, which we discuss in the next section.

## 6. Changes of Atmospheric Conditions

Figure 5 compares the visual light curve with the equivalent width ( $W_{\text{eq}}$ ) measurements of Fe I  $\lambda 5572$  (*open circles*), listed in column [4] of Table 2. The  $W_{\text{eq}}$ -values range between 282  $\text{m}\text{\AA}$  and 642  $\text{m}\text{\AA}$ , with typical errorbars of  $\pm 15$   $\text{m}\text{\AA}$ . The errors are computed by placing the continuum level for the line intensity normalization 1% higher and 1% lower. Similar error values are obtained for  $H\alpha$  (*crosses*; net equivalent width), and for Fe II  $\lambda 5325$  (*open triangles*), also listed in column [8] of Table 2. We find a very strong correlation between the  $V$ -magnitude and the  $W_{\text{eq}}$ -value of the Fe I line. It shows that this neutral absorption line is very sensitive to variations of the local excitation conditions, caused by changes in the thermal circumstances of the deeper photosphere with pulsation, as we discussed in § 3 from the radial velocity curve of the line. We find a tight relationship between the  $V$ -magnitude, and  $W_{\text{eq}}(\text{Fe I } 5572 \text{ \AA})$  expressed in  $\text{m}\text{\AA}$ :

$$V = 1.88 \times 10^{-3} \times W_{\text{eq}} + 3.75 \text{ mag.} \quad (1)$$

On the other hand, we also find that the  $W_{\text{eq}}$ -changes of the Fe II line are anti-correlated with  $V$ . This reveals that the population of the energy levels of neutral and singly-ionized iron lines in the atmosphere of  $\rho$  Cas is dependent of the variable local excitation conditions,

and strongly sensitive of the abundance of the iron ions. In the low-density atmospheres of cool supergiants with  $T_{\text{eff}}$  around 7000 K, the iron ionization balance is very sensitive to changes of the local thermal conditions, which causes the strength of Fe I and Fe II lines to vary oppositely with small variations of  $T_{\text{eff}}$ .

In the lower panel of Figure 5 we estimate the variation of  $T_{\text{eff}}$ , based on the  $W_{\text{eq}}$ -changes of the Fe I line with pulsation. The atmospheric conditions for the optical spectrum of 1993 December 20, and of 1995 April 18 have been determined in Lobel et al. (1998) from  $W_{\text{eq}}$  measurements of 23 Fe I and 11 Fe II lines. The spectrum of 1993 corresponds to  $T_{\text{eff}}=7250\pm 200$  K, and the spectrum of 1995 to  $T_{\text{eff}}=6500\pm 200$  K, whereby  $\log g$  decreases from 1.0 to 0.5, from (near) maximum to minimum  $V$ -brightness. The decrease of  $T_{\text{eff}}$  corresponds to an increase from 393 mÅ to 551 mÅ in Fe I  $\lambda 5572$ , which we utilize to estimate the  $T_{\text{eff}}$  for other variability phases by a linear interpolation:

$$T_{\text{eff}} = 9115 - W_{\text{eq}} \times 750 / 158 \text{ K} . \quad (2)$$

The  $T_{\text{eff}}$ -estimates from the  $W_{\text{eq}}$ -values of the Fe I line are marked with open circles. We note however that the direct correlation of the equivalent width values with the  $V$ -curve of equation (1) breaks down for the deep outburst minimum observations of 2000 September 17 and 20. During the outburst, the strong decrease of  $T_{\text{eff}}$  causes the population of this neutral line to shift from the linear to the flat part of the curve of growth. In these conditions the line depth saturates and becomes no longer directly correlated with the steep brightness decrease. An estimation of  $T_{\text{eff}}$  during the outburst can therefore not be obtained from an extrapolation of the  $W_{\text{eq}}$ -values observed during the outburst.

On the other hand, the strong correlation of the Fe I line with  $V$  during the quiescent pulsation phases enables us instead to directly estimate  $T_{\text{eff}}$  from  $V$ , by inserting equation (1) in equation (2):

$$T_{\text{eff}} = 9115 - 2525 \times (V - 3.75) \text{ K} . \quad (3)$$

The correlation reveals how  $T_{\text{eff}}$  varies by  $\sim 3000$  K during the outburst, from a very high value  $\simeq 8000$  K around JD 2451600 (2000 April), to a low  $T_{\text{eff}} \simeq 5000$  K during the deep brightness minimum of 2000 September and December. The extrapolation with equation (3), based on  $V$ , applies because we further check from spectral synthesis calculations that the spectra observed during the deep outburst minimum correspond to  $T_{\text{eff}}$ -values below 5000 K.

It is of note that the Fe I measurements after JD 2450250 show a *decrease* of  $W_{\text{eq}}$  to a minimum value around JD 2450409. However, the  $V$ -brightness estimates suggest an ongoing dimming of the star, which contradicts the strong  $W_{\text{eq}}$ - $V$  correlation observed during other quiescent variability phases. We think however that the visual brightness estimates

during this period (spring term) could be biased by the low altitude of the star for observers in the northern hemisphere. This is likely the case because our  $W_{\text{eq}}$ -values are measured from spectra of two different spectrographs, yielding a continuous sequence with a local minimum around JD 2450409, while the more accurate photo-electric  $V$  measurements were only obtained after this date (Fig. 5, *solid dots in the upper panel*). This is further supported since the  $W_{\text{eq}}$ -curve, with a local minimum around this epoch, also confirms the variability period of  $\sim 300$  d, that is observed between other consecutive brightness maxima, and also noticeable in the  $V_{\text{rad}}$ -curve (§ 5). Alternatively, when taking all visual brightness estimates at face value it would indicate that the correlation equations are not always perfect for this semi-regular variable star.

We further tested the large  $T_{\text{eff}}$  decrease during the outburst with the ORO spectra. The spectra are run through a grid of Kurucz models with  $4500 \text{ K} \leq T_{\text{eff}} \leq 8000 \text{ K}$ . For each of the spectra, the cross-correlation method selects a template spectrum that best fits the observed spectrum. The  $T_{\text{eff}}$  and line broadening are varied during the iterations, while the model gravity is set to a constant value. A rotational convolution is performed for the line broadening, but without changing the line equivalent width (i.e. the microturbulence broadening is assumed to remain constant). This rather simplified method of determining atmospheric changes with phase yields however a clear correlation between  $T_{\text{eff}}$  and the line broadening, in the sense that the spectral lines are broader when  $T_{\text{eff}}$  is higher. The correlation is very strong during the pre-outburst cycle and the actual outburst when  $T_{\text{eff}}$  strongly varies. The iterations reveal that  $T_{\text{eff}}$  increases from  $\simeq 6000 \text{ K}$  on JD 2451371 to  $\simeq 7600 \text{ K}$  on JD 2451598 (around the large  $V$ -brightness maximum before the outburst). After this period, the deeper photosphere rapidly expands, while the star quickly dims by more than a magnitude in  $V$ . Around the brightness minimum of JD 2451800 we compute that  $T_{\text{eff}}$  assumes the smallest value in the model grid of  $4500 \text{ K}$ . The temperature minimum lasts for only  $\sim 100$  d, while the photosphere quickly contracts from maximum expansion velocity to the stellar rest velocity (a  $V_{\text{rad}}$  decrease by  $\simeq 18 \text{ km s}^{-1}$ ). The star subsequently brightens up by  $0^{\text{m}}.8$  within the next 100 d, returning to  $T_{\text{eff}}$  above  $6000 \text{ K}$  before JD 2452000.

The rapid  $T_{\text{eff}}$  excursion by more than  $3000 \text{ K}$  for the outburst of  $\rho$  Cas, obtained from both methods described above, indicates that it results from the exceptionally large and fast mean atmospheric displacements we observe before and during the event. In the next section we investigate the changes of the optical spectrum in more detail. We show that the above derived  $T_{\text{eff}}$ -values are in close agreement with the detailed spectral synthesis models in which the gravity acceleration and the turbulence broadening are also varied. During the outburst minimum  $T_{\text{eff}}$  decreases so rapidly that TiO absorption bands can form, which are typically only observed in M-type (or very late K-type) stars as  $\mu$  Cep and Betelgeuse.

## 7. Spectral Variability During Outburst

### 7.1. Optical Emission Lines

We observe that during phases of fast photospheric expansion a prominent emission line spectrum develops with line intensity maxima above the local continuum level (*vertical dashed lines labeled a and b in Fig. 1*). The spectrum of 1993 December (*labeled a*) corresponds to a phase around maximum brightness with  $T_{\text{eff}}=7250$  K,  $\log g=0.5$ , and a projected microturbulence velocity of  $\zeta_{\mu}=12$  km s<sup>-1</sup> (Lobel et al. 1998). Strong emission lines of low-excitation energy metals as Fe I, Ni I, and Ca I have been identified (see Lobel 1997, p. 45). The presently observed strong correlation of emission line appearance in the spectrum of  $\rho$  Cas with the radial velocity curve indicates that their formation is related to enhanced excitation in the accelerating outflow during very fast photospheric expansions. The latter is supported by the far violet extended absorption line wings we observe during these phases, signaling the development of an optically thick expanding wind from the supergiant when  $T_{\text{eff}}$  is high. These very extended violet line wings were for example not observed in 1995 April, when  $T_{\text{eff}}$  decreased to 6500 K, and the star reached the  $V$ -brightness minimum around JD 2449820. Since the emission line spectrum remains static (and slightly blueshifted around the sound speed) it can emerge from a steady shock interface between the fast stellar wind that collides with denser circumstellar, or perhaps interstellar material, expelled during the violent (eruptive) mass-loss history of the hypergiant.

Figure 6 compares the spectral changes during the outburst for a small wavelength region around the Fe I  $\lambda 6358$  line. This line is sometimes observed in emission, for example during the pulsation phase of 1993 December when the atomic absorption lines developed far violet extended wings, indicating a phase of enhanced mass-loss. During this epoch, several other permitted low-energy Fe I and Ca I lines were observed in emission (Lobel 1997, Chap. 4).

The high-resolution spectral monitoring between 1994 and 1997 does not reveal prominent optical emission lines. The radial velocity curve (Fig. 1, *lower panel*) shows an overall decrease of atmospheric outflow during this period from JD 2449400 to JD 2450700. However, in 1998 October (Fig. 6, *spectrum labeled b*) we detect the optical emission lines again above the stellar continuum level. Similar to 1993 December, the absorption lines develop extended violet wings due to enhanced opacity in the stellar wind. During these phases of increased  $T_{\text{eff}}$  with fast wind expansion,  $\rho$  Cas' optical absorption line spectrum, mainly composed of neutral atomic species, becomes rather weak, and the peculiar emission line spectrum can therefore appear above the level of the continuum.

The synthetic spectrum is shown by the upper dotted line in Figure 6. The blend of Fe I



and V I lines at 6358 Å becomes very weak, computed for a Kurucz model of  $T_{\text{eff}}=7250$  K and  $\log g=1.0$ . After 1998 October,  $V$  dims by at least half a magnitude during  $\sim 5$  months, where after the star brightens up to the very bright maximum of 2000 April. The spectrum of 1999 May in Figure 6 (*solid line labeled c*), observed before this maximum, indicates  $T_{\text{eff}}=5750$  K and  $\log g=0.5$  from a best fit (*dotted line*). Hence,  $T_{\text{eff}}$  decreases by  $\sim 1500$  K after 1998 October, while the wind expansion strongly decelerates after early 1999 during the pre-outburst cycle.

The high-resolution spectrum of 2000 July 19 in Figure 6 (*solid line labeled d*) is observed within a month after maximum photospheric expansion velocity. Note that the continuum level of the spectrum is shifted down for display purposes. We observe that the entire absorption line spectrum displaces toward the shorter wavelengths. It reveals an average expansion of a large fraction of the deeper atmosphere, where the bulk of the photospheric spectrum forms. The synthetic spectrum fit (*middle dotted line*) shows that  $T_{\text{eff}}$  decreases to 4250 K with  $\log g=0$ . Hence, our detailed spectral modeling also reveals a decrease of at least 3000 K during the outburst of  $\rho$  Cas.

A comparison with the spectrum of the M-type supergiants Betelgeuse (*dashed line*) (with  $T_{\text{eff}}=3500$  K), and  $\mu$  Cep (*lower solid line*) in Figure 6 shows that the cores of neutral V I, Fe I, Ti I, and Cr I lines in  $\rho$  Cas become considerably deeper during the strong  $V$ -brightness decrease. We model the outburst spectrum by neglecting molecular lines in the synthesis. The good fit reveals that molecular absorption remains weak, and the local continuum level is mainly determined by blends of atomic lines. On the other hand, the synthetic spectrum of Betelgeuse is computed (*lower dotted line*) by including many molecular lines as TiO, C<sub>2</sub>, CN, etc. (Kurucz 1996). However, molecular opacity contributes substantially to the decrease of the local continuum level in Betelgeuse and  $\mu$  Cep (to  $\sim 0.5$  in normalized intensity). Contributions from TiO opacity are very important for an accurate synthesis of these M-type spectra (for a discussion see Lobel & Dupree 2000b). Our spectral observations and modeling indicate that the strong brightness decrease observed for  $\rho$  Cas between 2000 April and October corresponds to a decrease of  $T_{\text{eff}}$  by at least 3000 K, and probably by as much as 3500 K to the deep brightness minimum of late 2000. In less than half a year after the deep minimum the optical spectrum returns to  $T_{\text{eff}}\simeq 5750$  K around 2001 February (*solid line labeled e*).

## 7.2. H $\alpha$ Absorption and Emission

The upper panel of Figure 5 shows that the changes of the H $\alpha$  profile are uncorrelated with the variability of  $V$ . However, we observe a strong decrease of the (total) equivalent

line width, while the absorption portion of the line strongly red-shifts between JD 2449200 and JD 2450450 (see Fig. 3). During this period, the violet extension of the H $\alpha$  absorption core diminishes (Fig. 2), indicating that the wind in the upper H $\alpha$ -atmosphere stalls, and begins to collapse onto the deeper photosphere. The  $W_{\text{eq}}$ -changes of H $\alpha$  also occur much slower than observed for the iron lines, which confirms the rather different mean formation region of H $\alpha$ .

Figure 7 shows a number of high-resolution spectra around H $\alpha$  for the epochs labeled *a* to *d* in Figure 1. We observe that the Ti II absorption line, shortward of H $\alpha$ , becomes weaker in the outburst spectrum (*d*), due to a decrease of the excitation temperature in the line formation region. On the other hand, the neutral Fe I and V I lines, also labeled in the graph, become deeper and assume intensities comparable to these lines observed in Betelgeuse (*long dashed line*) and  $\mu$  Cep (*long dash-dotted line*). During the outburst the H $\alpha$  absorption core does not blue-shift, but instead remains centered around the stellar rest velocity, while the absorption core becomes weaker. The line also develops weak asymmetric emission wings at both sides of the central absorption core, reminiscent of the strongly self-absorbed emission lines observed in the near-UV spectra of Betelgeuse, and of other cool luminous stars (i.e. Lobel & Dupree 2001).

It is interesting to note that laser pulse laboratory experiments in hydrogen plasma produce strong Balmer emission lines during ionization recombination. Fill et al. (2000) argue that the observed emission production time-scales and population balance calculations reveal that three-body recombination is the main mechanism populating the levels that emit the Balmer lines during these experiments. Their measurements involve however electron densities  $n_e \simeq 10^{17} \text{ cm}^{-3}$  at gas pressures of  $P = 10^3 \text{ dyn cm}^{-2}$ , while hydrostatic photospheric models of  $\rho$  Cas assume  $n_e \leq 10^{13} \text{ cm}^{-3}$  for  $P \leq 10 \text{ dyn cm}^{-2}$ . Nevertheless, conditions of larger  $n_e$  and  $P$  can result by strong shock compression during the outburst, producing enhanced line emission in a cooling and expanding wake. The emission wings observed for H $\alpha$  in the outburst spectra of  $\rho$  Cas could therefore result from the recombination of partially ionized hydrogen gas.

The filling in of H $\alpha$  by line emission due to recombination during the outburst is also supported by the lack of evidence for a steady chromosphere in  $\rho$  Cas. In Betelgeuse and  $\mu$  Cep the stellar chromosphere strongly populates the H $\alpha$  transition, which produces the deep H $\alpha$  absorption cores in these M-type stars. However, if these supergiants had no chromosphere, the H $\alpha$  absorption core would become invisible against the photospheric spectrum. This can be illustrated with a detailed synthesis of their optical spectra (which are mainly formed by TiO opacity) (*dotted spectrum*), excluding the model for the chromosphere (see Lobel & Dupree 2000b). The outburst spectrum of  $\rho$  Cas, with a comparable low  $T_{\text{eff}}$ , shows

however much weaker  $H\alpha$  absorption with prominent emission line wings. It indicates that the line does not become excited in a stellar chromosphere. If a chromosphere were present during the outburst, much stronger  $H\alpha$  absorption would have to develop. This would prevent the recombination of partially ionized hydrogen in the outer atmosphere, and hence would suppress the formation of emission line wings.

The strongly self-reversed shape of the  $H\alpha$  emission line during the outburst can be produced if the  $H\alpha$  transition is sufficiently optically thick. Since we observe that the central absorption core remains almost static during the outburst, this would indicate that the central line scattering region is formed far above the  $H\alpha$  emission formation region, and does not share the dynamics of the outburst. This implies that  $\rho$  Cas'  $H\alpha$  atmosphere is considerably more extended than the dimensions derived from radial displacements based on the photospheric radial velocity changes during the outburst (§ 8.2). Detailed semi-empirical modeling of the Balmer lines of  $\rho$  Cas will be presented elsewhere.

It is of note that our NOT-Sofin observations of the G2–G5 supergiant HD 179821 also show variable red- and blueshifted emission in the  $H\alpha$  absorption core. This supergiant has recently been proposed as a low-mass post-AGB candidate, based on a LTE abundance analysis by Thévenin et al. (2000). Its far-IR excess signals a cool detached dust shell. There is however no consensus on the evolutionary status. Its high expansion velocity of  $34 \text{ km s}^{-1}$  is much larger than the value of  $10\text{--}15 \text{ km s}^{-1}$  for low-mass post-AGB stars, which rather suggests a massive supergiant. The emission humps in  $H\alpha$  result from NLTE-effects in a fast and spherically expanding wind (Dupree et al. 1984), inside the dust cavity. The emission sporadically appears above the stellar continuum level, as is observed in  $\rho$  Cas.

### 7.3. Ca II H & K Absorption

The absence of a permanent chromosphere in  $\rho$  Cas is further supported by the spectral monitoring of Ca II H & K. Emission reversals in the cores of these resonance lines are classic indicators of chromospheric activity in cool stars. However, near-UV observations with WHT-UES (1996 December 26) and NOT-Sofin (1998 October 6) do not show Ca II emission in the broad absorption cores. In Figure 8 the Ca II H & K lines only reveal a deep central core with zero intensity, within the limited spectral noise levels. This is unlike the prominent core emission observed in the Ca II K line of Betelgeuse (*dashed line lower panel*), modeled in Lobel & Dupree (2000b) with a kinetic temperature of the chromosphere not in excess of 5500 K. Note however that the broad wings of Ca II H & K show permanent emission lines of Fe I (*labeled RMT 45 and 43*). Recent observations with NOT-Sofin (2002 January 29) of the Ca II H line after the outburst of  $\rho$  Cas neither reveal a central emission

core (*dashed line in upper panel*). The absence of a steady chromosphere in  $\rho$  Cas is also apparent by the absence of central emission in the Mg II *h* & *k* lines, discussed and modeled in Lobel et al. (1998). It is of note that we neither observe central emission in Ca II K of HD 179821, indicating a massive Ia-supergiant like  $\rho$  Cas.

#### 7.4. Na *D* Emission

We observe a remarkable evolution in the split Na *D* lines of  $\rho$  Cas during the 2000-01 outburst. The high-resolution spectra in Figure 9 show that the central portion of the lines, between the adjacent black absorption troughs, turns in emission above the local continuum level (*solid lines labeled d*) on 2000 July 19 and August 2. The prominent central emission is also observed in the lower resolution spectra of September 17, 20, & 21 (Table 1, profiles not shown in Fig. 9). The lines are plotted in the heliocentric velocity scale, centered at the long-wavelength line of the doublet. Note that the central emission maxima do not coincide with the stellar rest velocity of  $-47 \text{ km s}^{-1}$  (*vertical dotted line*), but peak longward by  $\sim 10 \text{ km s}^{-1}$ . Another weaker feature is also observed shortward of stellar rest velocity in both lines of the doublet.

It is of importance to point out that the contamination of interstellar absorption in the Na *D* lines of  $\rho$  Cas (at a distance of  $\sim 3.1 \text{ kpc}$ ), and of other distant hypergiants, has always cast doubt on an interpretation which attributes the curious splitting to a central emission reversal. However, the high-resolution outburst spectra clearly show that central emission does (at least partly) involve the formation of these very complex resonance lines.

In order to investigate interstellar line contributions we compare with the Na *D* lines observed in HR 8752. The thin solid lines of the small panel show both doublet lines of  $\rho$  Cas in the same velocity scale, compared to these lines in HR 8752 (*thin dashed lines*), observed with NOT-Sofin in 1998 October, with very high resolution ( $R \sim 160,000$ ). Both hypergiants are only  $7^\circ 22'$  apart in the sky, and reveal narrow absorption components around  $-50 \text{ km s}^{-1}$  and  $-30 \text{ km s}^{-1}$  (with a similar FWHM of  $\simeq 10 \text{ km s}^{-1}$ ). These distinct absorption features can therefore be attributed to high-velocity clouds of the interstellar medium (ISM) in the direction of the Cas OB5 association. The interstellar absorption partly distorts the shape of the stellar central emission line, so that its actual intensity cannot accurately be determined. Moreover, we also observe two even narrower absorption features in both Na *D* lines of  $\rho$  Cas. The features, with velocities around heliocentric rest velocity, can possibly be attributed to weaker contributions from the local interstellar medium (LISM).

The increase of the central emission reversals above the local continuum level results

from the decrease of the optical continuum flux with the decrease of  $T_{\text{eff}}$  during the outburst. The flux of the central emission is therefore independent of the photospheric conditions, indicating that Na  $D$  emission emerges from an extended gas envelope around the hypergiant. We observe that the deep absorption portions of the Na  $D$  lines do not reveal significant Doppler shifts during the outburst, similar as for  $H\alpha$ . These static lines are unlike the weaker photospheric absorption spectrum which strongly blue-shifts. However, it should be remembered that the Na  $D$  lines are strongly intensity saturated. The absorption saturation distorts the line shape, which renders the lines useless for radial velocity measurements. On the other hand, the violet wings of both lines are excellent indicators for enhanced opacity in an expanding wind. The stellar wind is observed by the violet wing extensions during the outburst (*solid lines*), which are stronger than in the spectrum before the outburst (*dashed line labeled c*). Note for example that these violet line wings were very strong in the spectrum of 1993 December (*dash-dotted line labeled a*). In both cases extensions out to  $\sim 130 \text{ km s}^{-1}$  from the stellar photospheric values can be identified.

## 7.5. TiO Absorption Bands

We observe that TiO absorption bands develop in the outburst spectra of  $\rho$  Cas in 2000 July, August, and September. Figure 10 compares the high-resolution spectra around  $5450 \text{ \AA}$  of 2000 July 19 and August 2, with the spectra of 2000 September 17 and 20, and of 2001 February 5 and October 2 (*thin solid lines*). The spectra are shifted upward by 15% of the normalized stellar continuum flux. This wavelength region contains two split Fe I lines ( $\lambda 5446.9$  and  $\lambda 5455.6$ ) of RMT 15. The cores of these Fe I lines are also observed in the spectra of Betelgeuse (*dashed line*) and  $\mu$  Cep (*dash-dotted line*) where they do not split. The local normalized continuum level in the spectra of these M-type supergiants is strongly reduced (to  $\sim 40\%$ ) due to photospheric TiO opacity.

In the summer of 2000 the local continuum level in the  $\rho$  Cas spectra longward of  $5447 \text{ \AA}$  decreases by 10–15% with respect to the mean continuum level shortward of Fe I  $\lambda 5446.9$ . The intensity jump results from the development of TiO ( $C - X$ )  $\alpha$ -bands of R(11) 0–1 transitions, with bandheads at  $5447.912 \text{ \AA}$ ,  $5448.980 \text{ \AA}$ , and  $5450.729 \text{ \AA}$ . To demonstrate the influence of these bands on the atomic spectrum we calculate the TiO spectrum for a Kurucz model atmosphere with  $T_{\text{eff}}=4000 \text{ K}$  and  $\log g=0$ . The spectrum is computed with only TiO lines (*bold solid line*), using a macrobroadening velocity of  $21 \text{ km s}^{-1}$ . The three TiO bandheads are visible, and overplot in the heliocentric frame. The overlapping bands extend and degrade longward over several tens of angstroms, where they merge with other TiO bandheads. The extended TiO line list was computed by Kurucz (1999), based on

semi-empirical calculations by Schwenke (1998). The list includes lines from the five  ${}^Z\text{Ti } {}^{16}\text{O}$  isotopomers ( $Z=46-50$ ), with Earth abundance fractions.

Although the TiO bands at 5447 Å strongly develop in the outburst spectra of  $\rho$  Cas, we found it difficult to compute good fits to determine the atmospheric parameters. This is because these bandheads blend with strong atomic lines complicating our fit procedure. The absorption feature observed between 5447 Å and 5448 Å (heliocentric wavelengths) in the summer of 2000 is due to TiO, but its shape appears rather distorted due to the adjacent atomic lines. We therefore identified other ‘cleaner’ TiO bands that are closer to the stellar continuum level in the echelle spectra. In Figure 11 we identify TiO bands from  $(A - X)$   $\gamma$ -band R(16) 0–0 transitions, with a prominent bandhead at 7052 Å. The bands appear with stronger contrast in Betelgeuse, where they are permanent. The solid vertical lines mark a number of sharp characteristic TiO features that are weakly blended with other atomic and molecular lines. The synthetic spectrum (*dotted lines*) strongly fits the complex TiO spectrum of Betelgeuse with an atmospheric model of  $T_{\text{eff}}=3500$  K and  $\log g=-0.5$ . The line list typically contains  $\sim 1500$  TiO lines per Å, besides many other atomic and molecular species.

The high-resolution spectra show that the distinct TiO absorption features around 7070 Å are broader than sharp telluric lines (of water vapor and  $\text{O}_2$ ), also marked in Figure 11. We compute a best fit to the distinct TiO bands for a model atmosphere with  $T_{\text{eff}}=3750$  K and  $\log g=0$ . For comparison we plot the synthetic spectrum computed with only TiO lines (*upper dotted line*). Models with higher or lower atmospheric temperatures yield intensities for these bands that are too weak or too strong, and do not match the relative intensity of the TiO features. The spectrum is computed with solar abundance for TiO, and scaled to the observed spectrum. The best model obtained from the TiO synthesis is 500 K cooler than the photospheric model computed from the atomic lines in the outburst spectrum (Fig. 6).

The upper panel of Figure 12 compares the high-resolution WHT-UES spectra of  $\rho$  Cas during outburst (2000 July 19 and August 2), and a spectrum observed with NOT-Sofin on 2002 January 29, after the outburst. The spectra show 1.2 Å around the TiO absorption band at 7069.2 Å in the heliocentric wavelength scale. The spectra are continuum normalized, and plotted without vertical shifts. The spectrum of Betelgeuse is also shown (*lower solid line*), together with the synthetic spectrum of Figure 11 (*lower dotted line*). A microturbulence velocity of  $2 \text{ km s}^{-1}$ , and a geometric mean value of  $12 \text{ km s}^{-1}$  for the macrobroadening has been utilized in Betelgeuse (see Lobel & Dupree 2000b). The vertical lines mark only the strongest TiO lines in the list with  $\log gf$ -values above  $-1$ .

The outburst spectrum of  $\rho$  Cas of 2000 July is best fit after broadening the synthetic

TiO spectrum (*upper dotted lines*) with a microturbulence velocity of  $11 \text{ km s}^{-1}$ , and a mean value for the macrobroadening of  $21 \text{ km s}^{-1}$ . The broadening values are obtained after degrading the computed spectrum with the instrumental profile. The cross-correlation with the synthetic spectrum reveals that this TiO band assumes a heliocentric radial velocity of  $-82 \pm 2 \text{ km s}^{-1}$ . It signals an expansion velocity of the TiO line formation region by  $\sim 15$  to  $20 \text{ km s}^{-1}$  faster than we observe for the atomic line spectrum during the outburst. This indicates that the atomic lines form on average deeper in the photosphere, below the TiO formation region. The spectrum of 2002 January 29 (JD 2452303) is observed around the recent  $V$ -brightness maximum with  $T_{\text{eff}} > 6500 \text{ K}$ . The weak TiO bands are therefore not detected. The spectrum also shows that this wavelength region is very close to the stellar continuum level, and does not reveal weak absorptions that could blend with the TiO band. Hence, we can use the band at  $7069 \text{ \AA}$  to reliably estimate the mean gas density in the TiO line formation region during the outburst.

## 8. TiO Formation Region

### 8.1. Model Density

The lower panel of Figure 12 shows that the TiO lines are formed in the selected model atmosphere over a range of optical depths with  $-3 \leq \log \tau_{\text{Ross}} \leq 0$  (*vertical dashed lines*). Deeper in the atmosphere the kinetic temperature  $T$  (*dashed line*) increases to above  $4000 \text{ K}$ , where the TiO molecules dissociate in the chemical equilibrium calculations. On the other hand, TiO molecules do form at  $\log \tau_{\text{Ross}} \leq -3$ , but these outer layers are very optically thin and contribute little to the TiO absorption line formation. The TiO line contribution functions assume largest values in this model for  $3000 \text{ K} \leq T \leq 4000 \text{ K}$ , with negligible contributions outside the corresponding gas density regions.

Hence, we compute that the density  $\rho$  (*solid line*) in the TiO line formation region during outburst ranges between  $-9.8 \leq \log \rho \leq -8.5$ . It is interesting to note that the limited range of gas densities, derived from modeling newly formed TiO bands, are useful to also estimate the gas mass-loss rate during the eruption. Further tests show that a mean formation density during the outburst is much harder to constrain from modeling atomic absorption lines. The atomic lines develop strong asymmetries, with very extended blue line wings that form in a fast expanding low-density wind. The atomic lines thereby form over a much larger density range than the TiO bands. To infer the mass-loss rate from modeling the atomic line profiles would require detailed (semi-empiric) time-dependent models of the velocity- and density-structure of the atmosphere during the outburst, which is outside the scope of the present investigation.

## 8.2. TiO Mass-loss Rate

Based on the outburst spectra we can assume a lower density limit for the TiO line formation region of  $\rho_{\min} = 10^{-10}$  gr cm $^{-3}$ . The distance over which this region expands (assuming spherical geometry) is computed from the radial velocity we observe for the TiO bands. The star velocity of  $-47$  km s $^{-1}$  yields a mean velocity for the TiO envelope expansion of  $-82 + 47 = -35$  km s $^{-1}$ . It corresponds to a travel distance of  $d_s = 869 R_{\odot}$  ( $\sim 2 R_*$ ) over a period of  $\sim 200$  d. The latter is the time which elapsed between the maximum and minimum of the radial velocity curve, observed before the deep brightness minimum (Fig. 1).

During the fast expansion the temperature of the outer atmosphere rapidly plummets to below 4000 K, thereby continuously forming TiO molecules. The photosphere accelerates to very fast expansion velocities ( $\sim 35$  km s $^{-1}$ ), probably causing a circumstellar shock wave. During the brightness decrease the outer atmosphere expands over about twice the stellar radius. This corresponds to a total gas mass lifted above  $R_*$  of  $M_s = 3 \times 10^{-2} M_{\odot}$  ( $= 4 \pi R_*^2 d_s \rho_{\min}$ ) during 200 d. We thus compute a mass-loss rate of  $\dot{M} = 5.4 \times 10^{-2} M_{\odot} \text{ yr}^{-1}$  during the eruption. This value is 587 times larger than the mass-loss rate of  $9.2 \times 10^{-5} M_{\odot} \text{ yr}^{-1}$ , derived by Lobel et al. (1998) for the pulsation phase of 1993 December. For comparison, during the 200 days the hypergiant sheds the same amount of mass it normally would over a period of 3000 years by quiescent pulsation with  $\dot{M}$  below  $10^{-5} M_{\odot} \text{ yr}^{-1}$ .

The value of  $\dot{M} = 5.4 \times 10^{-2} M_{\odot} \text{ yr}^{-1}$  we calculate for the 2000-01 outburst is a *lower limit* since the lower limit of the density-range and  $R_* = 400 R_{\odot}$  are adopted to estimate a spherical mass-loss rate. We emphasize that the combination of the density- and kinetic temperature-range obtained in § 8.1 is required to correctly compute the intensity ratios observed across the newly formed TiO bands. Although we utilize a hydrostatic model atmosphere to perform the radiative transport calculation, this combination of density- and kinetic temperature-range, providing the correct relative band intensities, is also required in more realistic dynamic models. During the outburst the atmosphere likely assumes a very different density structure than that of a hydrostatic model, but the TiO fit procedure will require similar mean gas densities and kinetic temperatures in an expanding atmosphere. On the other hand, we should also mention that the geometric position of the TiO formation layers, having the required thermal conditions in a hydrostatic model, is very likely different from the location that these layers will assume in a hydrodynamic model. Dynamic models that are more extended than static models (i.e. with TiO opacity at larger atmospheric radii), yield larger mass-loss rates in the TiO formation region. This is also the case when using plane-parallel models instead of spherically symmetric models. The TiO bands computed in spherical symmetry yield smaller line depths (for the same atmospherical model parameters),



because the light rays that graze the atmosphere escape earlier from a curved model than from a plane-parallel model. The best fit calculated with spherical geometry hence requires larger gas densities in the TiO formation region than for a plane-parallel model, assuming that the mean optical depth is not appreciably different for both types of models. The latter assumption is justified here because the best fit indicates that the optical depth of the weak TiO bands is large ( $-3 < \log \tau_{Ross} < 0$ ), or that these bands form at (sub-)photospheric levels where the bulk of the atomic line spectrum emerges. Larger differences are expected toward smaller optical depths with  $\log \tau_{Ross} < -3$ , where the extended violet wings of the atomic lines are formed in a much faster expanding wind. Best fits to the new TiO bands using more extended dynamic and spherical models are therefore expected to provide larger  $\dot{M}$ -values than the lower limit we estimate from static plane-parallel models.

The present outburst observations, together with the outbursts of 1893, 1945-47, and 1985, indicate that the eruptions of  $\rho$  Cas occur on time-scales of about half a century. For an average mass of  $3 \times 10^{-2} M_{\odot}$  expelled during these events, the star would lose  $20 M_{\odot}$  during a period of only 33,750 years (over 675 outbursts). Since the current mass of  $\rho$  Cas is expected not to exceed  $40 M_{\odot}$  from evolutionary calculations, and since this time span (or an order of magnitude longer) is comparable to the evolutionary life time during the post-red supergiant phase, we infer that the recurrent eruptions, causing punctuated mass-loss episodes, are likely the major mass-loss mechanism for this massive hypergiant.

## 9. Is $\rho$ Cas Bouncing Against the Yellow Hypergiant Void?

De Jager & Nieuwenhuijzen (1997) suggested that the recurrent eruptions in yellow hypergiants occur when these stars approach the cool boundary of the ‘yellow void’, and bounce off redward. The evolutionary void is an area in the upper HR-diagram around  $T_{\text{eff}} \sim 10,000$  K with  $\log L/L_{\odot} \geq 5.7$ , which is nearly devoid of (white) supergiants. Their detailed calculations revealed that hydrostatically stable solutions cannot be computed for the atmospheres of *blueward* evolving yellow hypergiants at a low boundary of  $T_{\text{eff}} \simeq 8300$  K. The effective acceleration becomes negative, or directed outward, causing an unstable atmosphere above 8300 K. In a review on hypergiants de Jager (1998) suggested that the mechanism for outbursts may be related to increased pulsation velocities during a period of instability when the star, during rapid blueward evolution, increases its pulsation amplitudes. This ‘bouncing against the void’ may explain why most of the cool hypergiants cluster near this low-temperature boundary.

Another evolutionary aspect of yellow hypergiants is their possible connection with the S Dor variables. In a recent review on these hotter luminous stars, van Genderen (2001)

addressed the question if fast evolving yellow hypergiants are in fact proto-S Dor variables, as proposed by de Jager (1998). This can be supported by noting that both types of variables are evolving blueward, and that the void may provide a temporal obstacle at which the unstable atmosphere of the yellow hypergiant is fastly transformed into that of a more stable (less luminous) S Dor variable. The void could thus be considered as a stellar atmospherical phenomenon, during rapid blueward evolution, which causes a natural separation between two distinct classes of luminous stars -the Luminous Blue Variables (LBV) and the cool hypergiants- with essentially the same, or comparable, evolutionary life-times. The segregation possibly only occurs during the post-red supergiant phase after a yellow hypergiant, at the cool border of the void, has shed sufficient amounts of mass during recurring phases of punctuated mass-loss (outbursts) that quickly strip off its extended atmosphere. Such a scenario for the evolution of massive stars would imply that the instantaneous stellar mass is a fundamental parameter which determines at what point during blueward evolution a yellow hypergiant makes the transit across the void. In other words, the bouncing against the void occurs only if the blueward evolutionary track is sufficiently fast to quickly approach the cool border of the void. Less luminous (i.e. less massive) yellow hypergiants require more time with quiescent mass-loss before the recurrent outbursts can develop. It can explain why recurrent outburst have not been observed in many other galactic yellow hypergiants so far, although they bear the spectroscopic signatures of a cool hypergiant. Presumably,  $\rho$  Cas is therefore one of the most massive known yellow hypergiants, quickly heading to the point of transiting the void.

The above considerations in this section are rather tentative, but it is of note that advanced evolutionary calculations of massive supergiants do adopt average mass-loss rates during the yellow hypergiant phase that are compatible with the observed values of about  $20 M_{\odot}$  during 33,750 yr. The blueward tracks in these simulations (Meynet et al. 1994) last for  $\sim 49,000$  yr with  $\log L/L_{\odot}=5.33$  during this period, and only 6500 yr when  $\log L/L_{\odot}=5.77$ . In other words, the high mass-loss rates in these calculations yield very short-lived blue loops over which the yellow hypergiants cross the upper portion of the HR-diagram, thereby considerably diminishing the stellar mass, by about halving it. The recurrent outbursts of  $\rho$  Cas could therefore be a major cause which quickly transforms the yellow hypergiant into a hotter less massive hypergiant. We note that mass-loss estimates for the Giant and Lesser eruptions of the LBV  $\eta$  Car, by  $\sim 50$  years apart, of  $7 \times 10^{-2} M_{\odot} \text{ yr}^{-1}$  (Davidson & Humphreys 1997) are of the same order of magnitude as we observe for the outburst of  $\rho$  Cas.

To conclude this section, we should point out that cool hypergiants as  $\rho$  Cas are the prime candidates for progenitors of type II supernovae (SN). Their actual evolutionary phase remains poorly understood. The He-core burning phase of cool hypergiants is likely accom-

panied by tremendous episodic mass-loss events as presented here. If these stars lose half of the current mass in only a few tens of thousand years, it will lead to an active reconstruction of the stellar interior. Lessons from SN 1987A teach that we should monitor, by all possible means, a number of galactic type II SN progenitor candidates (such as the cool hypergiants), if we aim to understand the relationship between the mass of the progenitor and the mass of the compact SN remnant.

## 10. Comparison With Previous Outbursts of $\rho$ Cas

### 10.1. V-band Brightness Curves

Figure 13 compares the  $V$ -brightness curve observed during the three outbursts of  $\rho$  Cas in the last century. The upper panel shows the 2000-01 outburst, the middle panel the moderate outburst of 1985-87, and the lower panel the famous eruption of 1945-47. The three panels are plotted for the same time intervals and  $V$ -magnitude range, so that the outburst properties can be compared. Photo-electric  $V$  observations in 1985-87 (*solid dots in middle panel*) are from Leiker & Hoff (1987), Leiker et al. (1988), and Leiker, Hoff, & Milton (1989). Visual magnitudes during this period (*solid boxes in middle panel*) are offered by AFOEV<sup>5</sup>. The light curve during 1945-47 is from photographic and visual observations (*solid dots in lower panel*) listed in Gaposchkin (1949). The light curve before the brightness decrease of 1945 August is obtained from Payne-Gaposchkin & Mayall (1946) (*open symbols in lower panel*). The open circles are 20-day means with five or more photographic estimates, while the open boxes show two to four estimates. Visual brightness estimates from AAVSO during the 1946 outburst are also shown in Figure 1 of Beardsley (1961).

The brightness decrease lasted for  $\sim 660$  d during the entire outburst of 1945-47, with a very steep increase and rather symmetric decrease of  $1^m.5$  in  $V$  (Gaposchkin 1949). A lesser brightness decrease was observed during the outburst of 1986, with a (visual) dimming of only  $\sim 0^m.5$ , and a (photo-electric) brightness increase of  $\simeq 0^m.7$ . This event lasted for 550 d, but with a shallower brightness decrease and increase. The recent outburst of 2000-01 is more pronounced as the previous one, but a remarkable strong brightness maximum precedes the deep minimum in the fall of 2000. However, the entire outburst occurred over a much shorter time span of less than 500 d. The phases with the deep brightness minima therefore appear to have considerably shortened over the three outbursts; from  $\sim 400$  d in 1946, to  $\sim 200$  d in 1986, to  $\sim 100$  d in late 2000 (see also Hassforther 2001).

After the deep minimum of 1986 the  $V$ -brightness declined, along with a steady decline of the variability amplitude over time (see also Zsoldos & Percy 1991). The brightness

maximum after the deep minimum is followed by three declining brightness cycles, while returning to the mean magnitude level before the outburst. It signals pulsation phases over which the photosphere ‘relaxes’ to the initial conditions. The outbursts are followed by cycles of decreasing pulsation compression while the atmosphere gradually settles to the star’s gravitational potential well by dissipating the excess energy released by the explosion into the circumstellar environment (possibly somewhat similar to a bouncing ball losing height by friction).

## 10.2. Recurrent TiO bands

The vertical lines in the upper panel of Figure 13 mark our high-resolution spectroscopic observations, while spectroscopic observation dates quoted in the literature are marked for the other outbursts in the lower panels. The dates when TiO was observed in the spectrum are connected with a horizontal line and labeled with TiO. Popper (1947) was the first to report the observation of TiO bands in the spectrum of 1945 October of  $\rho$  Cas (see also Keenan 1947), shortly *before* the decline in light started. Interestingly, he also mentions that: “A spectrogram obtained by Struve in August, 1944, before the light had started to fade, shows that the spectroscopic changes were already well underway, although the TiO bands had not yet appeared.” It is important to point out that the outburst of 1945-47 was preceded by a pre-outburst cycle (JD 2431000 – JD 2431600), similar as we observe before the outburst of 2000-01 between JD 2451000 and JD 2451600. During the latter period, we do not find indications for TiO in the spectra (*labeled with numbers 39 – 63 in the upper panel*), although the spectra observed around the brightness minimum appear to be of a later spectral type (G–K). Our observations confirm Popper’s statement that TiO is not observed during the pre-outburst cycle of 1944 (*labeled ‘no TiO’ in the lower panel*).

We detect TiO bands in the WHT-UES spectra of 2000 July and August (*Nos. 64 & 65*), *before* the deep brightness minimum is reached in late September 2000. The presence of TiO before the deep minimum of 1946 is also stated by Beardsley (1961). A spectrum obtained by Bidelman in 1945 October, a short time after the decline to the deep minimum had commenced shows TiO bands, although the star was still fairly bright. On the other hand, the WHT-UES spectrum of 2001 February 5 (*No. 69*) does not contain discernible TiO bands. During the four months before this observation the star quickly brightens up by  $\sim 0^m.3$ , while the expansion velocity of the deeper photosphere strongly decelerates, and begins to collapse during the deep brightness minimum (*solid dots connected by the dotted line in upper panel are  $V_{\text{rad}}$ -values from Fe I; the other solid dots are values from ORO*). The spectra obtained between 2001 February and 2002 February (*Nos. 69 – 77*) do not

show TiO bands. These observations confirm the observations by Beardsley (1961) that TiO was no longer present in his spectra observed after 1947 May. He also mentions that Thackeray (1948) found that in 1947 April (around JD 2432280), when the star was on the rise to full brightness, the TiO bands were still present, although “almost gone”. Thackeray (1948) makes the remarkable statement that by 1947 April the absorption lines resumed their sharp(er) supergiant character of 1939 (observed before the outburst by Tai & Thackeray 1948). By comparing different wavelength portions of the spectrum with  $\mu$  Cep (M2) and  $\beta$  Cam (G1) he concludes that: “The temperature corresponding to the lines spectrum seems to vary from 5500 deg. in the green to 3500 deg. in the red.” In other words, the outburst spectra of 1945-47 and 2000-01 show that TiO bands occur throughout the period of brightness decline *and* the period of rise as well.

These observations show that the deep brightness minimum during the outbursts is not the primary cause for the formation of molecular bands in the spectrum. They rather indicate that the bands can form when only the upper atmosphere expands beyond a certain threshold velocity. For example, the TiO bands do not form during the pre-outburst cycle of 1999 because the photospheric expansion velocity does not exceed  $10 \text{ km s}^{-1}$  (with respect to the stellar rest frame), while in the summer of 2000 the expansion velocity increases to  $18 \text{ km s}^{-1}$ , and TiO is observed. The molecular bands are produced by rapid cooling of their outer formation region, which results from the unusual fast expansion of the entire atmosphere. It follows from our observations that the time-scale for the formation of the TiO bands is less than 100 d (between JD 2451650 and JD 2451744). Conversely, the collapse of the deeper photosphere raises the kinetic temperature in the molecular line formation region, which ceases to produce metal-oxides. The disappearance of these peculiar molecular bands after the deep minimum is not the result of the strong brightness increase only. Greenstein (1948) and Beardsley (1961) observe AlO in spectra of 1947 September and November (after JD 2432430), when TiO was no longer present. The AlO bands also disappear after that time, but they were observed during a period when the stellar brightness had returned to normal levels (Fig. 13, *lower panel*). It confirms that the appearance of newly formed molecules with the outbursts of  $\rho$  Cas chiefly results from the exceptional dynamics of the atmosphere during these events. Note further that we do not observe AlO in the outburst spectra of 2000-01. On the other hand, many broad absorption features develop in these complex spectra suggesting newly formed molecular bands, but which however still defy identification.

### 10.3. Blue H $\alpha$ Emission Before Outburst and Na $D$

Boyarchuk, Boyarchuk, & Petrov (1988) also observe the appearance of the TiO band at 5448 Å (§ 7.5) in 1986 February (JD 2446450 in Fig. 13). The band becomes gradually deeper and assumes maximum strength in 1986 May. It is still present in 1986 July, but disappears completely in 1986 August. They also monitored H $\alpha$  during the shallow brightness minimum (see their Fig. 5). The high-resolution spectra show that a very strong emission wing is present in the blue H $\alpha$  absorption core in 1984 November (JD 2446000), before the brightness decline. Strong emission in the blue wing of H $\alpha$  is also observed during the pre-outburst cycle of 1999. They further show that the H $\alpha$  absorption core becomes conspicuously weak during the deep brightness minimum of mid 1986, as we observe during the deep outburst minimum of late 2000 (§ 7.2). Note however that these authors do not observe central emission above the continuum in Na  $D$ , which also confirms a smaller continuum (hence  $T_{\text{eff}}$ ) decrease during the event of 1986. During the minimum of 1946 the broad absorption cores of Na  $D$  completely vanish, and weak emission lines appear above the continuum level (Fig. 1 of Thackeray 1948). Weak H $\beta$  and H $\gamma$  lines are observed during the deep minimum, with the presence of core emission in H $\alpha$  (Beardsley 1961).

The spectroscopic observations during the three outbursts of  $\rho$  Cas in the last century reveal remarkably similar evolutions of the detailed line profiles. These similarities indicate that the outbursts result from a driving mechanism which produces phases of fast photospheric expansion and rapid decreases of  $T_{\text{eff}}$ , which causes a substantial cooling of the outer atmosphere. In the next section we investigate the physical origin of this driving mechanism.

## 11. Outburst Mechanism

### 11.1. Dynamic Atmospheric Stability

In a study of atmospheric dynamic instability of red supergiants Paczynski & Ziolkowski (1968) were the first to simulate the ejection of a stellar envelope as a possible formation mechanism of planetary nebulae. They found that at sufficiently high luminosity, convective envelopes develop that are dynamically unstable, due to the low value of the first generalized adiabatic index  $\Gamma_1 \equiv (d \ln P / d \ln \rho)_{\text{ad}}$  in the thick zones of partial ionization of hydrogen and helium. The total energy of the envelope becomes positive or unbound when recombination of the ionized hydrogen and helium is taken into account. This was first conjectured by Lucy (1967), who suggested that planetaries may form when the mass contained in the hydrogen ionization zone is sufficient to reduce the specific heat ratio of the envelope to below 4/3. In more sophisticated numerical simulations Tuchman, Sack, & Barkat (1978) found that the

envelope becomes dynamically unstable, and mass is being expelled as a series of short-time events. The mass-loss process results from repetitive shock ejections, where the red giant loses about 3% of its prevailing envelope per ejection. During the event the mean envelope density decreases by an order of magnitude, and the region with  $\Gamma_1 < 4/3$  displaces toward the deeper mass layers with the release of recombination energy (*see their Figs. 3 & 4*). Interestingly, in a subsequent paper Tuchman, Sack, & Barkat (1979) simulated dynamically stable, but pulsational unstable envelopes, and demonstrated how a shell ejection event can occur after about 10 to 15 stable pulsation cycles. The radial pulsation amplitudes increase over time, up to a point where 20% of the outer envelope attains the escape velocity and is ejected (see their Fig. 12). The time interval between successive ejections is  $\sim 30$  years, which is close to the envelope’s thermal time-scale (Tuchman 1983). Wagenhuber & Weiss (1994) computed with a hydrostatic code, fast envelope ejection in Asymptotic Giant Branch models, caused by the recombination of hydrogen. Whether an ionization-recombination mechanism can eject planetary nebulae remains presently unanswered because a time-independent treatment of convection is assumed in these simulations. More recently, Harpaz (1998) also showed that mass ejections from giants could be complicated by the decrease of electron opacity during hydrogen recombination. Other hydrostatic calculations by Jiang & Huang (1997) indicate possible effects of turbulent pressure for mass ejections from surface layers. All these studies appear to suggest that an ionization-recombination driving mechanism is an important candidate for the origin of outbursts in cool luminous stars as  $\rho$  Cas. Note that more recently, Stothers & Chin (1997) also computed that an ionization-induced dynamic instability mechanism (with  $\Gamma_1 < 4/3$ ) can cause strong eruptive mass-loss for massive hot stars (i.e. LBVs as S Dor that also exhibit sudden spectral changes; see Massey 2000), and argued against a supercritical radiative acceleration for such events. A number of other outburst mechanisms for hot supergiants have also been suggested in the literature. ‘Geysers models’ and ‘violent mode-coupling instabilities’ have been reviewed and compared by Humphreys & Davidson (1994).

In the next paragraph we investigate the ionization-recombination mechanism for the outburst of  $\rho$  Cas. Based on hydrostatic calculations we provide arguments in favor of driving by a thermal runaway mechanism that causes the eruption. The main goal is to derive an analytic expression which correctly predicts the time-scale for the changes of  $T_{\text{eff}}$  during the outburst, based on the observed stellar parameters, and the hydrogen recombination energy. We show that our equation is also valid for other variable eruptive cool stars.

## 11.2. Ionization-recombination Driving

We demonstrate first that pure thermal expansion of an ideal hydrogen gas cannot provide sufficient energy to accelerate the atmosphere to an outburst. This results from the conservation of total energy. Consider a gas element with flow velocity  $v$  at a distance  $r$  in the atmosphere. The total energy of this element per unit mass is

$$\frac{1}{2}v^2 + e + \frac{P}{\rho} - \frac{G M_*}{r} = \text{const.}, \quad (4)$$

where  $e$  is specific internal energy (expressed per unit mass),  $P$  the local gas pressure, and  $\rho$  the mass density. For the specific internal energy of an ideal gas  $e = 3/2 N k T$ , due to the translational motion of the gas particles in the parcel, with an equation of state  $P = N k T \rho$ , the differential of equation (4) yields

$$-v \Delta v = \frac{5}{2} N k \Delta T + g_* \Delta r, \quad (5)$$

where  $k$  is the Boltzmann constant,  $N$  the number of particles per unit mass, and  $g_*$  the atmospheric gravity acceleration (at  $r=R_*$ ). Equation (5) provides an estimate of the acceleration of the gas element due to the change of the local temperature, assuming that its total energy per unit mass remains constant. Since we observe that the kinetic temperature in the atmosphere decreases by  $\Delta T \simeq -3000$  K during the outburst, with an outflow velocity of  $v=35 \text{ km s}^{-1}$  for the TiO bands in § 8.2, we compute that its corresponding acceleration  $\Delta v$  would not exceed  $2 \text{ km s}^{-1}$  (when neglecting the gravity acceleration). We observe, however, that the radial velocity increases to an expansion velocity above  $30 \text{ km s}^{-1}$  during the outburst. When including the gravity term in equation (5), the outward acceleration due to pure thermal expansion of the gas element, decreases to  $\Delta v < 2 \text{ km s}^{-1}$ .

However, if we consider instead the internal energy of a partially ionizing hydrogen gas  $e = 3/2 N k T(1+x) + N I_{\text{H}} x$ , with  $x$  the local ionization fraction ( $0 \leq x \leq 1$ ), and an equation of state that includes the electron pressure of the gas element  $P = N k T \rho(1+x)$  (hence the number of electrons per unit mass is  $N_e = x N$ ), the differential of equation (4) yields

$$-v \Delta v = \frac{5}{2} N k \Delta T (1+x) + \frac{5}{2} N k T \Delta x + N I_{\text{H}} \Delta x + g_* \Delta r, \quad (6)$$

where  $I_{\text{H}} = 13.6 \text{ eV}$  is the ionization energy of hydrogen. We assume that all translational energy of the free electrons is converted into accelerating the gas element due to ionization-recombination during cooling, and the hydrogen gas thereby almost completely recombines, hence  $x \simeq 0$  and  $\Delta x \simeq -1$ . For an average local temperature of  $T=2500 \text{ K}$ , with  $v=35 \text{ km s}^{-1}$ , we compute with equation (6) for  $\log g_* = -0.5$  and  $\Delta r \simeq R_*$  that  $\Delta v \simeq 19 \text{ km s}^{-1}$ . If the mean



atmospheric gravity acceleration decreases further to  $g_*=0.1 \text{ cm s}^{-2}$  during the outburst, the acceleration of the gas element increases to  $\Delta v \simeq 37 \text{ km s}^{-1}$ . This value corresponds to the observed change of expansion velocity during the outburst of  $\rho \text{ Cas}$ . It results from the release of ionization energy stored in the gas. The third term on the r.h.s. of equation (6) is the ionization energy content, which provides the major contribution to the change of total internal energy at relatively low atmospheric temperatures. These approximate calculations show that the conversion of thermal (translation) energy only is insufficient to increase the outflow velocity to the observed values. The release of hydrogen ionization energy is required to adequately drive the outburst.

### 11.3. Temperature Dependence

In this section we investigate the ionization-recombination driving mechanism of  $\rho \text{ Cas}$ ' outburst with a more detailed numerical calculation. We show that the observed time-scale, and the expansion velocity of the outburst can be well predicted from an adiabatic hydrostatic calculation in spherical geometry. We emphasize however that this discussion does not involve a detailed solution of the momentum equation to compute the time-evolution of the dynamic and thermal wind structure. The presented calculations rather consider the driving properties of different atmospheric layers, that result from the conservation of total energy and mechanical flow momentum at different temperatures. The full hydrodynamic treatment of the outburst would require a time- *and* temperature-dependent solution of the conservation equations. This would demand, however, the detailed knowledge of the physical mechanism by which ionization-recombination energy is converted into wind momentum (possibly due to electron scattering), besides the adiabatic expansion of the atmosphere. The driving mechanism is opacity dependent, which therefore also depends on the local gas temperature and density. Consequently, the atmospheric opacity also determines the detailed cooling properties during the outburst. With hydrogen recombination the (electron) opacity falls rapidly, thereby diminishing the driving force by the free flow of radiation. We also emphasize that the calculations do not consider radiative damping, or that we neglect possible radiation loss terms in the energy balance equation. This approximation assumes that the energy released by the recombining gas elements is entirely converted into flow momentum which drives an expansion. In this respect, we adopt a 'fully optically thick' limit to evaluate the energy and momentum balance of the outflow, and demonstrate that this assumption provides good agreement with the observations. The amount of radiative damping can possibly be determined by modeling the  $H\alpha$  line profile, to determine its optical thickness and the energy in the emission of the transition. The radiative losses are dependent on the atmospheric opacity, which includes the density dependent electron opacity. Presumably,

laboratory experiments performed at smaller electron densities could be useful to determine the importance of increased radiative recombination of hydrogen, compared to the three-body recombination observed for high densities (Fill et al. 2000).

We assume that the total energy of every gas (mass) element at temperature  $T$  in the expanding atmosphere is constant and given by equation (4), with the material gas pressure  $P = N k T \rho(1 + x)$ . The constant equals  $e_0$ , or the total energy the element assumed before the acceleration. Since we can suppose that the outburst is preceded by a compressed atmosphere which is almost static (or  $v_0 = 0$ ), the initial internal energy  $e_0 = 5/2 N k T_0 (1 + x_0) + N I_H x_0$ .  $T_0$  is the initial temperature of the gas element, and  $x_0$  its corresponding ionization fraction. For further calculations we can neglect the small contribution of the potential energy of gravity. Hence, the energy conservation equation for atmospheric gas elements is given by

$$\frac{1}{2}v^2 + \frac{5}{2} N k T (1 + x) + N I_H x = \frac{5}{2} N k T_0 (1 + x_0) + N I_H x_0, \quad (7)$$

and the r.h.s. remains constant with the changes of  $T$ ,  $x$ , and  $v$ , during the expansion. We further assume that the total mechanical momentum  $1/2\rho v^2 + P$  of every gas parcel remains constant along a flow line in the expanding atmosphere, and equals the layer pressure of the static atmosphere  $P_0$  before the expansion. Hence the Bernoulli equation yields

$$\frac{1}{2} \rho v^2 + P = P_0. \quad (8)$$

The LTE Saha equation is used to compute the changes of the thermal ionization fraction  $x$  during the expansion. Since  $x$  is a function of  $T$  and  $P$ , the ionization equation, together with the conservation of energy and momentum (Eqns. 7 & 8), define a set of coupled equations that can iteratively be solved with an equation of state of partially ionized hydrogen gas.

Figure 14 shows the expansion velocity  $v$  of the gas element computed for different temperatures  $T$  (*bold lines*). The gas acceleration curves are calculated for three different gas parcel momenta of  $0.1 P_0$  (*dashed line*),  $P_0$  (*solid*),  $10 P_0$  (*dash-dotted*), assuming  $T_0=8000$  K. For  $6000 \leq T \leq 8000$  K the gas remains nearly fully ionized ( $x=1$ ) (*thin lines*), and  $v$  does not exceed  $\sim 17 \text{ km s}^{-1}$ . Note that the addition of gravitation would decrease the computed flow velocities, although the computed  $v - T$  dependence remains similar. For  $4000 \leq T \leq 6000$  K, we find that  $v$  rapidly increases to  $\sim 70 \text{ km s}^{-1}$ , and assumes a constant value toward lower kinetic temperatures. The fast acceleration in this temperature range results from the release of ionization energy by hydrogen recombination. An important property of these curves is that the fast acceleration occurs over a kinetic temperature range of  $\sim 3000$  K, independent of the total parcel momentum. This range corresponds to the mean atmospheric temperature change we observe for the outburst of  $\rho$  Cas. An increase

(decrease) of the momentum displaces the region of fast acceleration toward higher (lower) temperatures, but the width of the temperature range remains unaltered. This limited range is determined by the kinetic temperature dependency of thermal hydrogen ionization, which supports that the outburst is driven by hydrogen recombination. The bold dotted line is the velocity computed for a gas element without ionization energy ( $x=0$ ) and  $e_0=5/2 N k T_0$ . It reveals that pure thermal expansion cannot provide the observed outflow velocities above  $30 \text{ km s}^{-1}$  in atmospheric layers of lower temperature.

For  $T \leq 4000 \text{ K}$  the fast velocity acceleration levels off due to the conservation of total energy. In the partial hydrogen ionization zone (around  $x \simeq 0.5$ ) gas parcels become very expandable because the local adiabatic indices  $\Gamma_1 - 1$  and  $\Gamma_3 - 1$  assume minimum values. The inverse values are shown in Figure 14 for hydrogen recombination. However, when the atmospheric layers nearly fully recombine ( $x \simeq 0$ ),  $1/(\Gamma_1 - 1)$  and  $1/(\Gamma_3 - 1)$  decrease, or the adiabatic expansivity diminishes. At low temperatures the outflow stalls with the decrease of recombination driving, and the smaller adiabatic expansivity. The outward driving forces therefore vanish, and the recombined hydrogen gas assumes conditions of maximum gravitational potential energy at low kinetic temperatures.

Figure 15 shows the solution of the above considered system of equations for every mass layer of the photospheric model with  $T_{\text{eff}}=7250 \text{ K}$  and  $\log g=1.0$ , determined for the pre-outburst condition of  $\rho \text{ Cas}$  (§ 7). The upper panel shows the model kinetic temperature structure (*bold solid line*), which together with the gas pressure structure, provides the input values  $T_0$  and  $P_0$  to calculate the ionization-recombination acceleration of the model layers. For Rosseland optical depths  $-0.5 \leq \log \tau_{\text{Ross}} \leq 0.5$  the hydrogen ionization fraction  $x$  (*thin solid line*) steeply increases from nearly zero to unity. For this model  $\Gamma_1$  (*thin short-dash dotted line*) assumes values below the value for atmospheric dynamic stability of  $4/3$  (*horizontal dotted line*) over the entire upper fraction at  $\log \tau_{\text{Ross}} \leq 0.5$ . It signals an enhanced adiabatic expansivity for the upper atmospheric layers. Since the third adiabatic index is defined by  $\Gamma_3 - 1 = -(d \ln T / d \ln V)_{\text{ad}}$ , and  $\Delta V / V = 3 \Delta r / r$  in spherical geometry, the relative radius increase for every mass layer with spherical adiabatic expansion is

$$\frac{\Delta r}{r} = \frac{1}{3} \frac{(-\Delta T)}{T} \frac{1}{\Gamma_3 - 1}. \quad (9)$$

Detailed LTE expressions of  $\Gamma_3 - 1$  for singly-ionizing monatomic gas mixtures with equilibrium radiation are provided in Lobel et al. (1992). We presently limit the calculations to thermal hydrogen ionization without equilibrium radiation, for which (e.g. Mihalas & Weibel Mihalas 1984)

$$\Gamma_3 - 1 = \frac{c_p - c_v}{c_v} \frac{\chi_\rho}{\chi_T} = \frac{1 + (x/2)(1-x)(5/2 + I_{\text{H}}/(kT))}{3/2 + (x/2)(1-x)(3/2 + (3/2 + I_{\text{H}}/(kT))^2)}, \quad (10)$$

where  $c_p$  and  $c_v$  are the heat capacities, and  $\chi_\rho$  and  $\chi_T$  the isothermal and isochoric factor, respectively.

The upper panel of Figure 15 shows the temperature structure of the photospheric model with  $T_{\text{eff}}=3750$  K and  $\log g=0$ , obtained from the TiO outburst spectrum (*bold long-short dashed line*). This temperature structure is assumed after outburst, and can be well approximated by lowering the kinetic temperature of the gas layers in the pre-outburst model (with  $T_{\text{eff}}=7250$  K) by  $\Delta T_{\text{eff}}/T_{\text{eff}}$ , with  $\Delta T_{\text{eff}}=-3500$  K (*bold dash-dotted line*). Hence, we can assume that the outburst diminishes the temperature  $T_0$  of each layer by  $\Delta T = T_0 \Delta T_{\text{eff}}/T_{\text{eff}}$ , which yields with equation (9) an adiabatic radius change of

$$\Delta r = \frac{r}{3} \frac{(-\Delta T_{\text{eff}})}{T_{\text{eff}}} \frac{1}{\Gamma_3 - 1}. \quad (11)$$

With the cooling of the layer temperatures to  $T = T_0 + \Delta T$ , we compute the corresponding layer accelerations from the conservation of total energy and momentum. The velocity increase from static initial conditions is shown by the bold solid line in the lower panel of Figure 15. We calculate a maximum layer expansion velocity of  $36-37 \text{ km s}^{-1}$  at  $\tau_{\text{R}} \simeq 1$ . Around these optical depths, the hydrogen ionization fraction  $x$  strongly decreases during the outburst because the gas is partially ionized over this region of the atmosphere (*thin solid line in upper panel*). Hydrogen gas can therefore recombine more by the decrease of the local temperature than in the neutral or fully ionized atmospheric regions. The decrease of  $x$  is shown by the thin long-dash dotted line in the upper panel. The adiabatic expansion velocity in the lower panel peaks in layers where  $\Delta x$  is largest. It is of note that toward the deeper atmosphere at  $\tau_{\text{R}} > 10$ , the adiabatic expansion velocity increases, although hydrogen remains nearly fully ionized. It results from pure thermal expansion with the decrease of the kinetic temperature in conditions of larger density. However, in these layers the adiabatic expansivity  $1/(\Gamma_3 - 1)$  is much smaller than for layers at  $\tau_{\text{R}} < 10$  (*thin short-dash dotted line in lower panel*). With equation (11) we calculate that these deeper atmospheric layers expand over much shorter distances during the outburst. For example, the relative radius increase  $\Delta r/r$  (*thin dashed line*) at  $\tau_{\text{R}}=1$  is  $\simeq 2.5$  near the maximum of expansion velocity, whereas  $\Delta r/r$  decreases to below 30% at  $\tau_{\text{R}} > 10$ . We compute that the adiabatic expansion time  $t_{\text{ad}} = \Delta r/v$  (*thin solid line*) of atmospheric layers at a distance  $r=R_* \simeq 400 R_\odot$  ranges between 170 and 267 d for  $-3 < \log \tau_{\text{R}} < 0.5$ . We therefore conclude that the close correspondence of  $t_{\text{ad}}$  with the observed time-scale of  $\sim 200$  d, over which  $T_{\text{eff}}$  decreases from 7250 K to  $\leq 4000$  K, indicates a quasi-adiabatic spherical expansion of the entire upper atmosphere during the outburst, driven by the release of hydrogen ionization energy due to complete recombination. After the outburst the value of  $\Gamma_1$  increases to above  $4/3$  in the region where  $\Delta x$  is maximum, and hence the inflated atmosphere becomes dynamically stable (*long dashed line in upper panel*).

#### 11.4. Outburst Time-scale

From the considerations in the previous section we derive a more general equation for the time-scale of recombination-driven stellar outbursts. Since the maximum expansion velocity occurs in the partial ionization layers of the pre-outburst atmosphere where  $x_0 \simeq 0.5$ , the adiabatic outburst velocity, due to complete recombination to  $x \simeq 0$  in this region, is approximated with equation (7):

$$v^2 \simeq 5 N k (-\Delta T) + 5 N k (T_0 x_0 - T x) + 2 N I (-\Delta x), \quad (12)$$

where  $I$  is the energy of the recombining ionization stage of the driving element under consideration. Hence, for  $\Delta x \simeq -1/2$ , with a temperature change of  $\Delta T$  in layers of  $T_0$ , equation (12) casts to:

$$v^2 \simeq 5 N k T_0 \left( \frac{1}{2} - \frac{\Delta T_{\text{eff}}}{T_{\text{eff}}} \right) + N I. \quad (13)$$

The adiabatic index of volume expansion in the partial ionization region with  $x_0 \simeq 0.5$  simplifies with equation (10) to

$$\Gamma_3 - 1 = \frac{21 + 2 I / (k T_0)}{27 + 2 (3/2 + I / (k T_0))^2}. \quad (14)$$

The outburst time (over which  $T_{\text{eff}}$  decreases by  $-\Delta T_{\text{eff}}$ ), driven by the recombining atmospheric region around  $T_0$ , is obtained with equations (11), (13), and (14)

$$t_{\text{burst}} = \frac{\Delta R_*}{v} \simeq \frac{R_*}{3 \sqrt{N k T_0}} \frac{(-\Delta T_{\text{eff}} / T_{\text{eff}})}{\sqrt{5/2 - 5 \Delta T_{\text{eff}} / T_{\text{eff}} + I'}} \left( \frac{27 + 2 (3/2 + I')^2}{21 + 2 I'} \right), \quad (15)$$

where we denote  $I' = I / (k T_0)$ . The first two factors at the r.h.s. of equation (15) result from gas dynamics (total energy conservation and spherical geometry), whereas the last factor is of thermodynamic origin (adiabaticity). The last two factors are dimensionless. For the outburst of  $\rho$  Cas, we compute  $t_{\text{burst}} = 221$  d for  $R_* = 400 R_\odot$ ,  $T_{\text{eff}} = 7250$  K,  $\Delta T_{\text{eff}} = -3500$  K, and  $T_0 = 8,000$  K in the partial hydrogen ionization zone. For supergiant atmospheres composed of hydrogen  $I'_H = 19.7$ . However, for pulsating supergiants with hydrogen deficient atmospheres, for which outbursts can be driven by the first recombination of helium, equation (15) predicts much shorter time-scales. For example, for R CrB, a Ib-supergiant with  $T_{\text{eff}} \simeq 6900$  K and  $R_* = 80 R_\odot$ , we compute for  $T_0 = 13,000$  K in the first helium recombination zone ( $I'_{\text{He}} = 24.58$  eV and  $I'_{\text{He}} = 21.9$ ) an outburst time of 39 d for  $\Delta T_{\text{eff}} = -3500$  K. This time-scale corresponds to the brightness declines by 3–6 mag. observed in R CrB-type variables, which occur in less than 50 d (Clayton 1996). In these smaller stars the outbursts occur faster and more violently than in the hypergiants. The burst-time also depends on the relative abundances

of hydrogen and helium, whereas equation (15) assumes a pure hydrogen (or helium) atmosphere. For gas mixtures, the last factor of equation (15) requires the multi-component expressions of  $1/(\Gamma_3-1)$ , computed in Lobel et al. (1992) for solar abundance values (Anders & Grevesse 1989). In the first ionization zone of helium with  $T_0=13,000$  K, we compute that  $1/(\Gamma_3 - 1)=6.67$ , which yields for  $\rho$  Cas  $t_{\text{burst}}=72$  d. This time-scale is at least a factor of two shorter than the observed burst-time, which excludes driving by helium recombination in this luminous hypergiant. Note that for  $\rho$  Cas we compute that the outburst extends the atmosphere with  $v=36$  km s<sup>-1</sup> over  $\Delta R_*=v \times t_{\text{burst}}=988 R_\odot$  ( $\simeq 2.5 R_*$ ), while for R CrB the equation predicts that  $v=48$  km s<sup>-1</sup> and  $\Delta R_*=235 R_\odot$  ( $\simeq 2.9 R_*$ ).

## 12. Discussion

In a study of stellar outburst mechanisms, Sedov (1958) obtained time-dependent solutions for the propagation of a spherically expanding shock wave in a gravity field. Analytic solutions are provided in which the energy of the shock motion remains equal at any time to the initial energy in the equilibrium state of the unperturbed atmosphere. He derived a simple analytic solution in cases of a constant specific heat ratio  $\gamma=c_v/c_p=7/6$ , and showed that the radial velocity of the shock decreases monotonically with  $v_{\text{sh}}=\text{const} \times t^{-1/6}$ . The equations can also be applied to the extended partial hydrogen ionization zone in the upper atmosphere of  $\rho$  Cas with  $\gamma < 4/3$  before the outburst. This zone provides mechanical shock energy by hydrogen recombination to drive the outburst, with the conservation of total energy.

Since the adiabatic expansion velocities computed for the outburst (and observed also) of  $\rho$  Cas exceed the adiabatic sound speed ( $v_s=\sqrt{\Gamma_1 P/\rho}=5-13$  km s<sup>-1</sup>), we propose the formation of a circumstellar shock wave that surpasses the gravitational pull of the supergiant, carrying momentum beyond the sonic point into the circumstellar environment. The disrupted and inflated atmosphere reaches a state of reduced total energy, and adapts to this energy dissipation by contracting globally. Hydrogen recombination driving thus provides a limit to the mechanical energy which can be released by this thermal outburst mechanism, and may explain why comparable atmospheric changes have occurred during the three outbursts of  $\rho$  Cas in the last century; for example, the formation of TiO in outer layers with  $T < 4000$  K, and the decrease of  $V$ -brightness by  $\leq 1^{\text{m}}.5$ , for total outburst times of 500 to 660 d.

We think that the outburst results from a synchronization phenomenon whereby ionization-recombination energy is released upon decompression, in a global cooling of the entire atmosphere. The increase of outflow momentum causes an outward acceleration by which the

atmosphere further cools, thereby reinforcing the release of more ionization energy. The cooling and recombination rates synchronize, which causes a fast escalation of ionization energy release into atmospheric expansion toward the deeper layers that contain more ionization energy. This unleashes even more energy, and hence produces an explosive runaway event.

The condition for an outburst is therefore strongly dependent of the overall temperature- and density-structure during the atmospheric compression phase that leads up to the eruption. The atmospheric dimensions determine whether the recombination rate (and hence the wind acceleration) can keep up with the cooling rate, and this in turn determines whether a ‘disruption’ front, or a strong expansion shock wave, can move down the atmosphere, and consume most of its ionization energy. The full time-dependent solution of the hydrodynamic and thermodynamic equations will therefore also require the proper treatment of the detailed physics of strong shock waves in partially ionizing gas, with variable gammas across the shock surface. It is known that the ionization of hydrogen due to the compression by strong shock waves can store 5 to 6 times more energy in ionization energy than the amount that is available in the translational motion of particles of the shocked gas (Lobel 1997, p. 80). Note that partial thermal ionization can raise the compressibility of the shocked gas, whereby the density jump ratio across a compression front can increase to very high values of  $\sim 20$ . However, the density jump ratio is limited to a maximum value of only 4 in cases of ideal gas, for which partial ionization is neglected.

The ionization-recombination instability requires a ‘trigger’ that provides the precise atmospheric structure to this cascade of energy release. The outburst of  $\rho$  Cas is preceded by a conspicuously long period between 1993 and 1997 over which the stellar wind practically vanishes. The wind acceleration appears to stall (observed from the disappearance of violet extended wings in the photospheric lines), while the (photospheric) radial velocity increases by  $30 \text{ km s}^{-1}$  (Fig. 1). The  $V_{\text{rad}}$ -curve, shows four quasi-periodic oscillations, with  $T_{\text{eff}}$ -changes of 500 to 800 K during the pulsation cycles. After that time the atmosphere expands rapidly, with the strong  $V$ -brightness decrease of the pre-outburst cycle. It signals the sudden release of flow momentum that has accumulated in the atmosphere over the four preceding years, for example in a denser mass shell that has been swept up in the atmosphere by a subsonic wind.

During the large oscillation preceding the actual outburst, the atmosphere decompresses and cools, thereby changing its thermodynamic structure, so that the next phase of compression can effectively convert the kinetic energy from a ballistic supersonic downfall (by  $\sim 13 \text{ km s}^{-1}$ ) into ionization energy. The atmosphere therefore strongly collapses, becoming denser and warmer, while partly storing this kinetic energy into ionization energy. What follows is a phase of unusual high  $T_{\text{eff}} \sim 8000 \text{ K}$ . Cool supergiant atmospheres become very

compressible (or expandable) around  $T_{\text{eff}}=7000\text{--}8000$  K by the decrease of  $\Gamma_1$ , which is related to the atmospheric elasticity (or bulk modulus), to below the stability value of  $4/3$  over a large geometric fraction. Lobel (2001) shows (see Fig. 6) that these atmospheres can even assume  $\Gamma_1$ -values below unity for  $\log \tau_{\text{R}} \leq 0$ , due to partial LTE- and non-LTE-ionization of hydrogen. For these atmospheric conditions the volume-averaged  $\langle \Gamma_1 \rangle$  assumes values below  $4/3$  down to the base of the atmosphere, beyond the hydrogen and helium ionization zones. Local mechanic perturbations, i.e. gas rarefactions, then become not sufficiently balanced by the counterworking thermodynamic forces. The latter rather enhance the rarefactions and release more recombination energy, which causes their displacements  $\delta r/r$  from hydrostatic equilibrium to grow exponentially with time.

For the conditions of supergiant atmospheres with  $T_{\text{eff}}=7000\text{--}8000$  K, the atmospheric structure is very dynamically unstable, and tuned so that a self-sustained hydrodynamic-thermal avalanche can occur. The entire atmosphere rapidly de-ionizes and expands from the top to the very bottom, while driving an accelerating wind. This mechanism is time-critical and comes to a halt only when most of the atmospheric ionization energy has been released by the outburst, and  $\langle \Gamma_1 \rangle$  returns to above  $4/3$  in the outer atmosphere. The atmosphere cools down to below  $T_{\text{eff}}=4500$  K with the fast expansion, whereby the upper layers with  $T_{\text{kin}} < 4000$  K form TiO bands that characterize the spectra of M-type stars.

The outburst trigger can be compared to lifting a heavy hammer over a long period of time, that suddenly drops and hits a lighter rubber ball on the floor. The ball jumps up very high because its elasticity conserves linear momentum. For the outburst of  $\rho$  Cas, thermal ionization-recombination ensures that the high compressibility of the atmosphere ‘bounces back’ in a resonant amplification of a superwind that further cools and releases more energy from the decompressing ionization reservoir. Think of it as if the ball bounced hard enough to also release internal chemical energy, giving it an additional kick (e.g. jump higher on a trampoline by timely bending and stretching your legs). In a study of gravitational collapse of stellar cores, which can eject the stellar envelope in a supernova-like explosion, Bruenn, Arnett, & Schramm (1977) compute that the kinetic energy for a reflected shock wave is maximized when a large inward acceleration is rapidly changed to large outward acceleration during the bounce. They suggest that this is accomplished with an adiabatic index below  $4/3$ , that goes suddenly well above  $4/3$ . Arnett & Livne (1994) calculate that when the first adiabatic index is only slightly above  $4/3$ , the released (here thermo-nuclear) energy will drive a pulsation with large amplitude.

The conversion of ionization-recombination energy into expansion energy may also explain why the outbursts of  $\rho$  Cas are rather sporadic. The progressive built-up of momentum in the atmosphere by a stalled wind over a long period of time, which can trigger the coher-



ent gravitational collapse, is frequently disrupted by the usual quasi-periodic oscillations of the atmosphere. Ordered atmospheric oscillations effectively transport momentum upward which inhibits activation of the trigger, and does not allow sufficient momentum to built up (e.g.  $T_{\text{eff}}$  above 7250 K has previously not been reported for  $\rho$  Cas). This occurs most of the time, but occasionally the quiescent pulsations become very disordered (or incoherent) due to the weak force of gravity and the enormous atmospheric extension (Lobel et al. 1994; e.g. Soker & Harpaz 1992 examine the location of the ‘transition region’ relative to the ionization zones which determines if non-radial pulsation modes are excited in AGB stars). Because these random modes cease to effectively convey pulsation momentum upward, the stellar wind driving vanishes, and the piston momentum becomes temporarily stored in the atmosphere. If momentum can accumulate over a period of more than four pulsation cycles (four years say), a subsequent average radial pulsation is preceded by very high atmospheric compression, which produces the required thermal conditions of  $\langle \Gamma_1 \rangle < 4/3$ , that yield the ionization-recombination driven runaway. The outburst occurs when the atmospheric cooling rate synchronizes with the displacement of the driving recombination front toward the deeper atmosphere. In these low-gravity atmospheres the recombination acceleration is almost independent of  $g_*$  (e.g. Figure 1 is computed for  $g_*=0$ ). The latter of course determines the magnitude of the expansion velocity during the outburst, and whether the effective atmospheric acceleration  $g_{\text{eff}}$  becomes negative (Nieuwenhuijzen & de Jager 1995). An inward directed  $g_{\text{eff}}$  over a long period of time plays a crucial role for the initial built-up of momentum, and a subsequent activation of the trigger. Outbursts that are initiated by a similar trigger mechanism are therefore expected in other pulsating stars that assume comparable thermal conditions at the base of the atmosphere as  $\rho$  Cas.

It is interesting to note that the time-scale over which the total ionization-recombination energy, released into the circumstellar environment by the outburst (assuming complete hydrogen recombination), is dissipated by the stellar radiation field over a period following the fast envelope expansion of

$$t_{\text{brightness-min}} \simeq \frac{I_{\text{H}} N \rho_{\text{s}} d_{\text{s}}}{\sigma T_{\text{eff}}^4}, \quad (16)$$

where  $\sigma$  is the Stefan-Boltzmann constant. For an atmospheric expansion of  $d_{\text{s}} = 869 R_{\odot}$  during outburst, and an envelope density of  $\rho_{\text{s}} = 10^{-10} \text{ gr cm}^{-3}$  (determined from TiO bands in § 8.2), we compute with equation (16) that  $t_{\text{brightness-min}} \simeq 86 \text{ d}$  for  $T_{\text{eff}}=3500 \text{ K}$ . This time corresponds very well to the period over which the deep brightness minimum of  $\sim 100 \text{ d}$  was observed in late 2000.

### 13. Summary and Conclusions

1. Spectroscopic monitoring of the yellow hypergiant  $\rho$  Cas with high-resolution over the past 8.5 years reveals a strong correlation between the radial velocity curve and the  $V$ -magnitude variations. The latter lag the photospheric oscillations by  $\sim 100$  d. Between 1994 and 1997 the entire upper and lower atmosphere collapses, resulting in the pre-outburst cycle of 1999, when a very large brightness maximum of  $V \sim 4^m.0$  is assumed. During the  $V$ -maximum, the photosphere expands unusually fast, and  $V$  subsequently dims by  $1^m.2 - 1^m.4$  to the very deep outburst minimum during  $\sim 100$  d in late 2000. The profile shape and velocity variations observed in selected optical Fe I lines, formed in the stellar photosphere, occur on markedly shorter time-scales of  $\sim 300$  d than the changes of  $H\alpha$ . It signals a strongly velocity-stratified pulsating atmosphere.

2. The outburst is preceded by a variability phase whereby enhanced absorption develops in the long-wavelength wing of  $H\alpha$ , together with a conspicuously strong short-wavelength emission. During the outburst the  $H\alpha$  absorption core becomes very weak and develops satellite emission lines. It indicates that the line is filled in by emission due to recombination of hydrogen with the global cooling of the atmosphere by  $\sim 3000$  K. The equivalent width variations of the Fe I  $\lambda 5572$  line reveal that the  $T_{\text{eff}}$ -changes are limited to  $\sim 500 - 800$  K during the quiescent pulsation phases. Spectral synthesis calculations reveal however that  $T_{\text{eff}}$  decreases from  $\geq 7250$  K to  $\leq 4250$  K during the outburst.

3. During the outburst the optical absorption spectrum strongly blue-shifts, and resembles the spectra of the early M-type supergiants Betelgeuse and  $\mu$  Cep. Central emission appears above the continuum level in the split Na  $D$  lines with the decrease of the optical continuum flux. The hypergiant is surrounded by a tenuous gas envelope producing permanent line emission in these broad resonance lines, and in forbidden optical [Ca II] lines. Prominent permitted emission lines of neutral metals appear above the local continuum level during exceptional pulsation phases when  $T_{\text{eff}}$  is large, and the photosphere rapidly begins to expand. It indicates that the peculiar emission lines are excited by the supersonic stellar wind. On the other hand, high-resolution observations do not reveal central emission in the broad Ca II H & K lines, indicating the absence of a (classic) permanent chromosphere in the hypergiant.

4. Most remarkably, weak electronic TiO bands develop in the summer of 2000 before the  $V$ -brightness minimum. Detailed spectral synthesis calculations show that the bands form over atmospheric regions with  $3000 \text{ K} \leq T \leq 4000 \text{ K}$  and  $-9.8 \leq \log \rho \leq -8.5$ , and assume an expansion velocity of  $35 \text{ km s}^{-1}$ . These molecular bands develop within  $\sim 100$  d after fast outward acceleration, due to the rapid decline of the kinetic temperature in the line formation region. During the outburst, the TiO envelope expands faster than the photosphere, with

the photospheric expansion determined from the radial velocity of the atomic absorption line spectrum.

5. We compute an exceptionally large mass-loss rate of  $\dot{M}=5.4\times 10^{-2} M_{\odot} \text{ yr}^{-1}$  for spherical expansion of the TiO envelope with a minimum density of  $\rho_{\text{min}}=10^{-10} \text{ gr cm}^{-3}$  at  $R_{*}=400 R_{\odot}$ . The cool gas shell expands to  $\sim 2.5 R_{*}$  during an outburst period of  $\sim 200$  d. The large mass-loss rate indicates that the recurrent outbursts of  $\rho$  Cas, about every half a century, are the main mass-loss mechanism of this cool star in the post-red supergiant evolutionary phase.

6. Within half a year after the deep brightness minimum  $T_{\text{eff}}$  increases to  $\simeq 5750$  K, and the peculiar TiO bands vanish. Optical and near-IR TiO bands were also observed during the previous outbursts of  $\rho$  Cas in 1986 and 1946, when the star dimmed and brightened up over comparable time-scales. TiO is also observed before the deep brightness minimum of 1946, indicating that the TiO formation is dependent on the atmospheric expansion velocity, which is largest before the deep minimum. Strong emission in the short-wavelength wing of H $\alpha$  is also observed before the outburst of 1986, indicating that the wind dynamics in the outer atmospheric envelope plays a crucial role for an activation of the trigger that causes the outbursts of  $\rho$  Cas.

7. We compute that the outburst mechanism can be driven by the release of ionization energy due to the recombination of hydrogen as the atmosphere cools. When  $T_{\text{eff}}$  increases to  $\geq 7250$  K, the supergiant atmosphere becomes dynamically unstable because the first generalized adiabatic index  $\Gamma_1$  decreases to below  $4/3$  in the partial ionization zone of hydrogen. Atmospheric expansion in this region becomes further amplified with the adiabatic cooling and the release of more driving energy by hydrogen recombination, until  $T_{\text{eff}} \leq 3750$  K and  $\Gamma_1$  increases above  $4/3$ . The activation of the trigger therefore requires a phase of exceptionally high  $T_{\text{eff}}$  before the outburst, which can result from enhanced global atmospheric compression during a cycle of strong coherent pulsation in the pre-outburst cycle of 1999. Based on these simple considerations we derive an equation that correctly predicts the time-scale for the rapid brightness decrease in terms of observable stellar parameters  $R_{*}$ ,  $T_{\text{eff}}$ , the change of  $T_{\text{eff}}$ , and the ionization energy of the recombining element under consideration.

This research was supported in part through grant number GO-5409.02-93A to the Smithsonian Astrophysical Observatory from the Space Telescope Science Institute, which is operated by the AURA, under NASA contract NAS 5-26555. A. L. would like to thank S. Bagnulo at European Southern Observatory (Chile), and A. E. Rosenbush at the Crimean Astrophysical Observatory (Ukraine) for providing optical spectra of  $\rho$  Cas. We thank R. Kurucz at the Smithsonian Astrophysical Observatory for discussions and help with the

spectral synthesis calculations. A. L. gratefully acknowledges support by the SRON-Utrecht (The Netherlands) over the years for maintaining the spectral data base of  $\rho$  Cas. We thank numerous observers of the WHT-UES service programs who have contributed to this long-term project.

## REFERENCES

- Anders, E., & Grevesse, N. 1989, *Geochim. Cosmochim. Acta*, 53, 197
- Arnett, D., & Livne, E. 1994, *ApJ*, 427, 315
- Beardsley, W. R. 1953, *ApJS*, 5, 381
- Beardsley, W. R. 1961, *AJ*, 58, 34
- Bidelmann, W. P., & McKellar, A. 1957, *PASP*, 69, 31
- Boyarchuk, A. A., Boyarchuk, M. E., & Petrov P. P. 1988, *Proc. of the sixth Soviet-Finnish Astronomical Meeting held in Tallinn, Nov. 10-15, 1986*, U. Hanni & I. Tuominen (eds.), *Tartu Astrophysical Obs. Teated*, 92, 40
- Bruenn, S. W., Arnett, W. D., & Schramm, D. N. 1977, *ApJ*, 213, 213
- Clayton, G. C 1996, *PASP*, 108, 225
- Davidson, K., & Humphreys, R. M. 1997, *ARA&A*, 35, 1
- de Jager, C. 1998, *A&ARev.*, 8, 145
- de Jager, C., Lobel, A., & Israelian, G. 1997, *A&A*, 325, 714
- de Jager, C., Lobel, A., Nieuwenhuijzen, H., & Stothers, R. 2001, *MNRAS*, 327, 452
- de Jager, C., & Nieuwenhuijzen, H. 1997, *MNRAS*, 290, L50
- Dupree, A. K., Hartmann, L., & Avrett, E. H. 1984, *ApJ*, 281, L37
- El Eid, M., & Champagne, A. E. 1995, *ApJ*, 451, 298
- Fill, E., Pretzler, G., Tommasini, R., & Witzel, B. 2000, *Europhys. Lett.*, 49 (1), 27
- Galazutdinov, H. A. 1992, *Preprint of the Special Astrophysical Observatory of the Russian Academy of Science No. 92*

- Gaposchkin, S. 1949, Harvard Bulletin 919, 18
- Gaposchkin, C. P., Gaposchkin, S., & Mayall, M. 1947, AJ, 52, 123
- Greenstein, J. L. 1948, ApJ, 108, 78
- Harpaz, A. 1998, ApJ, 498, 293
- Hassforther, B. 2001, BAV Rundbrief, 50, 34
- Humphreys, R. M., & Davidson, K. 1994, PASP, 106, 1025
- Humphreys, R. M., Smith, N., Davidson, K., Jones, T. J., Gehrz, R. T., Mason, C. G., Hayward, T. L., Houck, J. R., & Krautter, J. 1997, AJ, 114, 2778
- Ilyin, I. 2000, PhD Thesis, Univ. of Oulu, Finland
- Israelian, G., Lobel, A., & Schmidt M. R. 1999, ApJ, 523, L145
- Jiang, S. Y., & Huang, R. Q. 1997, A&A, 317, 121
- Jura, M., & Kleinmann, S. G. 1990, ApJ, 351, 583
- Keenan, P. C. 1947, ApJ, 106, 295
- Kurtz, M. J., & Mink, D. J. 1998, PASP, 110, 934
- Kurucz, R. L. 1996, in Model Atmospheres and Spectrum Synthesis, ed. S. Adelman, F. Kupka and W. Weiss (ASP Conf. Ser., 108), 160
- Kurucz, R. L. 1999, Kurucz CD-ROM No. 24. Cambridge, Mass., Smithsonian Astrophysical Observatory, 199
- Latham, D. W. 1992, in IAU Coll. 135, Complementary Approaches to Double and Multiple Star Research, eds. H. A. McAlister & W. I. Hartkopf (San Francisco: ASP), 110
- Leiker, P.S., & Hoff, D. B. 1987, Information Bulletin on Variable Stars, 3020, 1
- Leiker, P. S., Hoff, D. B., & Milton, R. 1989, Information Bulletin on Variable Stars, 3345, 1
- Leiker, P. S., Hoff, D. B., Nesbella, J., Gainer, M., Milton, R., & Pray, D. 1988, Information Bulletin on Variable Stars, 3172, 1
- Lobel, A. 1997, Pulsation and Atmospheric Instability of Luminous F and G-type Stars, PhD. thesis, Brussels Univ., ISBN 90-423-0014-0, Shaker Publ., Maastricht

- Lobel, A. 2001a, ApJ, 558, 780
- Lobel, A. 2001b, <http://lanl.arXiv.org/abs/astro-ph/0108358>
- Lobel, A., Achmad, L., de Jager, C., & Nieuwenhuijzen, H. 1992, A&A, 246, 147
- Lobel, A., de Jager, C., Nieuwenhuijzen, H., Smolinski, J., & Gesicki, K. 1994, 291, 226
- Lobel, A., & Dupree, A. K. 2000a, BAAS 197, #44.15
- Lobel, A., & Dupree, A. K. 2000b, ApJ, 545, 454
- Lobel, A., & Dupree, A. K. 2001, ApJ, 558, 815
- Lobel, A., Israelian, G., de Jager, C., Musaev, F., Parker, J. Wm., & Mavrogiorgou, A. 1998, A&A, 330, 659
- Lucy, L. B. 1967, AJ, 72, 813
- Massey, P. 2000, PASP, 112, 144
- Meynet, G., Maeder, A., Schaller, G., Schaerer, D., & Charbonnel, C. 1994, A&AS, 103, 97
- Mihalas, D., & Weibel Mihalas, B. 1984, Foundations of Radiation Hydrodynamics, Oxford Univ. Press, Oxford
- Moore, C. E. 1945, Princeton Obs. Contr. No. 20.
- Morrison, N. D., Knauth, C. D., Mulliss, C. L., & Lee, W. 1997, PASP, 109, 676
- Nieuwenhuijzen, H., & de Jager, C. 1995, A&A, 302, 811
- Nordström, B., Latham, D. W., Morse, J. A., Milone, A. A. E., Kurucz, R. L., Andersen, J., & Stefanik, R. P. 1994, A&A, 287, 338
- Paczynski, B., Ziolkowski, J. 1968, Proc. IAU Symposium No. 34, D. E. Osterbrock and C. R. O'Dell (eds.), Dordrecht, D. Reidel Publ., 396
- Payne-Gaposchkin, C., & Mayall, M. W. 1949, Harvard Bulletin 918, 11
- Percy, J. R., Kolin, D. L. 2000, JAVSO, 28, 1
- Percy, J. R., Kolin, D. L., & Henry, G. W. 2000, PASP, 112, 363
- Popper, D. M. 1947, AJ, 52, 129

- Schuster, M. T., & Humphreys, R. M. 2001, BAAS 199, #92.17
- Schwenke, D. W. 1998, Faraday Discuss., 109, 321
- Sedov, L. I. 1958, Proc. IAU Symposium No. 8, J. M. Burgers and R. N. Thomas (eds.), 1077
- Smith, N., Humphreys, R. M., Davidson, K., Gehrz, R. D., Schuster, M. T., & Krautter, J. 2001, AJ, 121, 1111
- Soker, N., & Harpaz, A. 1992, PASP, 104, 923
- Stothers, R. B., & Chin, C.-W. 1997, ApJ, 489, 319
- Stothers, R. B., & Chin, C.-W. 2001, ApJ, 560, 934
- Tai, W. S., & Thackeray, A. D. 1948, MNRAS, 108, 271
- Takeda, Y., & Takeda-Hidai, M. 1994, PASJ, 46, 395
- Thévenin, F., Parthasarathy, M., & Jasiewicz, G. 2000, A&A, 359, 138
- Thackeray, A. D. 1948, MNRAS, 108, 279
- Tuchman, Y. 1983, in Planetary nebulae, Proc. of the Symposium, London, England, Aug. 9-13, 1982, Dordrecht, D. Reidel Publ. Co., 281
- Tuchman, Y., Sack, N., & Barkat, Z. 1978, ApJ, 219, 183
- van Genderen, A. M. 2001, A&A, 366, 508
- Wagenhuber, J., & Weiss, A. 1994, A&A, 290, 807
- Zsoldos, E., & Percy, J. R. 1991, A&A, 246, 441

Fig. 1.— The  $V$ -brightness curve of  $\rho$  Cas (*solid symbols*) is compared in the upper panel to the radial velocity curve (*dotted line*), observed over the past 8.5 years. Observation dates of echelle spectra are marked with vertical lines in the lower panel. The radial velocity curve (*connected solid dots*) of Fe I  $\lambda 5572$  shows a strong increase of the photospheric pulsation amplitude before the outburst of fall 2000 (JD 2451800–JD 2451900), when TiO bands develop (*marked TiO*). The peculiar emission line spectrum of  $\rho$  Cas is observed during phases with fast atmospheric expansion (*and is marked by Em.*). The vertical dashed lines, labeled a to e, are compared and modeled in this paper. Note that the dotted line connecting the radial velocity values is determined from the half width of the Fe I line at half absorption minimum by linearly interpolating between the profile shapes.



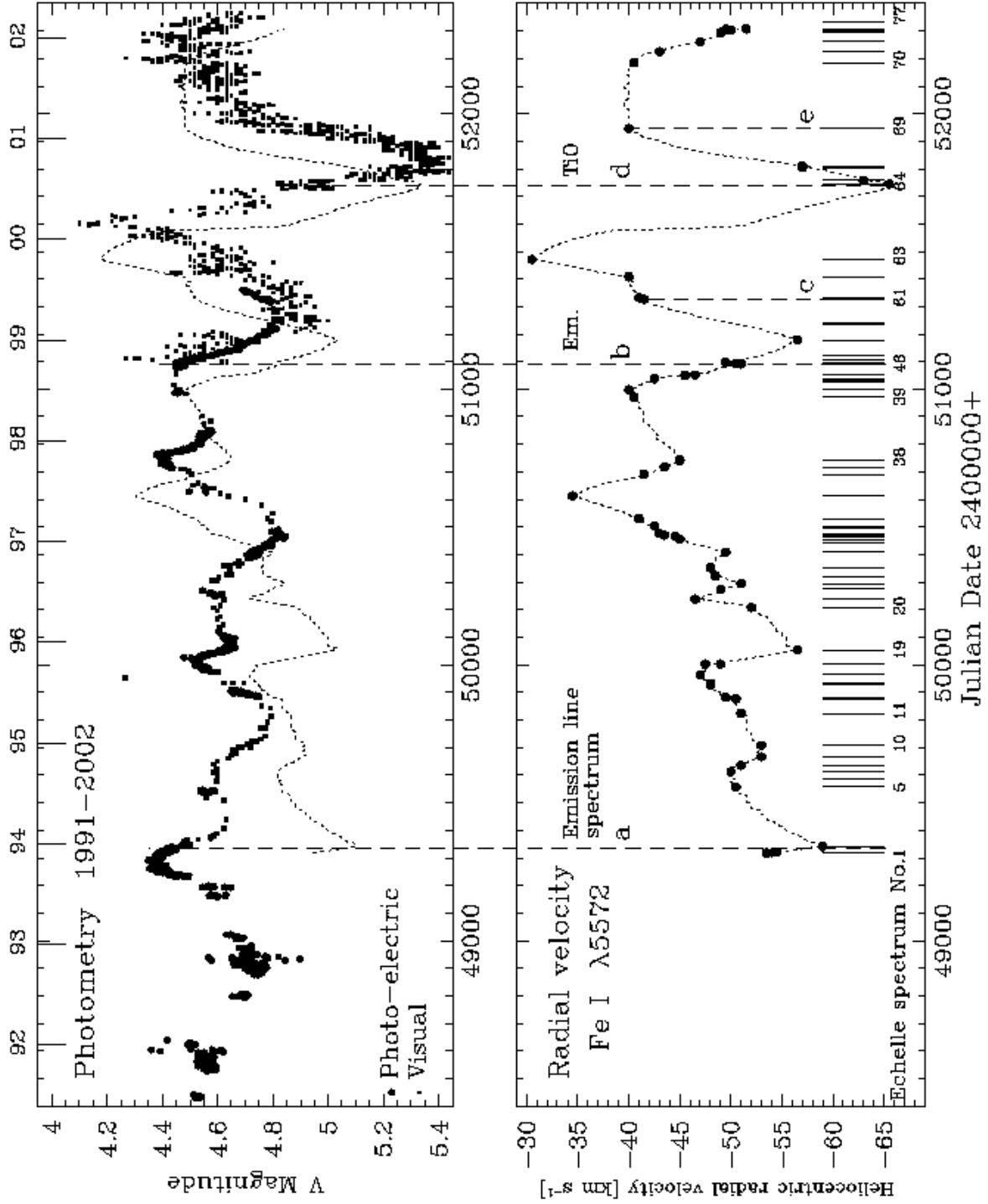


Fig. 2.— Detailed evolution of the line profiles of  $H\alpha$ , Fe I  $\lambda 5572$ , and Fe I  $\lambda 5506$  (*panels left to right*), observed between 1993 November and 2002 July. The right-hand tickmarks (*bottom to top*) indicate the continuum level. The vertical dotted lines mark the stellar rest velocity of  $\rho$  Cas. The  $H\alpha$  line shows variable emission wings, with a central absorption core that becomes very weak during the outburst. The Fe I lines show Doppler shifts, and variable extended violet line wings during the photospheric pulsations and the outburst. The Fe I  $\lambda 5506$  is split due to a static central emission core (see text).

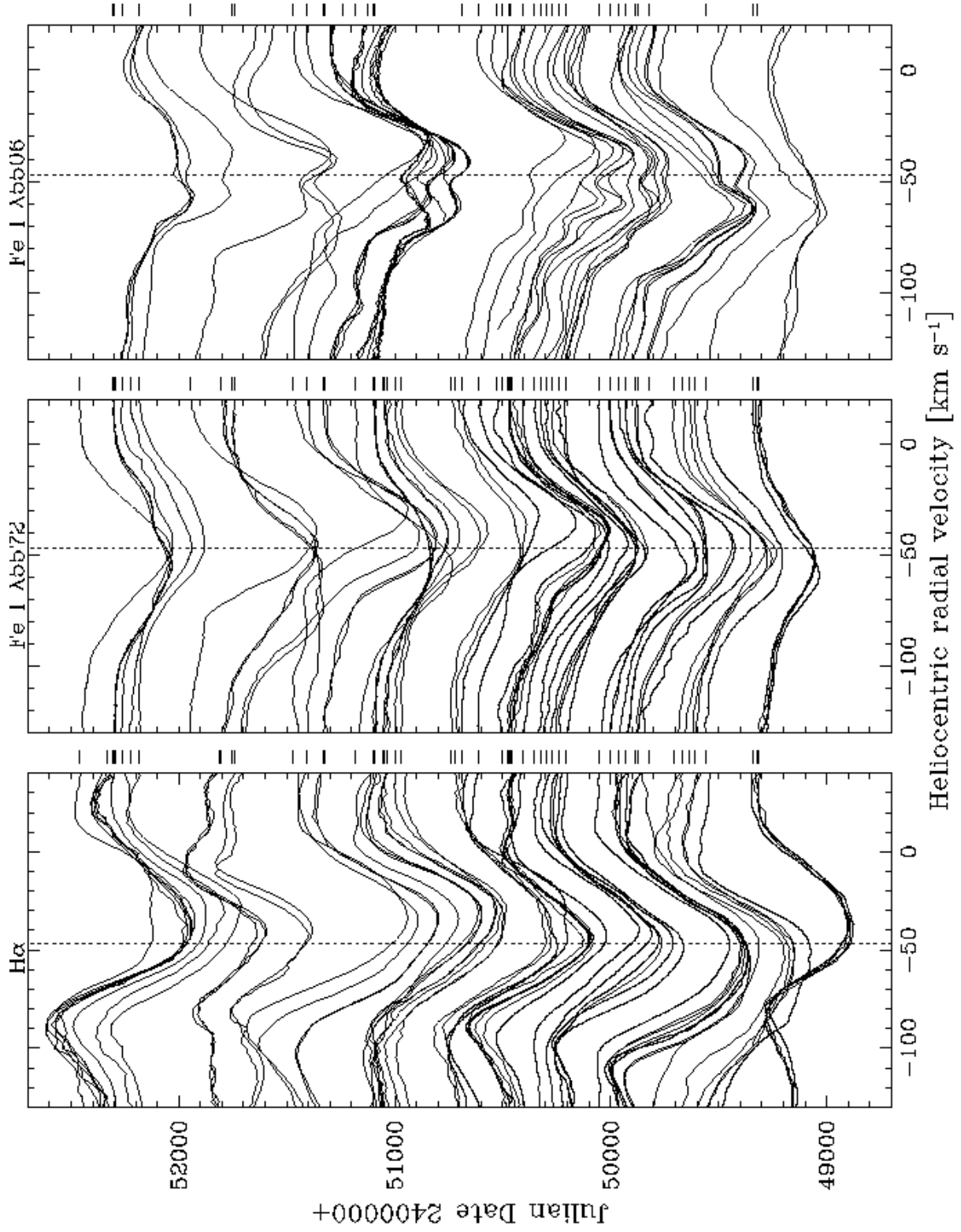


Fig. 3.— Dynamic spectra of the three lines of Figure 2. The grayscale is linear (online figure: red color indicates the local continuum level, and blue the depression in the line cores). The white spots in  $H\alpha$  are emission above the continuum level. The line profiles are linearly interpolated between subsequent observation nights, marked with the left-hand tickmarks. Time runs upward, indicated for each new calendar year with the right-hand numbers. The dashed white lines trace the radial velocity curve, determined from the bisector at half intensity minimum of the absorption portion of the line profile. The curves reveal a strongly velocity-stratified dynamic atmosphere. Notice the strong blue-shift of the Fe I lines during the outburst (mid 2000). The outburst is preceded by very strong emission in the short-wavelength wing of  $H\alpha$ , while the absorption core extends longward, and the photospheric Fe I lines strongly red-shift. A strong collapse of the entire atmosphere precedes the outburst (see text).

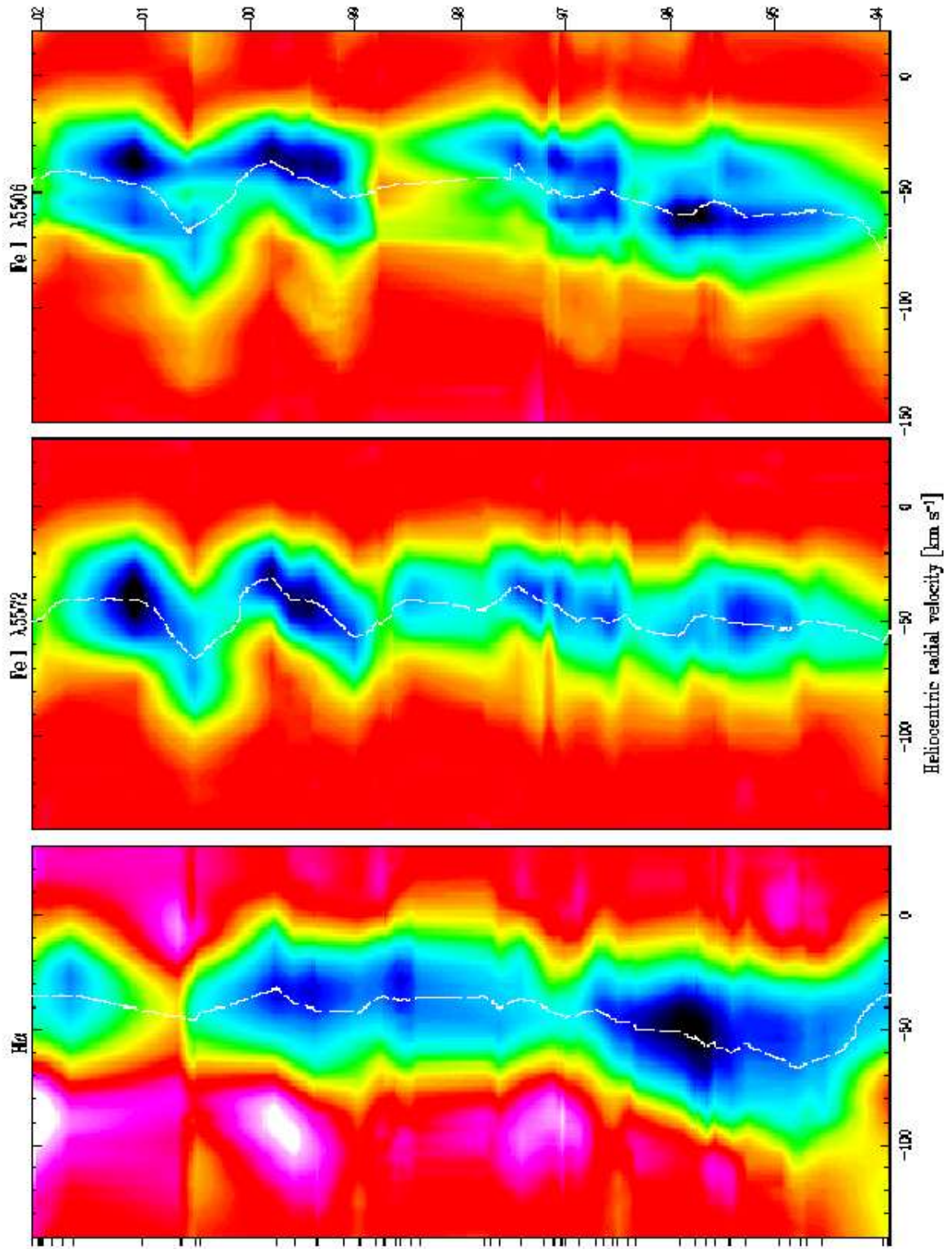


Fig. 4.— Comparison of the radial velocity curve measured from Fe I  $\lambda 5572$  (*dots*), and from cross-correlating the spectrum observed between 5166 Å and 5211 Å (*boxes*). The photospheric expansion decelerates over a long period of time between JD 2449300 and JD 2450400. After this time, the photosphere and the H $\alpha$ -envelope collapse until JD 2450600. The global contraction phase is followed by the pre-outburst cycle in 1999 during which the photosphere rapidly expands and contracts, resulting in the very large  $V$ -brightness maximum of JD 2451600. The maximum is preceded with the outburst and a subsequent  $V$ -magnitude decrease by  $1^m.2$ – $1^m.4$  during  $\sim 200$  d. Both radial velocity measurement techniques are in good agreement during the strong velocity excursions. The open circles are velocity variations determined from the second moment of the Fe I  $\lambda 5572$  line (see text).

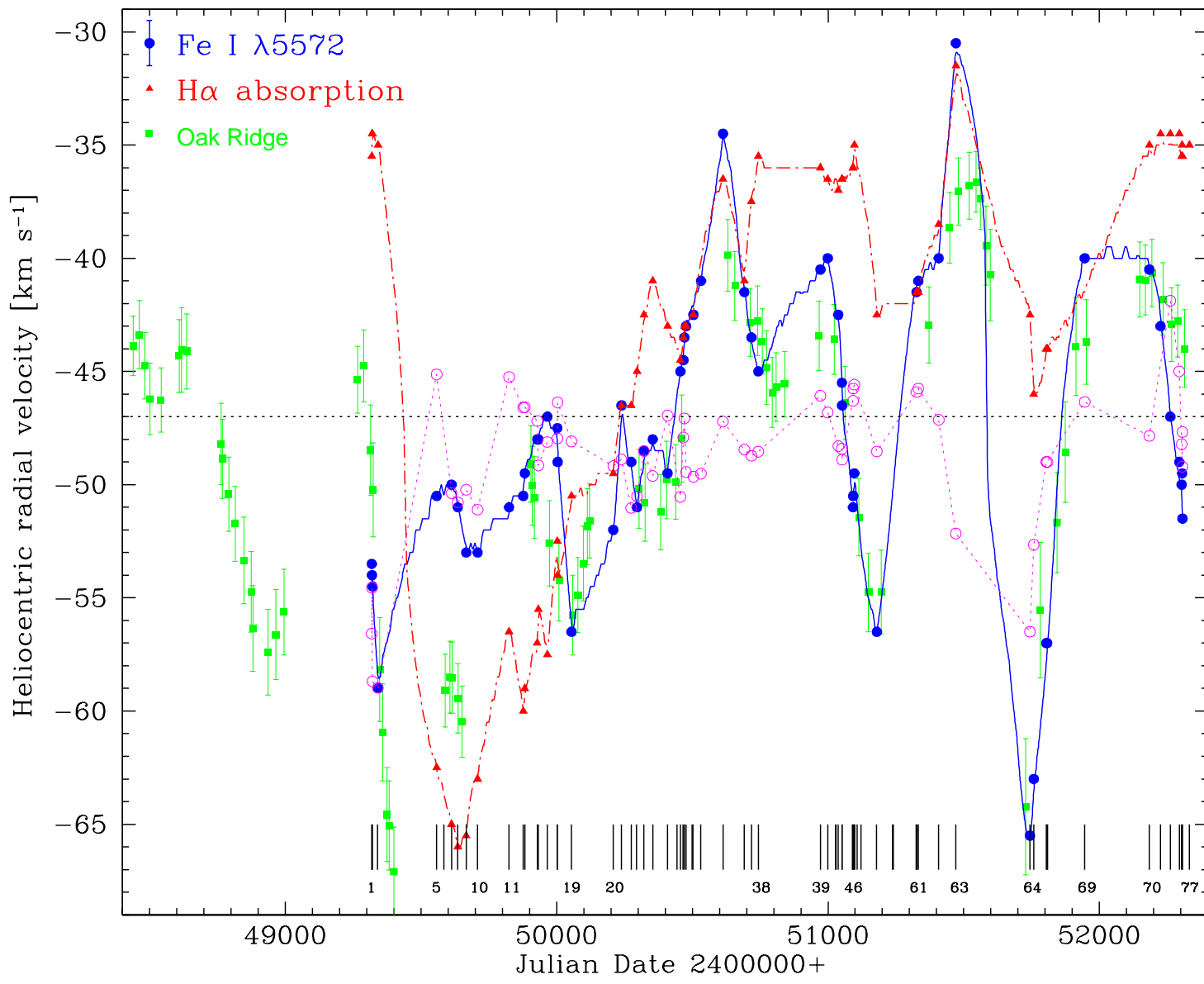


Fig. 5.— A comparison of the  $V$ -brightness curve with equivalent width values measured from Fe I  $\lambda 5572$  (*circles*), Fe II  $\lambda 5325$  (*triangles*), and H $\alpha$  absorption and emission (*crosses*) reveals a strong correlation of the Fe I equivalent width with  $V$ . It signals temperature changes in the line formation region, determined by variations of  $T_{\text{eff}}$  with the photospheric pulsations. The Fe II line is anti-correlated due to changes of the iron ionization balance. H $\alpha$  is uncorrelated with a longer variability period, indicating a mean line formation region different from the photospheric iron lines. The lower panel shows the changes of  $T_{\text{eff}}$  with pulsation, computed from the equivalent width values of Fe I (*circles*), and from the  $V$ -magnitude values (*boxes*). A decrease of  $T_{\text{eff}}$  by  $\sim 3000$  K occurs during the outburst.



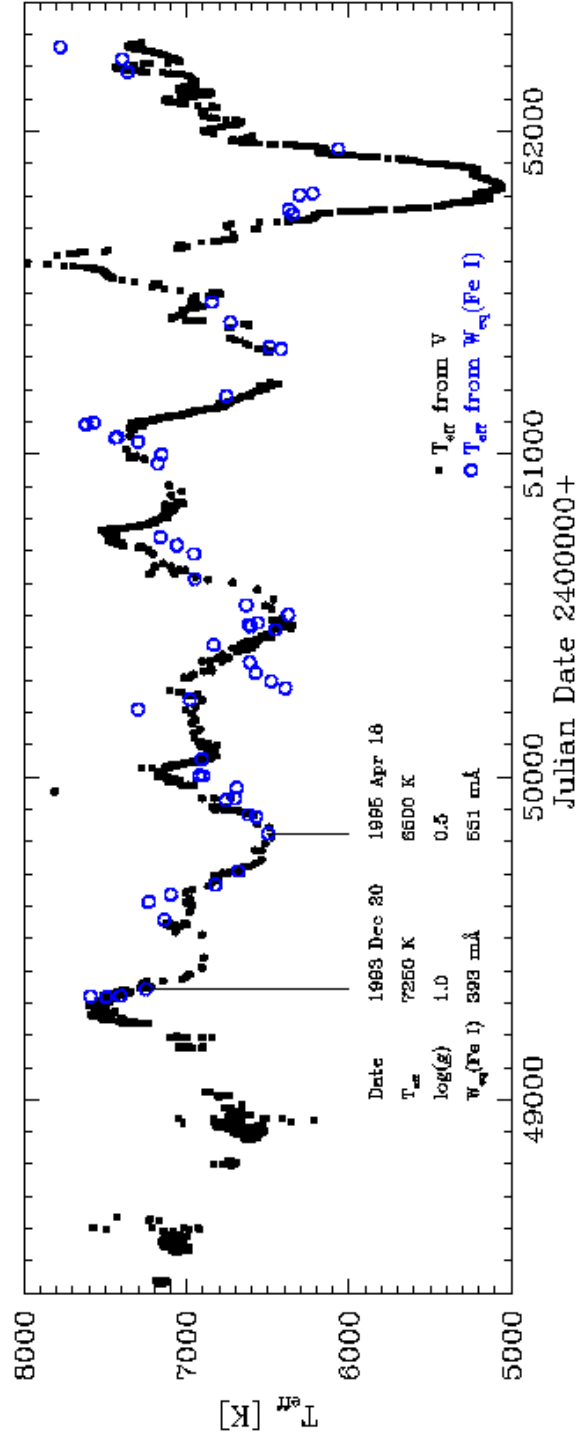
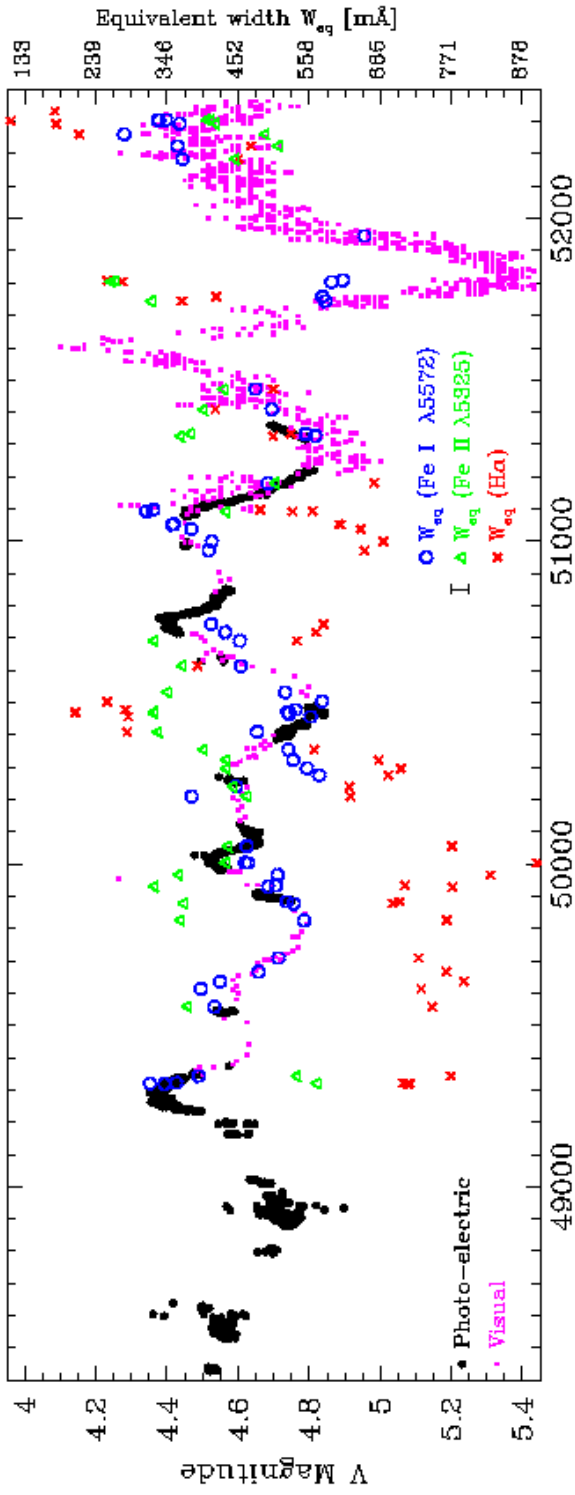


Fig. 6.— High-resolution spectra of  $\rho$  Cas around Fe I  $\lambda 6358$  (*solid lines labeled a to e for the dates of Fig. 1*) show that the photospheric spectrum strongly blue-shifts during the outburst. Synthetic spectrum calculations (*dotted lines*) indicate that  $T_{\text{eff}}$  decreases to  $\simeq 4250$  K, and the spectrum becomes comparable to the early M-type supergiants  $\mu$  Cep (*lower solid line*) and Betelgeuse (*dashed line*), with  $T_{\text{eff}}=3500$  K. A prominent emission line spectrum is observed in  $\rho$  Cas during phases of high  $T_{\text{eff}}=7250$  K, when the atmosphere rapidly accelerates outward. Note that the Fe I emission line blends with an absorption line of V I. Other neutral absorption lines are also indicated. The vertical dotted line is drawn at the stellar rest velocity.



Fig. 7.— High-resolution spectra of  $\rho$  Cas reveal that the  $H\alpha$  absorption core becomes very weak during the outburst (*solid line labeled d*). The line core does not blue-shift, and develops strong emission line wings. The line becomes filled in by recombination emission with the cooling of the  $H\alpha$ -envelope during outburst. Strong emission is also observed in the blue wing of  $H\alpha$  (*long-short dashed line*) for the pre-outburst cycle (*c*), during the atmospheric collapse that precedes the large  $V$ -brightness maximum before the outburst. The  $H\alpha$  line core of  $\rho$  Cas is much weaker than in Betelgeuse and  $\mu$  Cep (*solid dashed and dash-dotted lines*), where it is excited by a permanent chromosphere. Note that the spectra of Betelgeuse and  $\mu$  Cep are blueshifted to align the photospheric absorption lines with the outburst spectrum of  $\rho$  Cas. The synthetic spectrum of Betelgeuse (*dotted line*) is computed without a model of the chromosphere (see text).

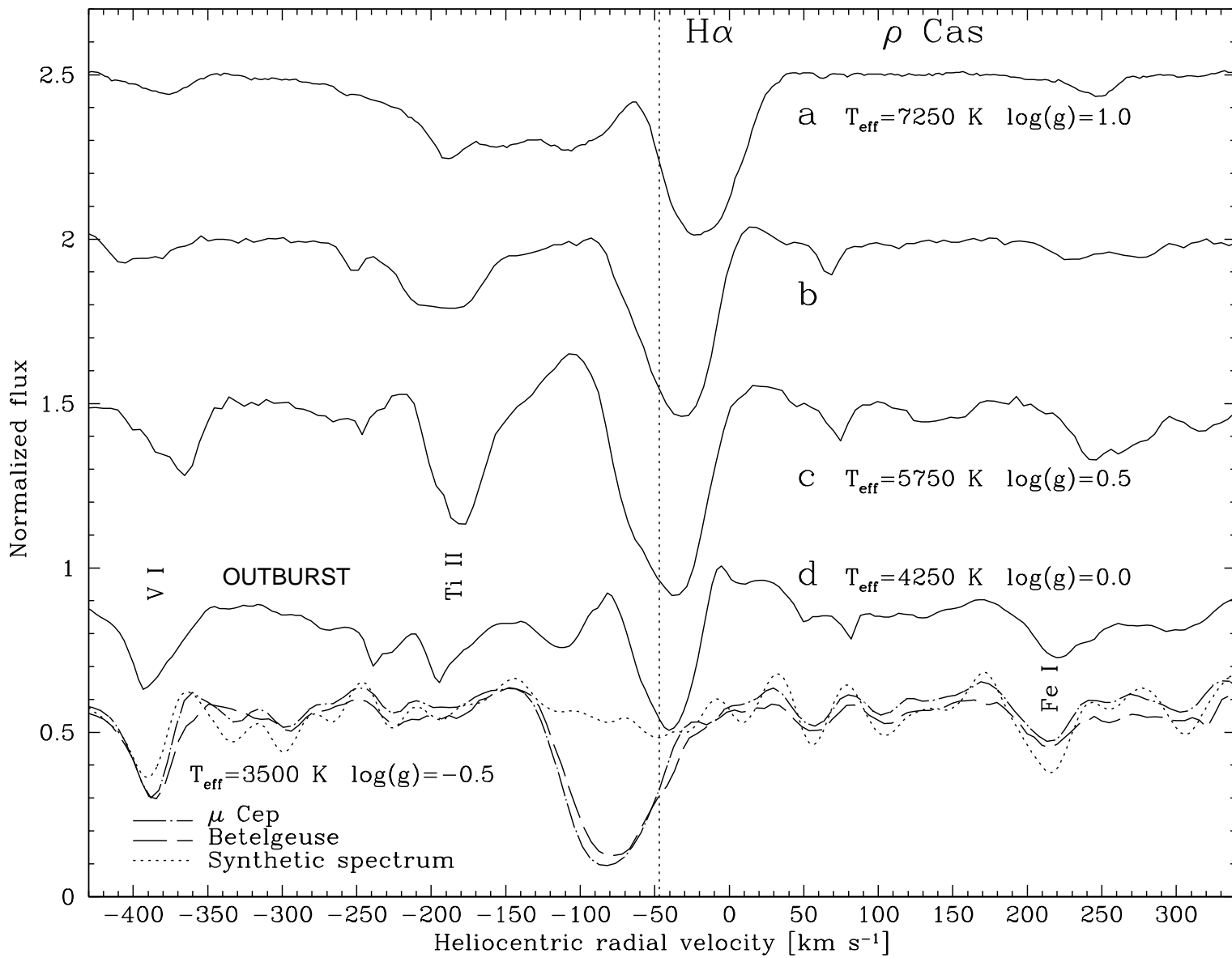


Fig. 8.— High-resolution spectra of  $\rho$  Cas in the upper panel do not reveal central Ca II H emission in 1996 December (*solid line*), 1998 October (*dash-dotted line*), and 2002 January (*dashed line*) after the outburst. Permanent Fe I emission lines of RMT 45 and 43 are observed in the broad Ca II H line wings. Central emission is neither observed around the stellar rest wavelength (*vertical dotted lines*) of Ca II K in the lower panel. Central emission observed in Betelgeuse (*short dashed line*) emerges from the extended and permanent chromosphere. The Ca II H & K lines indicate the absence of a classic chromosphere in  $\rho$  Cas.

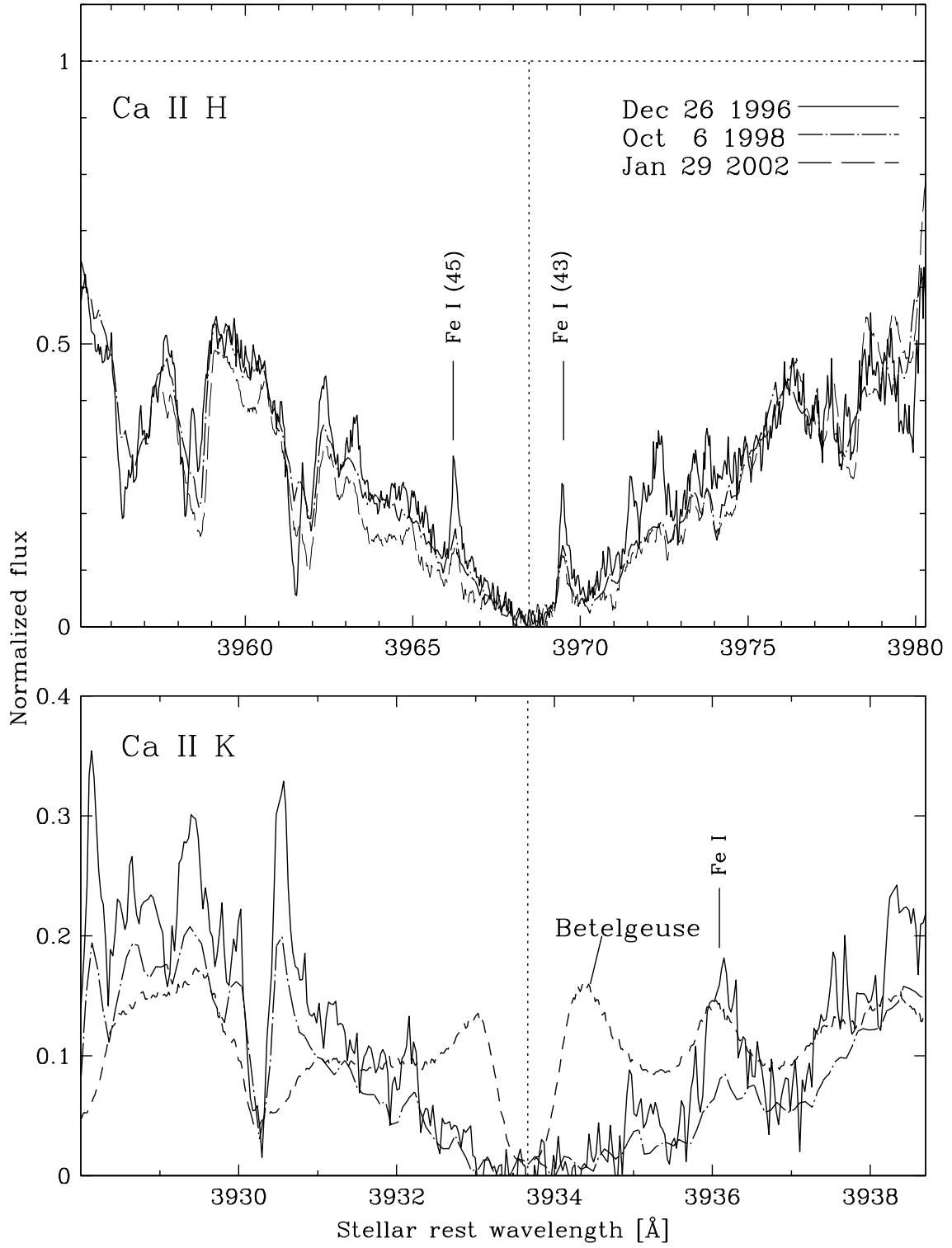


Fig. 9.— During the outburst central emission appears above the local continuum level (*horizontal dotted line*) in the Na *D* lines (*solid lines labeled d* of 2000 July 19 and August 2). The broad absorption portions of the lines are strongly intensity saturated, and do not show Doppler shifts with time (*dash-dotted and dashed lines labeled a and c*). The maximum of the central emission line is red-shifted with respect to the stellar rest velocity (*vertical dotted line*), and a blue-shifted narrow feature is observed in both lines of the doublet. The smaller figure shows a comparison of the doublet lines in  $\rho$  Cas (*bold solid lines*) with the lines observed in HR 8752 (*thin dashed lines*). Two interstellar absorption components are observed around  $-50 \text{ km s}^{-1}$  and  $-30 \text{ km s}^{-1}$  (see text). The outburst spectra clearly show that central emission contributes to the complex Na *D* line formation, besides the interstellar absorption (see text).



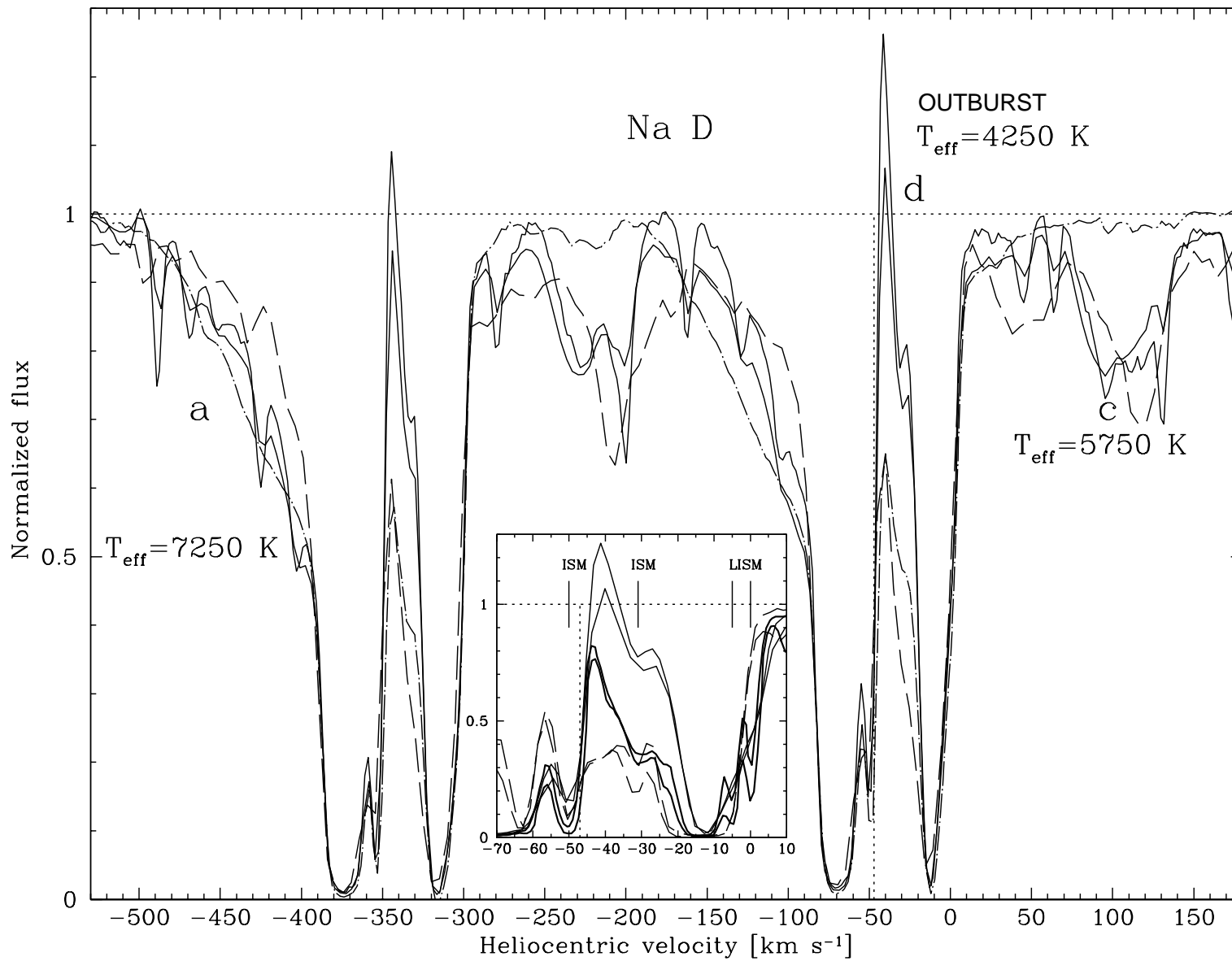


Fig. 10.— The outburst spectra of  $\rho$  Cas of 2000 Juny, August, and September show the development of optical titanium oxide (TiO) bands with three bandheads around 5446 Å. For display purposes, the spectra are shifted upwards by 15% of the normalized stellar continuum level. The TiO bands disappear in the spectra of 2001 February and October when  $T_{\text{eff}}$  increases above 4500 K (*upper thin solid lines*). The TiO band is permanent in the early M-type supergiants Betelgeuse and  $\mu$  Cep (*lower broken lines*). A spectrum synthesis with only TiO lines shows how these bands significantly decrease the continuum flux level longward of the bandheads (*bold solid line*). Note the typical split cores of Fe I lines in  $\rho$  Cas, caused by central emission, which is absent in Betelgeuse and  $\mu$  Cep. Note also how the component ratio of the split lines varies over time with the atmospheric dynamics.

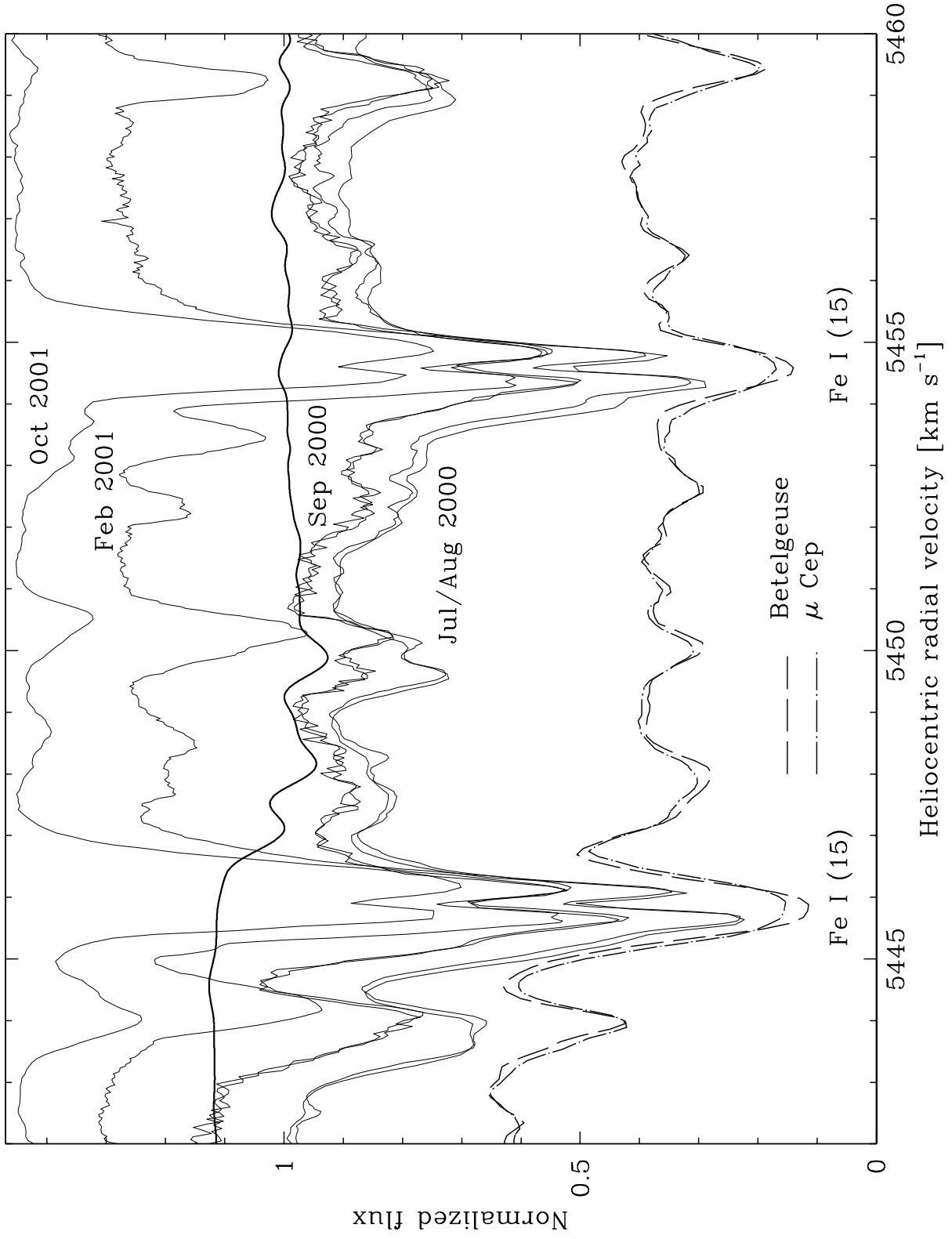


Fig. 11.— Near-IR TiO absorption bands are observed during the outburst of  $\rho$  Cas in 2000 July (*middle solid line*). The weak TiO bands around 7070 Å have distinct shapes (*at vertical solid lines*), also observed in Betelgeuse (*lower solid line*). The synthetic spectrum of  $\rho$  Cas is computed with only TiO lines (of the P, Q, & R branches) (*upper dotted line*), while that of Betelgeuse (*lower dotted line*) also includes molecular and atomic lines. Note that the TiO bands are considerably broader than the telluric lines (*marked with  $\oplus$* ).

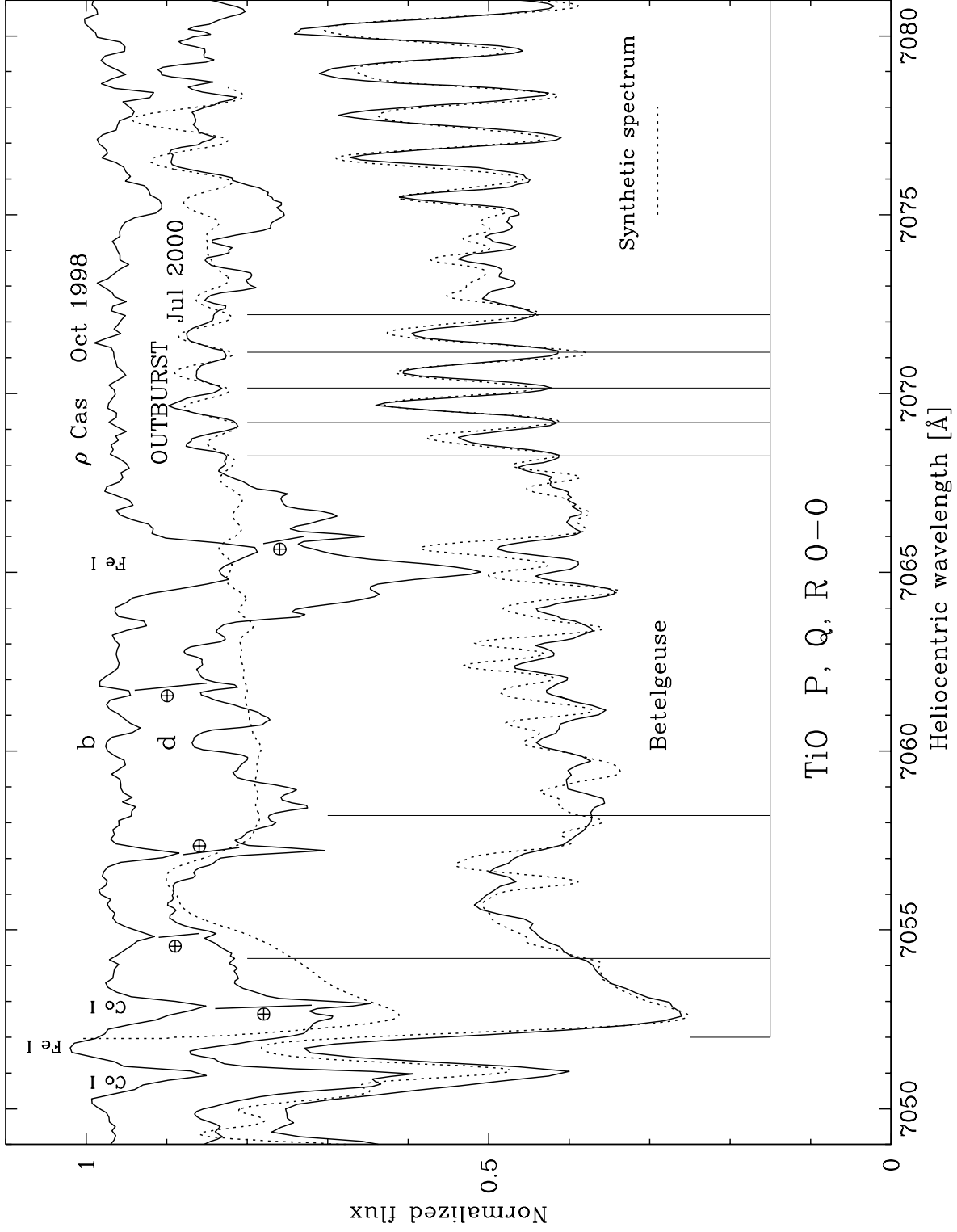


Fig. 12.— The TiO band at 7069.2 Å, observed during the outburst of  $\rho$  Cas on 2000 July 19 in the upper panel, is best fit (*dotted line*) for a model atmosphere with  $T_{\text{eff}}=3750$  K and  $\log g=0$  in the lower panel. The spectrum of 2002 January with higher  $T_{\text{eff}}$  does not show the TiO bands. A microturbulence velocity of  $11 \text{ km s}^{-1}$ , and macrobroadening of  $21 \text{ km s}^{-1}$  are required to broaden the synthetic spectrum (*dotted line*) of  $\rho$  Cas to the observed shape of the TiO band. The best fit yields a radial velocity of  $-82 \text{ km s}^{-1}$ , or an expansion velocity of  $35 \text{ km s}^{-1}$ . The strongest TiO lines for the synthesis, with  $\log gf$ -values  $>-1$ , are marked (*vertical lines*). The synthetic spectrum for Betelgeuse of Fig. 11 (*lower dotted line*), and the fit parameters are also shown. The model reveals that the main contribution to the TiO band formation occurs at  $-3 \leq \log \tau_{\text{Ross}} \leq 0$ , with a lower gas density limit of  $\rho_{\text{min}}=10^{-10} \text{ gr cm}^{-3}$  (see text).

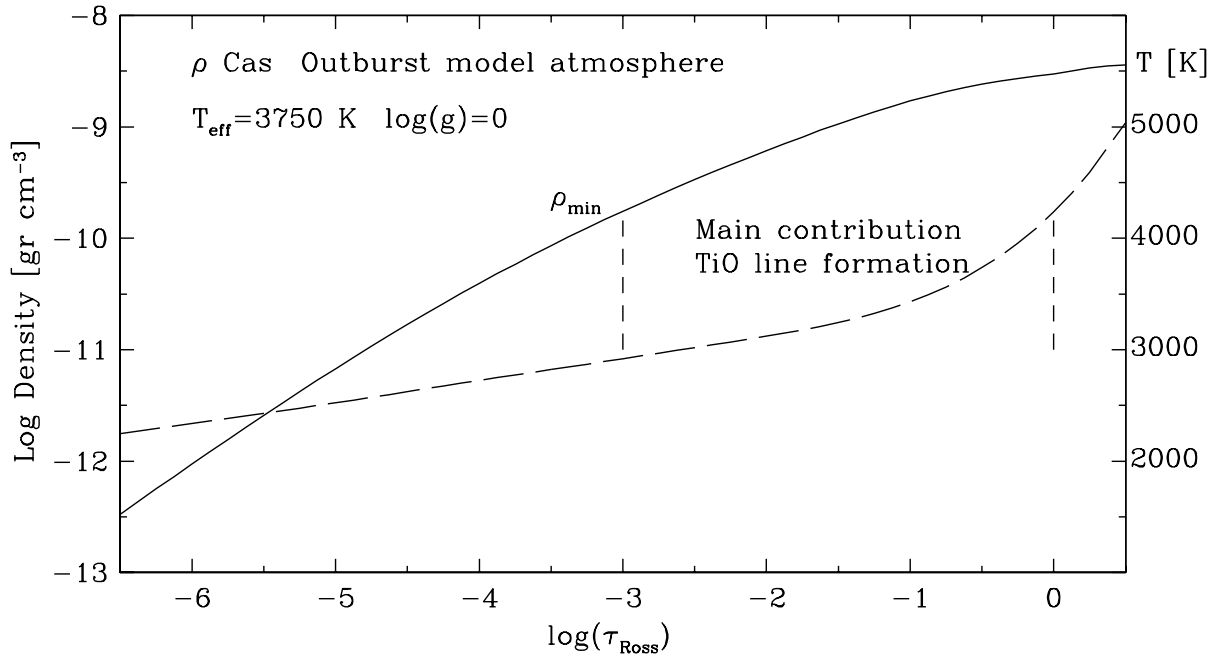
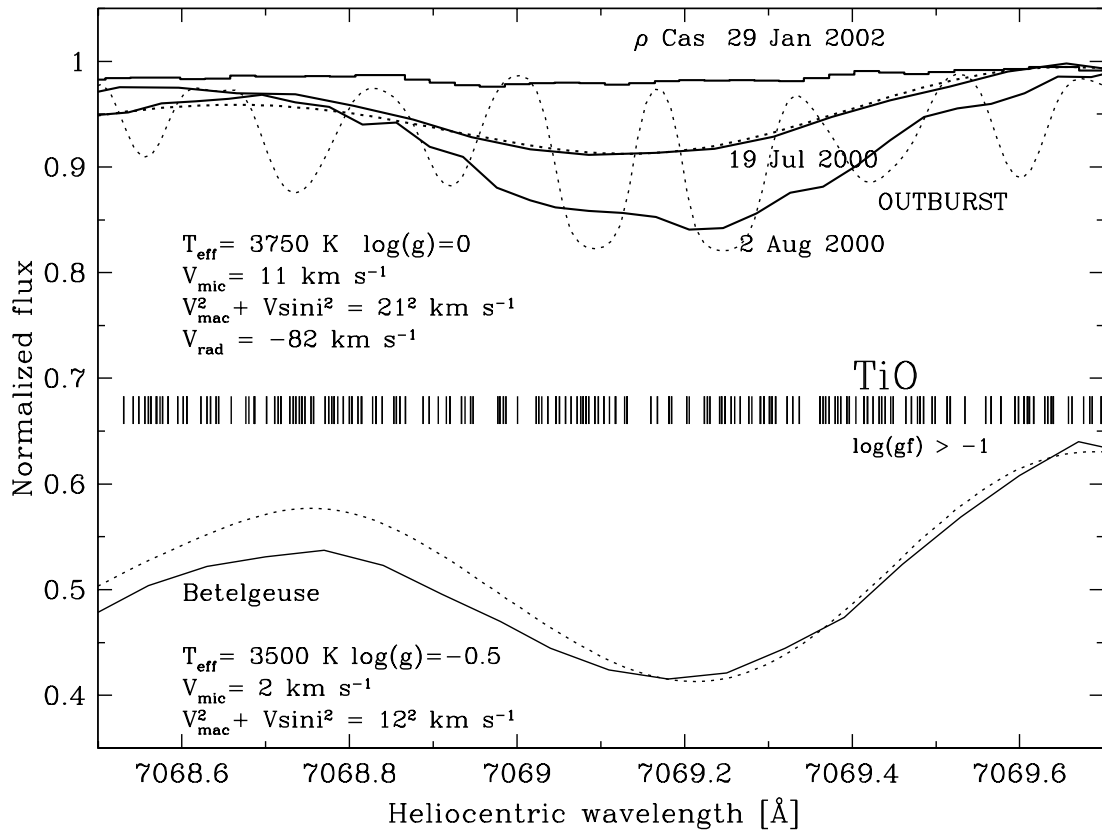


Fig. 13.— The panels compare the  $V$ -brightness changes during the three outbursts of  $\rho$  Cas in the last century. The strong  $V$ -brightness decrease by  $1^m.2$ – $1^m.4$  in 1946 and 2000 is preceded by a pre-outburst cycle and a bright maximum. The deep brightness minima during the three outbursts have considerably shortened from  $\sim 400$  d in 1946,  $\sim 200$  d in 1986, to  $\sim 100$  d in 2000. TiO bands are not observed in 1945 August (*vertical line labeled ‘no TiO’*), before the brightness maximum. Neither are they observed in the high-resolution pre-outburst spectra of 1999 (*vertical lines No. 39 to 63*). The TiO bands develop in the summer of 2000 (*Nos. 64 & 65*), before the deep minimum, and disappear during the brightness increase (*No. 69*). TiO bands are also observed before the deep minimum of 1946. It indicates that TiO forms only during phases of very fast atmospheric expansion, when the atmosphere sufficiently cools to  $T_{\text{eff}} \leq 4250$  K. The outburst of 1986 is rather moderate. Optical TiO bands are only observed during the deep minimum. Strong emission in the blue wing of  $H\alpha$  develops before the outbursts of 1986 and 2000, when the photosphere collapses (see text).



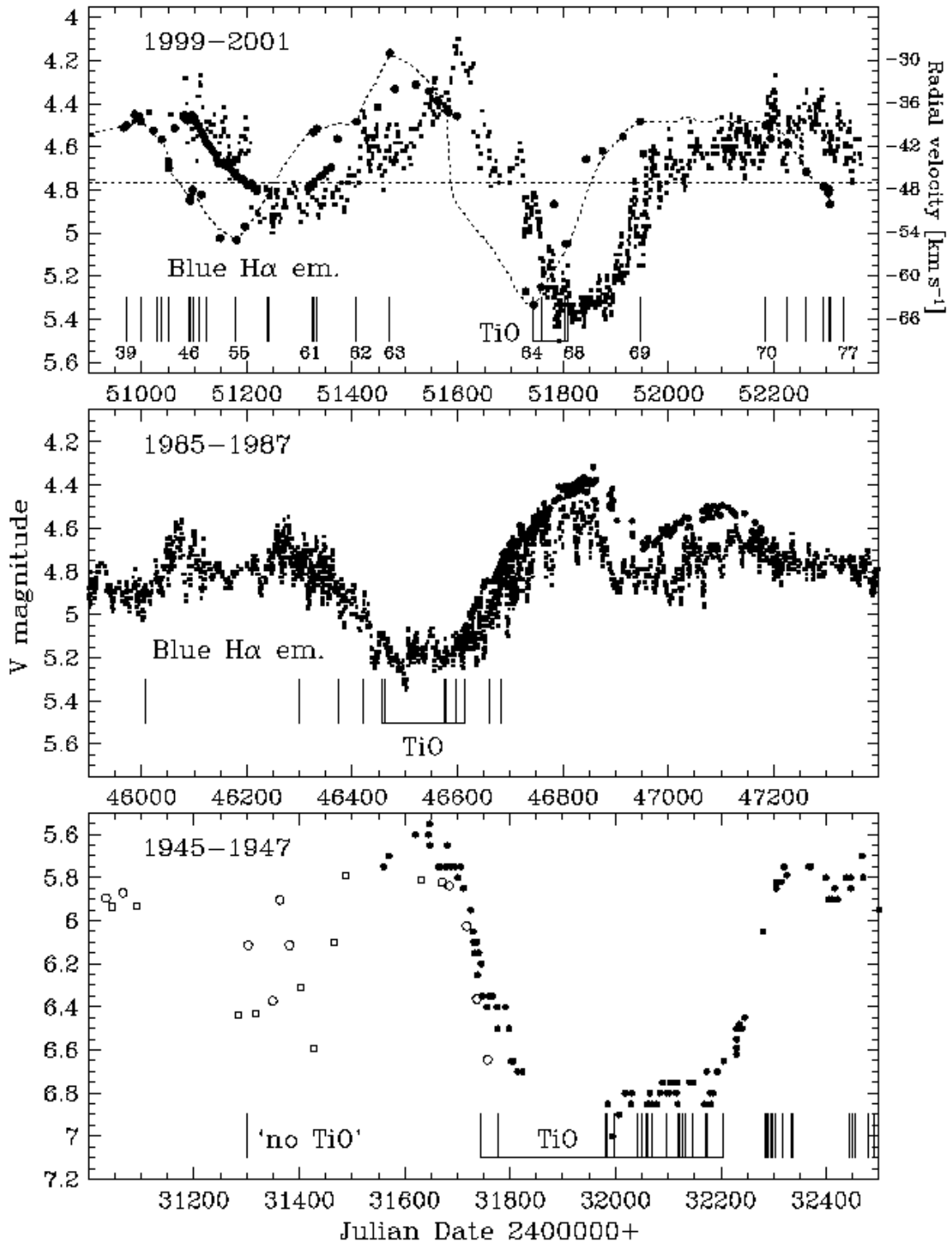


Fig. 14.— The expansion velocity of recombining hydrogen gas with an initial kinetic temperature of 8000 K, is computed as a function of the final gas temperature  $T$  (*bold lines*). With the recombination during cooling, the velocity of gas parcels that cool to 4000 K  $\leq T \leq 6000$  K, with an ionization fraction of  $x \sim 0.5$  (*thin lines*), strongly increases, because the recombination energy drives the expansion with the conservation of total energy and flow momentum. The gas parcels are initially at rest, and their acceleration is computed for flow momenta of 0.1 (*dashed lines*), 1 (*solid lines*), and 10 (*dash-dotted lines*) times the initial gas pressure. In the partial hydrogen ionization-recombination zone the gas parcels become very expandable or compressible, because  $1/(\Gamma_1 - 1)$  and  $1/(\Gamma_3 - 1)$  assume maximum values. The dotted line is computed without recombination (i.e. pure thermal expansion), which does not yield sufficiently large photospheric expansion velocities observed for the outburst of  $\rho$  Cas.

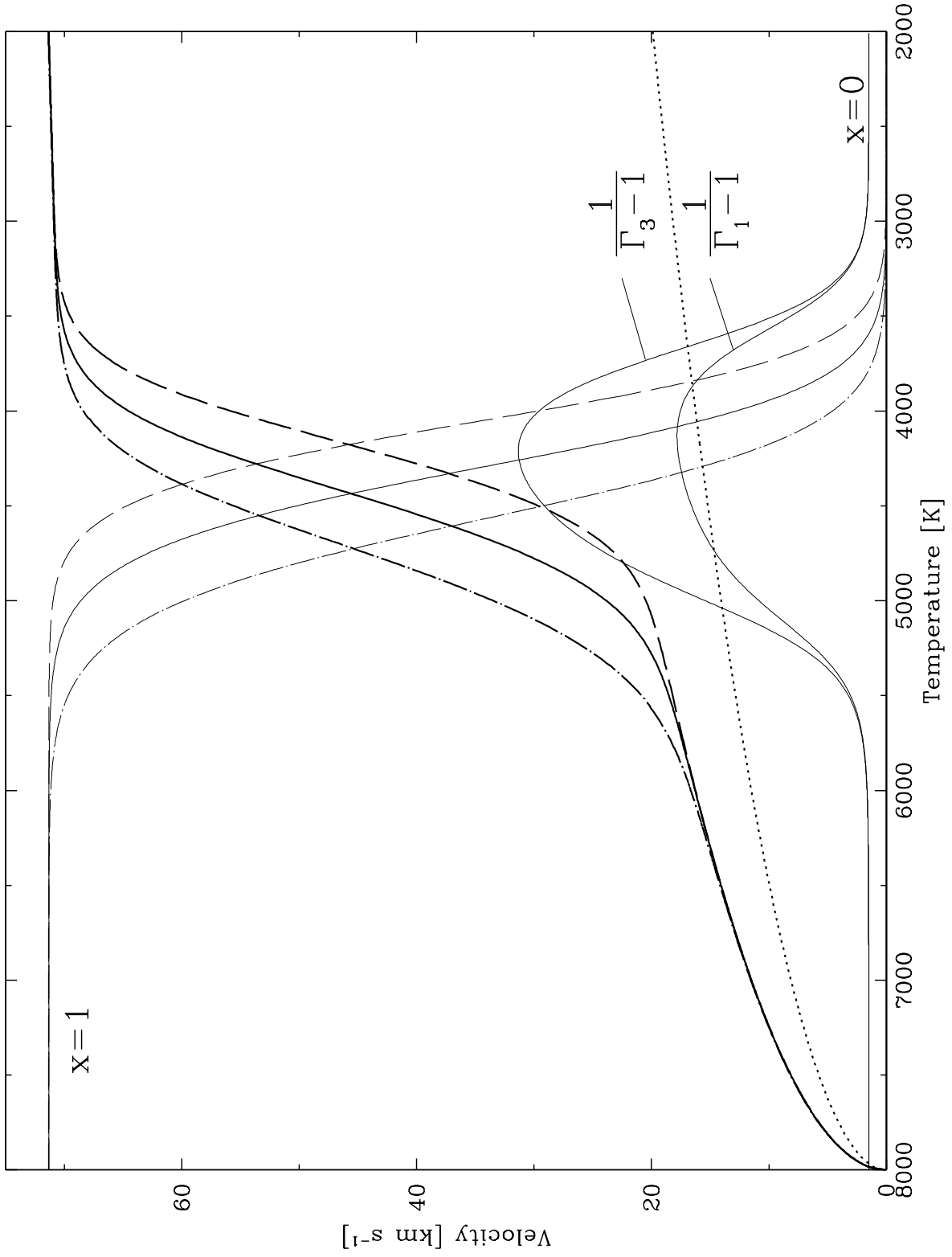


Fig. 15.— Top: Kinetic temperature structure  $T$  with optical depth (*thick solid line*), the ionization fraction  $x$  (*thin solid line*), and  $\Gamma_1$  (*thin dot short-dashed line*) of the model atmosphere before outburst ( $T_{\text{eff}}=7250$  K). The changes of  $T$  (*thick long-dashed short-dashed line*),  $x$  (*thin dot long-dashed line*), and  $\Gamma_1$  (*thin long-dashed dotted*) after the outburst (to  $T_{\text{eff}}=3750$  K) are also plotted.  $\Gamma_1$  increases from a value below  $4/3$  for dynamic atmospheric stability (*horizontal dotted line*), to well above  $4/3$  beyond the partial recombination zone of hydrogen ( $-0.5 \leq \log \tau_{\text{Ross}} \leq 0.5$ ). Bottom: The cooling of 3500 K increases the photospheric outflow velocity  $v$  (*bold solid line*) in the partial ionization zone to above  $35 \text{ km s}^{-1}$ , observed for the TiO bands. These atmospheric layers are very expandable, where  $1/(\Gamma_3-1)$  assumes maximum values (*thin dash-dotted line*), and yield a relative radius increase  $\Delta r/r \simeq 2.5$  (*thin dashed line*). The time-scale for spherical adiabatic expansion  $t_{\text{ad}}$  (*thin solid line*) in this region at  $r=R_* \simeq 400 R_{\odot}$  ranges between 170 and 267 d, comparable to the observed time of  $\sim 200$  d for the rapid  $V$ -brightness decrease during the outburst of  $\rho$  Cas (see text).

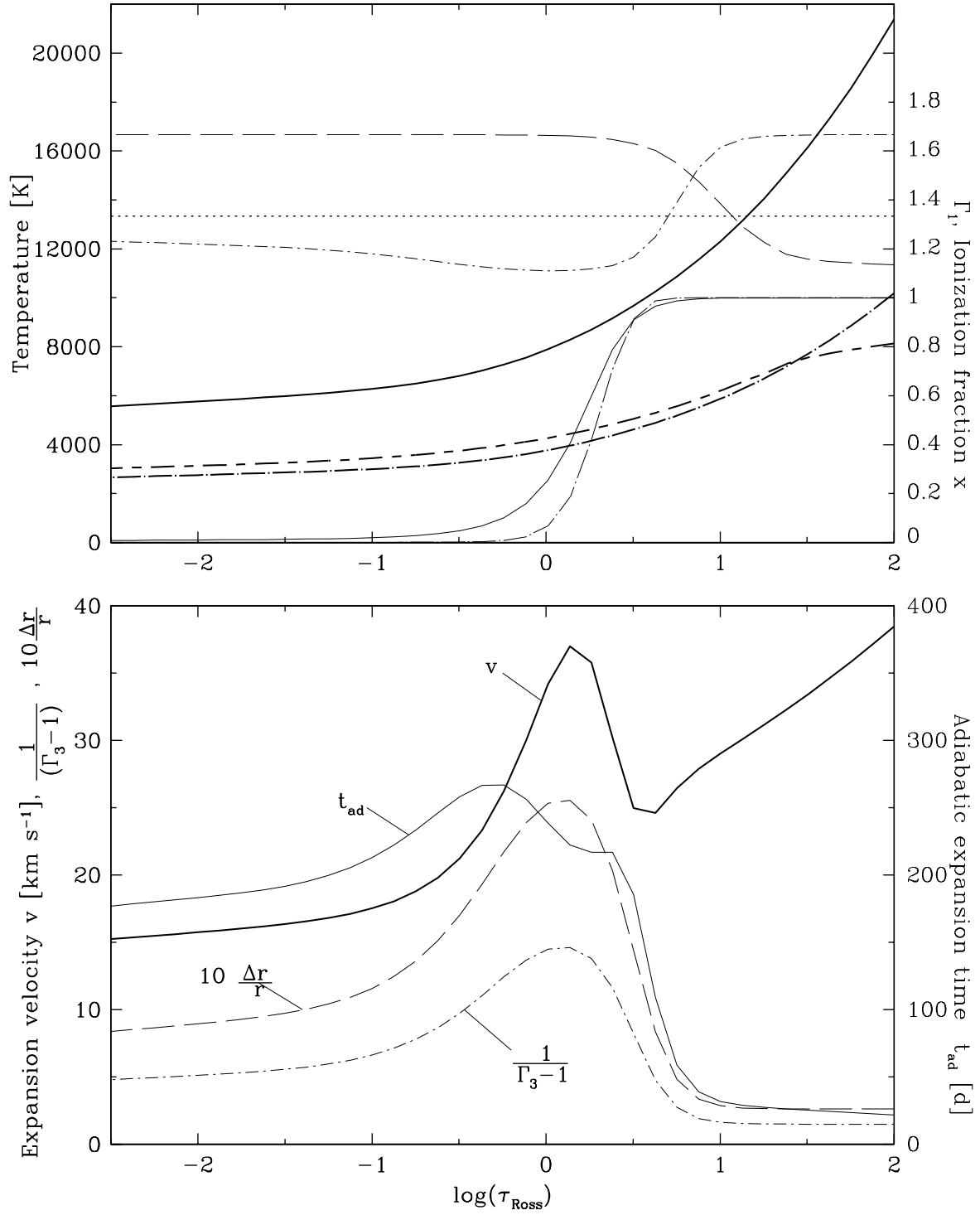


Table 1. Near-UV, optical, and near-IR high-resolution echelle spectra of  $\rho$  Cas in 1993-2002

No.	Telescope- Instr.	Obs Date	Jul. Date 2400000+	Time (UT)	Air- mass	Wav. range (Å)	Detector /Grating	$R$	Exp. times (s)
1	Ritter	1993 Nov 28	49319	04:28	1.2	5473–6799	CCD1	26,000	1200
2	SAO/AN	1993 Nov 29	49320			4400–6700		36,000	
3	Ritter	1993 Dec 01	49322	02:28	1.11	5473–6799	CCD1	26,000	1200
4	WHT-UES	1993 Dec 20	49342	20:28	1.18	4800–7740	E31	50,000	100,2×150
5	WHT-UES	1994 Jul 25	49558	02:05	1.33	4800–7740	E31	50,000	60,3×50
6	WHT-UES	1994 Aug 20	49584	03:57	1.15	4800–7740	E31	50,000	4×100
7	Ritter	1994 Sep 18	49613	05:47	1.04	5470–6796	CCD1	26,000	1800
8	Ritter	1994 Oct 11	49636	05:48	1.08	5469–6794	CCD1	26,000	1800
9	Ritter	1994 Nov 11	49667	03:35	1.07	5469–6794	CCD1	26,000	1200
10	Ritter	1994 Dec 23	49709	01:08	2.02	5473–6799	CCD1	26,000	900
11	WHT-UES	1995 Apr 18	49825	05:28	2.37	4490–6690	E31	50,000	200,400
12	SAO/AN	1995 Jun 09	49877	04:11	1.1	4924–6600		36,000	
13	SAO/AN	1995 Jun 15	49883	03:51	1.1	4924–6600		36,000	
14	SAO/AN	1995 Jul 31	49929			5496–6575		80,000	
15	SAO/AN	1995 Aug 04	49933	22:57	1.05	4925–6601		36,000	
16	SAO/AN	1995 Sep 06	49966			5499–6578		80,000	
17	Ritter	1995 Oct 13	50003	04:32	1.04	5472–6798	CCD1	26,000	900
18	SAO/AN	1995 Oct 13	50004	21:37	1.08	4923–6598		36,000	
19	SAO/AN	1995 Dec 03	50055	18:41	1.10	4928–6605		36,000	
20	SAO/A	1996 May 06	50209	02:05	1.32	4906–6634		36,000	
21	WHT-UES	1996 Jun 05	50239	05:06	1.35	4490–6690	E31	50,000	100,60
22	SAO/AN	1996 Jul 11	50275	00:51	1.04	4902–6629		36,000	
23	SAO/AN	1996 Jul 31	50296	23:43	1.04	4902–6629		36,000	
24	SAO/AN	1996 Aug 27	50322	00:22	1.08	4901–6627		36,000	
25	WHT-UES	1996 Sep 28	50354	00:20	1.14	4490–6690	E31	50,000	40,60,90
26	SAO/AN	1996 Nov 21	50409	18:29	1.06	4897–6622		36,000	
27	WHT-UES	1996 Dec 26	50444	23:10	1.71	3840–4990	E31	50,000	300
28	Ritter	1997 Jan 08	50456	23:47	1.9	5341–6597	CCD1	26,000	3600
29	SAO/AN	1997 Jan 18	50467	16:08	1.14	4554–6760		80,000	
30	SAO/AN	1997 Jan 22	50471	15:24	1.12	4912–6641		36,000	

Table 1—Continued

No.	Telescope- Instr.	Obs Date	Jul. Date 2400000+	Time (UT)	Air- mass	Wav. range (Å)	Detector /Grating	$R$	Exp. times (s)
31	Ritter	1997 Jan 29	50477	00:38	1.25	5341–6597	CCD1	26,000	3600
32	WHT-UES	1997 Feb 20	50500	19:26	1.68	cen 5513	E79 <sup>a</sup>	50,000	2×30,2×100
33	SAO/AN	1997 Feb 24	50504	16:10	1.49	5499–6570		170,000	
34	SAO/AN	1997 Mar 24	50532			5321–6150		170,000	
35	SAO/AN	1997 Jun 14	50613	00:26	1.18	4906–6634		40,000	
36	SAO/AN	1997 Aug 31	50692	02:30	1.3	4915–6624		40,000	
37	Ritter	1997 Sep 27	50718	04:03	1.06	5340–6596	CCD1	26,000	1200
38	Ritter	1997 Oct 22	50743	06:17	1.15	5339–6596	CCD1	26,000	1200
39	Ritter	1998 Jun 08	50972	08:26	1.3	5340–6596	CCD1	26,000	1800
40	Ritter	1998 Jul 05	50999	07:57	1.15	5340–6596	CCD1	26,000	1800
41	WHT-UES	1998 Aug 03	51029	23:00	2.01	3100–3700	E31	50,000	600
42	WHT-UES	1998 Aug 04	51030	04:43	1.14	3100–3700	E31	50,000	900
43	Ritter	1998 Aug 13	51038	07:30	1.05	5339–6596	CCD1	26,000	1800
44	Ritter	1998 Aug 26	51051	06:02	1.06	5339–6596	CCD1	26,000	2000
45	Ritter	1998 Aug 27	51052	08:51	1.09	5339–6596	CCD1	26,000	2000
46	NOT-Sofin	1998 Oct 04	51091	23:58	1.14	4507–6110	Cam1	160,000	2×600
47	NOT-Sofin	1998 Oct 05	51092	23:19	1.15	5060–7500	Cam2	80,000	200,3×180
48	NOT-Sofin	1998 Oct 06	51092	01:17	1.18	3420–11550	Cam3	33,000	190,110
49	NOT-Sofin	1998 Oct 08	51094	00:39	1.18	4791–7240	Cam1	160,000	3×600
50	WHT-UES	1998 Oct 08	51095	22:14	1.20	4050–8800	E31	50,000	2×100
51	NOT-Sofin	1998 Oct 11	51097	02:38	1.43	4322–5620	Cam2	80,000	5×900
52	NOT-Sofin	1998 Oct 11	51097	04:12	1.81	3470–11550	Cam3	33,000	2×300,2×240
53	WHT-UES	1998 Oct 22	51109	23:55	1.16	4050–8800	E31	50,000	2×100,50
54	NOT-Sofin	1998 Nov 05	51123	23:51	1.24	4507–6289	Cam1	160,000	480,300
55	WHT-UES	1999 Jan 01	51180	19:35	1.17	4050–8800	E31	50,000	2×100
56	NOT-Sofin	1999 Feb 28	51238	19:44	1.97	4407–5660	Cam2	80,000	3×900
57	NOT-Sofin	1999 Mar 02	51240	19:29	2.07	4407–5660	Cam2	80,000	6×900
58	NOT-Sofin	1999 May 27	51325	05:52	1.33	4407–5660	Cam2	80,000	400
59	NOT-Sofin	1999 May 28	51326	05:07	1.45	3468–11332	Cam3	33,000	450,230
60	NOT-Sofin	1999 May 30	51328	03:15	1.95	4407–5660	Cam2	80,000	725,600

Table 1—Continued

No.	Telescope- Instr.	Obs Date	Jul. Date 2400000+	Time (UT)	Air- mass	Wav. range (Å)	Detector /Grating	$R$	Exp. times (s)
61	NOT-Sofin	1999 Jun 04	51333	04:34	1.48	3495–11332	Cam3	33,000	2×80,180
62	WHT-UES	1999 Aug 18	51408	03:08	1.14	4050–8800	E31	50,000	2×100,2×30
63	NOT-Sofin	1999 Oct 19	51471	23:19	1.14	3495–11333	Cam3	33,000	430,2×80
64	WHT-UES	2000 Jul 19	51744	02:10	1.37	4050–8800	E31	50,000	150
65	WHT-UES	2000 Aug 02	51758	05:12	1.15	5410–8800	E31	50,000	60,30
66	Ritter	2000 Sep 17	51804	06:38	1.13	5339–6596	CCD1	26,000	3000
67	Ritter	2000 Sep 20	51808	05:28	1.17	5339–6596	CCD1	26,000	3000
68	Shajn	2000 Sep 21	51809	22:41	1.04	<sup>c</sup>	CCD	30,000	1800,1200,3000
69	WHT-UES	2001 Feb 05	51946	20:34	1.72	cen 7090	E79 <sup>a</sup>	50,000	300,2×240
70	WHT-UES	2001 Oct 02	52184	03:14	1.33	4050–8800	E31	50,000	100,2×90
71	Ritter	2001 Nov 12	52225	04:52	1.13	5339–6596	CCD1	26,000	3600
72	TBL	2001 Dec 18	52262	20:28	1.15	4489–6619	CCD	35,000	1600
73	Ritter	2002 Jan 19	52294	23:52	1.15	5339–6596	CCD1	26,000	3600
74	NOT-Sofin	2002 Jan 29	52303	19:53	1.4	3758–11225	Cam2	80,000	<sup>b</sup>
75	NOT-Sofin	2002 Jan 31	52305	19:44	1.4	3620–10947	Cam2	80,000	<sup>b</sup>
76	NOT-Sofin	2002 Feb 01	52306	19:36	1.4	3572–11321	Cam3	33,000	<sup>b</sup>
77	Shajn	2002 Feb 26	52332	16:12	1.46	<sup>c</sup>	CCD	30,000	900,900,900
78	Ritter	2002 Jul 07	52462	08:07	1.55	5339–6596	CCD1	26,000	3000

<sup>a</sup> E79 grating with 18 orders; exposures at indicated central wavelength contain no H $\alpha$

<sup>b</sup> S/N > 300 at echelle orders 6000–9000 Å

<sup>c</sup> Coudé spectra of 30 Å and 64 Å, centered at Ca II  $\lambda$ 8540, H $\alpha$ , and Na  $D$



Table 2. H $\alpha$  and Fe I radial velocities, and equivalent width values from echelle spectra of  $\rho$  Cas in Table 1

Spectrum No.	Obs Date	Jul. Date 2400000+	Fe I $\lambda$ 5572 (mÅ)	(km s <sup>-1</sup> )	H $\alpha$ (mÅ)	(km s <sup>-1</sup> )	Fe II $\lambda$ 5325 (mÅ)
1	1993 Nov 28	49319	341	-53.5	707	-35.5	-
2	1993 Nov 29	49320	321	-54.0	709	-34.5	571
3	1993 Dec 01	49322	360	-54.5	700	-34.5	
4	1993 Dec 20	49342	393	-59.0	770	-35.0	541
5	1994 Jul 25	49558	416	-50.5	743	-62.5	377
6	1994 Aug 20	49584					
7	1994 Sep 18	49613	396	-50.0	726	-65.0	-
8	1994 Oct 11	49636	425	-51.0	790	-66.0	-
9	1994 Nov 11	49667	483	-53.0	763	-65.5	-
10	1994 Dec 23	49709	513	-53.0	722	-63.0	-
11	1995 Apr 18	49825	551	-51.0	764	-56.5	366
12	1995 Jun 09	49877	535	-50.5	684	-60.0	371
13	1995 Jun 15	49883	525	-49.5	694	-59.0	
14	1995 Jul 31	49929	497	-48.0	773	-57.0	328
15	1995 Aug 04	49933	508	-48.0	702	-55.5	
16	1995 Sep 06	49966	511	-47.0	830	-57.5	364
17	1995 Oct 13	50003	467	-47.5	902	-52.5	-
18	1995 Oct 13	50004	462	-49.0	899	-54.0	434
19	1995 Dec 03	50055	465	-56.5	772	-50.5	438
20	1996 May 06	50209	382	-52.0	620	-49.5	465
21	1996 Jun 05	50239	449	-46.5	619	-46.5	445
22	1996 Jul 11	50275	573	-49.0	677	-46.5	
23	1996 Jul 31	50296	555	-51.0	695	-45.0	435
24	1996 Aug 27	50322	535	-48.5	662	-42.5	435
25	1996 Sep 28	50354	527	-48.0	566	-41.0	401
26	1996 Nov 21	50409	481	-49.5	286	-43.0	333
27	1996 Dec 26	50444	-	-	-	-	-
28	1997 Jan 08	50456	561	-45.0	288	-44.5	-
29	1997 Jan 18	50467	529	-44.5	208	-43.5	326
30	1997 Jan 22	50471	526	-43.5	210	-43.0	327

Table 2—Continued

Spectrum No.	Obs Date	Jul. Date 2400000+	Fe I $\lambda$ 5572		H $\alpha$		Fe II $\lambda$ 5325
			(mÅ)	(km s <sup>-1</sup> )	(mÅ)	(km s <sup>-1</sup> )	(mÅ)
31	1997 Jan 29	50477	538	-43.0	283	-43.0	-
32	1997 Feb 20	50500	-	-	-	-	-
33	1997 Feb 24	50504	578	-42.5	256	-42.5	-
34	1997 Mar 24	50532	523	-41.0	-	-	347
35	1997 Jun 14	50613	456	-34.5	392	-36.5	369
36	1997 Aug 31	50692	455	-41.5	540	-41.0	327
37	1997 Sep 27	50718	433	-43.5	569	-37.5	-
38	1997 Oct 22	50743	412	-45.0	580	-35.5	-
39	1998 Jun 08	50972	408	-40.5	642	-36.0	-
40	1998 Jul 05	50999	413	-40.0	670	-36.5	-
41	1998 Aug 03	51029	-	-	-	-	-
42	1998 Aug 04	51030	-	-	-	-	-
43	1998 Aug 13	51038	382	-42.5	636	-37.0	-
44	1998 Aug 26	51051	354	-45.5	605	-36.5	-
45	1998 Aug 27	51052	356	-46.5	604	-36.5	-
46	1998 Oct 04	51091	-	-	-	-	-
47	1998 Oct 05	51092	314	-51.0	534	-36.0	434
48	1998 Oct 06	51093	315	-50.5	563	-36.0	439
49	1998 Oct 08	51094	-	-	-	-	-
50	1998 Oct 08	51095	317	-50.5	555	-36.0	445
51	1998 Oct 11	51097	325	-49.5	485	-35.0	-
52	1998 Oct 11	51097	325	-49.5	485	-35.0	-
53	1998 Oct 22	51109	-	-	-	-	-
54	1998 Nov 05	51123	-	-	-	-	-
55	1999 Jan 01	51180	497	-56.5	655	-42.5	508
56	1999 Feb 28	51238	-	-	-	-	-
57	1999 Mar 02	51240	-	-	-	-	-
58	1999 May 27	51325	-	-	-	-	-
59	1999 May 28	51326	568	-41.5	505	-41.5	367
60	1999 May 30	51328	-	-	-	-	-

Table 2—Continued

Spectrum No.	Obs Date	Jul. Date 2400000+	Fe I $\lambda$ 5572 (mÅ)	(km s <sup>-1</sup> )	H $\alpha$ (mÅ)	(km s <sup>-1</sup> )	Fe II $\lambda$ 5325 (mÅ)
61	1999 Jun 04	51333	553	-41.0	532	-41.5	381
62	1999 Aug 18	51408	502	-40.0	418	-38.5	401
63	1999 Oct 19	51471	478	-30.5	505	-31.5	431
64	2000 Jul 19	51744	583	-65.5	368	-42.5	323
65	2000 Aug 02	51758	578	-63.0	419	-46.0	-
66	2000 Sep 17	51804	592	-57.0	279	-44.0	263
67	2000 Sep 20	51808	609	-57.0	256	-44.0	279
68	2000 Sep 21	51809	-	-	-82	-44.0	-
69	2001 Feb 05	51946	642	-40.0	-	-	-
70	2001 Oct 02	52184	369	-40.5	452	-35.0	449
71	2001 Nov 12	52225	362	-43.0	471	-34.5	513
72	2001 Dec 18	52262	282	-47.0	214	-34.5	493
73	2001 Jan 19	52294	365	-49.0	180	-34.5	419
74	2002 Jan 29	52303	334	-50.0	112	-35.5	-
75	2002 Jan 31	52305	344	-49.5	084	-35.0	412
76	2002 Feb 01	52306	331	-51.5	014	-35.5	406
77	2002 Feb 26	52332	-	-	178	-35.0	-
78	2002 Jul 07	52462	455	-48.0	462	-32.0	392

Table 3. Heliocentric radial velocity values of  $\rho$  Cas from Oak Ridge Observatory

Observation No.	Obs Date	Jul. Date 2400000+	Radial velocity (km s <sup>-1</sup> )	$\sigma$ -error (km s <sup>-1</sup> )
1	1990 Jul 10	48082.7792	-49.25	1.76
2	1991 Jan 26	48282.5157	-57.44	1.64
3	1991 Jan 26	48283.4890	-56.81	1.69
4	1991 Feb 22	48309.5056	-53.49	1.57
5	1991 Jul 02	48439.7185	-43.87	1.31
6	1991 Jul 25	48462.7144	-43.38	1.50
7	1991 Aug 15	48483.6314	-44.75	1.46
8	1991 Sep 02	48501.8755	-46.22	1.58
9	1991 Oct 13	48542.8552	-46.26	1.42
10	1991 Dec 19	48609.5897	-44.32	1.61
11	1991 Dec 28	48618.6044	-44.04	1.86
12	1992 Jan 16	48637.5462	-44.12	1.66
13	1992 May 21	48763.8432	-48.21	1.80
14	1992 May 26	48768.8483	-48.86	1.76
15	1992 Jun 18	48791.7918	-50.42	1.63
16	1992 Jul 12	48815.7609	-51.73	1.66
17	1992 Aug 13	48847.6561	-53.35	1.91
18	1992 Sep 09	48874.5931	-54.74	1.78
19	1992 Sep 15	48880.8412	-56.35	1.89
20	1992 Nov 10	48936.6925	-57.40	1.90
21	1992 Dec 09	48965.6710	-56.62	1.99
22	1993 Jan 08	48995.5736	-55.63	1.90
23	1993 Oct 06	49266.8169	-45.37	1.48
24	1993 Oct 29	49289.7625	-44.76	1.59
25	1993 Nov 23	49314.6535	-48.48	2.00
26	1993 Dec 02	49323.6625	-50.23	2.08
27	1993 Dec 27	49348.6110	-58.16	2.29
28	1994 Jan 06	49358.6010	-60.94	2.14
29	1994 Jan 23	49375.5034	-64.57	2.08
30	1994 Jan 29	49382.4878	-65.05	1.97

Table 3—Continued

Observation No.	Obs Date	Jul. Date 2400000+	Radial velocity (km s <sup>-1</sup> )	$\sigma$ -error (km s <sup>-1</sup> )
31	1994 Feb 23	49400.4998	-67.10	1.97
32	1994 Aug 25	49589.5946	-59.09	1.61
33	1994 Sep 11	49606.8947	-58.50	1.59
34	1994 Sep 20	49615.5279	-58.52	1.57
35	1994 Oct 11	49636.7901	-59.44	1.53
36	1994 Oct 26	49651.7738	-60.46	1.57
37	1995 Jul 06	49904.7214	-49.09	1.70
38	1995 Jul 12	49910.7263	-50.05	1.75
39	1995 Jul 20	49918.7322	-50.58	1.81
40	1995 Sep 13	49973.5750	-52.59	1.89
41	1995 Oct 18	50008.7730	-54.22	1.80
42	1995 Dec 08	50059.6458	-55.76	1.76
43	1995 Dec 27	50078.5827	-54.88	1.66
44	1996 Jan 16	50098.5535	-53.49	1.65
45	1996 Jan 31	50113.5055	-51.85	1.67
46	1996 Feb 07	50121.4657	-51.60	1.64
47	1996 Aug 08	50303.6662	-50.19	1.74
48	1996 Aug 30	50325.6188	-50.79	1.71
49	1996 Oct 27	50383.7322	-51.21	1.67
50	1996 Nov 18	50405.6617	-49.79	1.72
51	1996 Dec 21	50438.6331	-49.88	1.65
52	1997 Jan 13	50461.5697	-47.96	1.92
53	1997 Jul 01	50630.7519	-39.87	1.58
54	1997 Jul 27	50656.7196	-41.22	1.52
55	1997 Sep 21	50712.8952	-42.83	1.49
56	1997 Oct 18	50739.7600	-42.76	1.53
57	1997 Nov 05	50757.7209	-43.67	1.43
58	1997 Nov 21	50773.6715	-44.83	1.63
59	1997 Dec 12	50794.6395	-45.93	1.54
60	1997 Dec 27	50809.5757	-45.69	1.52

Table 3—Continued

Observation No.	Obs Date	Jul. Date 2400000+	Radial velocity ( $\text{km s}^{-1}$ )	$\sigma$ -error ( $\text{km s}^{-1}$ )
61	1998 Jan 26	50840.4817	−45.56	1.45
62	1998 Jun 02	50966.8395	−43.42	1.53
63	1998 Jul 28	51022.6960	−43.58	1.54
64	1998 Sep 06	51062.6185	−46.40	1.61
65	1998 Oct 27	51113.7562	−51.44	1.71
66	1998 Dec 01	51148.6347	−54.76	1.73
67	1999 Jan 17	51196.4950	−54.74	1.85
68	1999 Jul 12	51371.7138	−42.95	1.69
69	1999 Sep 26	51447.8544	−38.65	1.56
70	1999 Oct 29	51480.7145	−37.05	1.49
71	1999 Dec 08	51520.6480	−36.80	1.47
72	2000 Jan 02	51545.6049	−36.62	1.34
73	2000 Jan 18	51561.5488	−37.37	1.36
74	2000 Feb 07	51582.4827	−39.44	1.74
75	2000 Feb 23	51598.4778	−40.74	2.02
76	2000 Jul 03	51728.7458	−64.23	3.01
77	2000 Aug 26	51782.6216	−55.54	2.99
78	2000 Oct 26	51843.7270	−51.68	2.21
79	2000 Nov 26	51874.6841	−48.57	2.22
80	2001 Jan 04	51913.5566	−43.90	2.17
81	2001 Feb 10	51951.4604	−43.70	1.86
82	2001 Aug 27	52148.6168	−40.94	1.65
83	2001 Sep 17	52169.5344	−40.96	1.54
84	2001 Oct 11	52193.7849	−40.65	1.49
85	2001 Nov 20	52233.6801	−41.80	1.60
86	2001 Dec 22	52265.6062	−42.93	1.63
87	2002 Jan 14	52288.5766	−42.77	1.59
88	2002 Feb 07	52313.4838	−43.99	1.71